Deformation-induced interface roughening and failure in polymer-coated steels

Citation for published version (APA):

Beeck, van, J. (2015). *Deformation-induced interface roughening and failure in polymer-coated steels*. [Phd Thesis 1 (Research TU/e / Graduation TU/e), Mechanical Engineering]. Technische Universiteit Eindhoven.

Document status and date:
Published: 01/01/2015

Document Version:
Publisher's PDF, also known as Version of Record (includes final page, issue and volume numbers)

Please check the document version of this publication:

• A submitted manuscript is the version of the article upon submission and before peer-review. There can be important differences between the submitted version and the official published version of record. People interested in the research are advised to contact the author for the final version of the publication, or visit the DOI to the publisher's website.
• The final author version and the galley proof are versions of the publication after peer review.
• The final published version features the final layout of the paper including the volume, issue and page numbers.

[Link to publication](#)

Deformation-induced interface roughening and failure in polymer-coated steels

Jeroen van Beeck
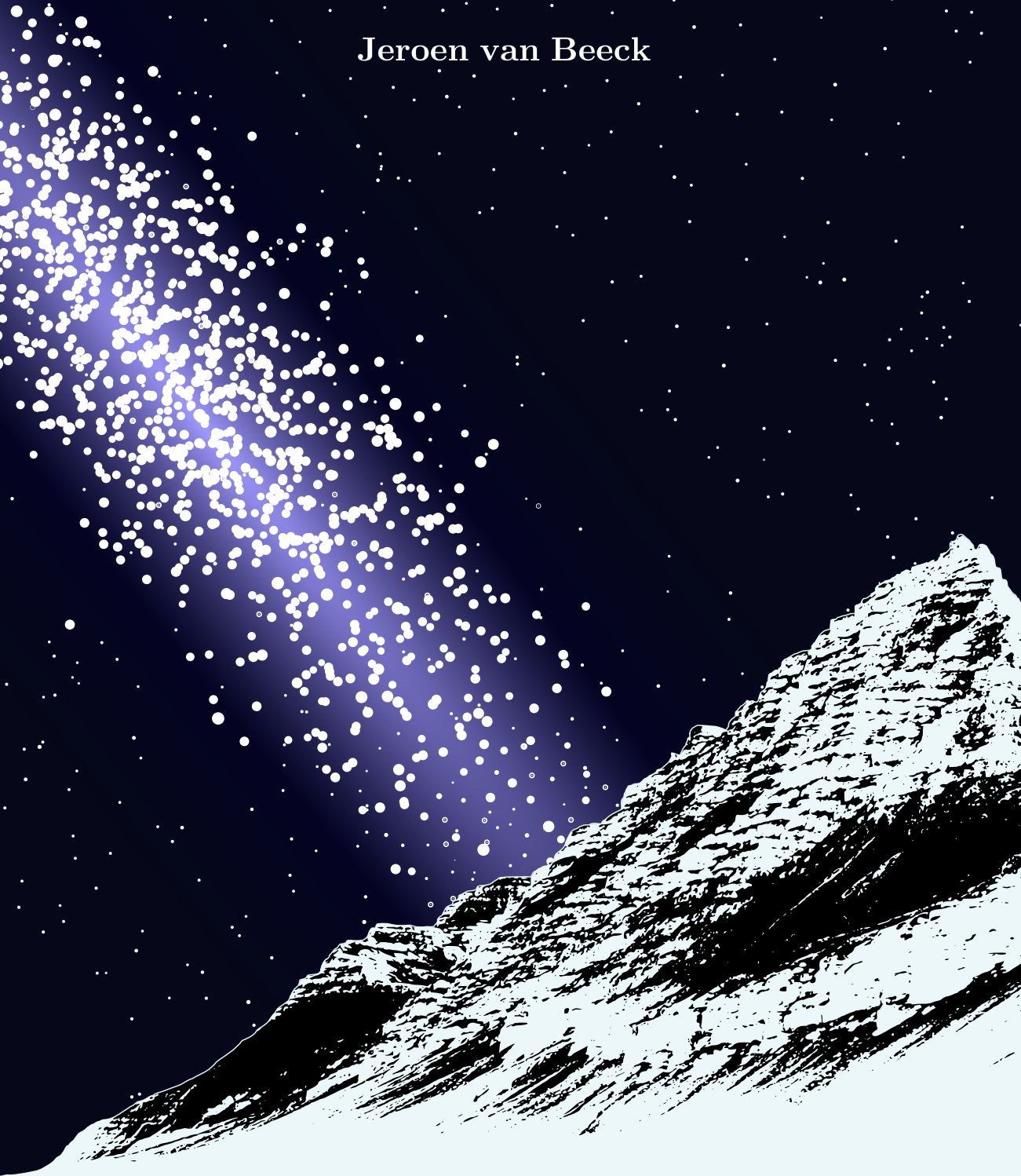
Deformation-induced interface roughening and failure in polymer-coated steels

Cover rationale:
The Icelandic mountain symbolizes the changing steel surface roughness, the PhD progress as experienced by the author, and the author's favorite pastime activity. The view on the galaxy illustrates our continuing quest to find our place within the universe.

Deformation-induced interface roughening and failure in polymer-coated steels

PROEFSCHRIFT

ter verkrijging van de graad van doctor aan de Technische
Universiteit Eindhoven, op gezag van de rector magnificus
prof.dr.ir. C.J. van Duijn, voor een commissie aangewezen door
het College voor Promoties, in het openbaar te verdedigen op
dinsdag 7 april 2015 om 16:00 uur

door

Jeroen van Beeck

geboren te Oss

Dit proefschrift is goedgekeurd door de promotoren en de samenstelling van de promotiecommissie is als volgt:

voorzitter:	prof.dr. L.P.H. de Goey
1$^{\text{e}}$ promotor:	prof.dr.ir. M.G.D. Geers
copromotor(en):	dr.ir. P.J.G. Schreurs
leden:	prof.dr.ir. A.H. van den Boogaard (UT)
	prof.dr.ir. J.P. Ponthot (Université de Liège)
	dr.ir. L.E. Govaert
	prof.dr. J.T.M. de Hosson (RUG)
adviseur(s):	dr.ir. B. Boelen (Tata Steel BV)

"Admitting that you do not know something is
the first step to learning."

Terry Goodkind, Faith of the Fallen

<div align="right">**SUMMARY**</div>

Deformation-induced interface roughening and failure in polymer-coated steels

An important topic for industrial innovation in the packaging industry today is environmental conservation by improving existing manufacturing processes. A prime example of this is the food and beverage industry where protective polymer coatings are applied to steels as a packaging material. A recent innovation in these applications is pre-coating the steel prior to can manufacturing. Compared to lacquering the steel after production, a reduction of energy consumption and CO_2 emission of one third is achieved. Furthermore, the process water used and the resulting solid wastes are reduced to practically zero.

However, this innovation comes with a number of challenges as the pre-coated steel is subjected to large deformations at increased temperatures and high strain rates during production. These deformations result in surface roughening of the steel and hence the polymer-steel interface. After production, the interface must not exhibit any damage (visible or invisible), even after a relatively long shelf-life period, as this damage triggers corrosion and compromises the quality of the canned content.

The topic explored in this thesis is the contribution of deformation-induced steel surface roughening during forming on the polymer-steel interface integrity. A numerical-experimental framework has been developed to study the interface during deformation-induced roughening of a coated packaging steel. The experimental investigation provides qualitative and quantitative insight into the roughening phenomenon and the results are incorporated into numerical simulations to predict the interface integrity.

First, the deformation-induced roughening phenomenon was studied experimentally. An uncoated packaging steel sheet was deformed in tension and sequential height profiles were measured using a confocal optical profiler. These profiles were used in a newly developed finite element based global digital image correlation method to extract the full-field three-dimensional displacement fields which accompany the change in surface roughness. The resulting displacement fields show the formation of hills and valleys on the steel surface, which grow as the deformation is increased.

The extracted displacement fields were applied as a boundary condition in a two-dimensional plane-strain simulation of a polymer layer. The interface between the steel and the polymer was modeled using a cohesive zone model. The change in steel roughness results in localized bands of increased stress and strain in the polymer coating. The interface shows delamination at high strains near these localization bands. By varying the thermodynamic state of the polymer coating, an optimum was identified for the age of the polymer. A young polymer shows significantly less localization with less interface damage as a result.

However, the polymer-coated steel is typically stored for long periods of time after lacquering the steel substrate material and prior to production during which the polymer ages continuously. Interface damage during production can be prevented by pre-conditioning

the polymer thermodynamic state before production, e.g. by rolling the polymer-coated steel. To study the effect of pre-conditioning, the evolution of the polymer state during rolling was investigated numerically. The predictions show a significant dependency of the state parameter on the rolling reduction indicating that the rolling reduction can be optimized to delay or even prevent interface damage during production.

To study more complex loading conditions typically encountered during production where the steel substrate is not experimentally accessible, i.e. deep drawing and wall ironing, a crystal plasticity model for the simulation of deformation-induced steel surface roughening was incorporated. Simulations of uniaxial tension showed that the predicted roughness compares qualitatively to experimental results. Furthermore, the simulations predicted the initiation and growth of interface damage. Comparing the simulation results in tension and compression showed that in compression, the roughening rate is increased with an increase in predicted interface damage as a result.

With the developed framework qualitative and (semi)-quantitative insight is gained in understanding how packaging steels roughen during production. Furthermore, the effects of the change in roughness on the integrity of the polymer-steel interface was characterized. With the identified optimum in the thermodynamic state and the possibility to pre-condition this state prior to forming, the formation of interface damage may be delayed or even prevented. Finally, the incorporation of a predictive steel model, i.c. crystal plasticity, complements the cumbersome measurements of the detailed experimental displacement fields that accompany deformation-induced roughening. This enables the analysis of industrial deformation processes where measuring the steel surface profile is difficult if not impossible, e.g. deep drawing and wall ironing.

The following notations are adopted throughout this thesis

Cartesian unit vectors	$\vec{e}_i; \; i = x, y, z$
vector	$\vec{a} = a_i \vec{e}_i$
second-order tensor	$\mathbf{A} = A_{ij} \vec{e}_i \vec{e}_j$
fourth-order tensor	$^4\mathbf{A} = A_{ijkl} \vec{e}_i \vec{e}_j \vec{e}_k \vec{e}_l$
matrix	$\underline{A}$
column	$\underset{\sim}{a}$
vectorial inner product	$\vec{a} \cdot \vec{b} = a_i b_i, \; i = x, y, z$
vectorial dyadic product	$\vec{a} \otimes \vec{b} = a_i b_j \vec{e}_i \vec{e}_j$
vectorial outer product	$\vec{a} \times \vec{b} = \vec{c}$
tensorial inner product	$\mathbf{A} \cdot \mathbf{B} = A_{ij} B_{jk} \vec{e}_i \vec{e}_k$
tensorial double inner product	$\mathbf{A} : \mathbf{B} = A_{ij} B_{ji}$
vector length	$||\vec{a}||$
matrix and tensor transpose	$\underline{A}^{\mathrm{T}}, \mathbf{A}^{\mathrm{T}}$
matrix and tensor inverse	$\underline{A}^{-1}, \mathbf{A}^{-1}$
material time derivative	$\dot{a}, \dot{\mathbf{A}}$
absolute value	$|a|$
normalized value	$\hat{a}$
matrix, column and spatial average	$\langle \underline{A} \rangle, \langle \underset{\sim}{a} \rangle, \langle a \rangle$

INTRODUCTION

1.1 Background and motivation

1.1.1 Polymer-coated steels

Sheet metal with a protective coating is increasingly used in manufacturing, e.g. the production of packaging for food, beverages, aerosols and paint (see also Fig. 1.1(a)). The coating ensures protection for the metal against the environment on either the inside or outside and thereby also protects the content. Traditionally, these products are manufactured using blank sheet metal, after which the coating is applied in several lacquering steps. This process is environmentally unfriendly as it involves the use of solvents and it is energy consuming. In recent years, the alternative of pre-coating the sheet metal prior to manufacturing has been explored since this significantly reduces the environmental impact of the production process.

An example of an application where the use of pre-coated metals has resulted in a drastic reduction of the environmental impact is pre-coated steel used in the food and beverage packaging industry, e.g. Protact [64] (see Fig. 1.1(b)). Here, an Electrolytically Chromium Coated Steel (ECCS) plate is pre-coated by extruding a thin Polyethylene terephthalate (PET) layer onto the preheated steel. Compared to the traditional production process, pre-coating the steel reduces the energy consumption and CO_2 emission with one third and the process water and resulting solid wastes to practically zero [1].
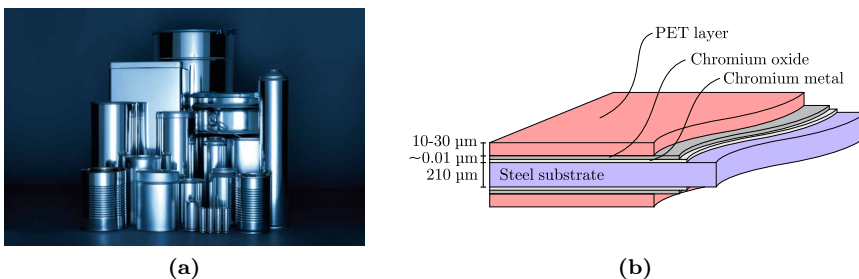

Figure 1.1: (a) Applications of metal-polymer laminates (after [64]) and (b) different material layers in a polymer-coated ECC steel (after [15]).

1.1.2 Challenges

During production, the polymer-coated steel is subjected to severe loading conditions. The production of a can or canister from these materials is accomplished through repeated deep (re-)drawing followed by wall ironing, see Fig. 1.2. The deformations are large and involve high strain rates, temperatures and pressures. Clearly, the production process may influence the polymer-steel interface integrity. While damage is often not visible by the human eye after manufacturing, it may become apparent during the prolonged product shelf-life. The packaging industry demands a material that does not exhibit any visible or invisible damage, even after a relatively long shelf-life period as this triggers corrosion and compromises the canned content [9, 14].

(a) deep drawing.   **(b)** deep redrawing.   **(c)** wall ironing.
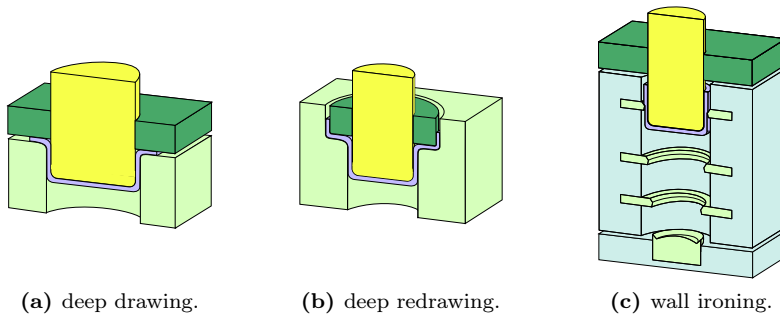
Figure 1.2: Different industrial manufacturing processes used in can production (after `CustomPartNet.com`).

Boelen et al. [9] showed experimentally with an acid vapor deposition and saline sterilization test that the polymer-steel interface weakens during production, see also Fig. 1.3. Furthermore, the influence of the sheet deformation on the polymer-steel interface was investigated experimentally via peel-off experiments by Boelen et al. [9] and Van den Bosch et al. [14]. They reported that the bonding between polymer and steel is reduced by (pre-)deforming the steel substrate. Similarly, experiments of Fedorov et al. [28] using laser-induced delamination shows the same trend. Even more recently, Faber et al. [25] revealed the presence of interface damage in produced cans by investigating the polymer-steel interface in cross-sections using Focused Ion Beam milling. These results suggest that deformation-induced roughening of the interface is the prime cause of the reduction in adhesion and possible delamination.
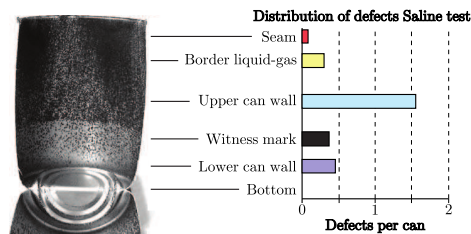
Figure 1.3: Experimental results of Boelen et al. (after [9]); the so-called witness marks indicate the transition between the subsequent steps in can production.

1.2   Deformation-induced roughening

A polycrystalline metal, i.e. the ECCS used in packaging for food and beverages, roughens at a free surface when it is deformed due to crystallographic differences between grains and other plasticity related phenomena. An example of the deformation-induced surface roughening for an ECC steel in tension is shown in Fig. 1.4. The initial surface profile is induced by the rolls rolling the steel to its desired thickness, see Fig. 1.4(a). The roughness profile measured after a tensile strain of $\varepsilon = 21\%$ (just before material failure), see Fig. 1.4(b), shows a drastic change in surface height profile. Local hills and valleys have formed on the initial surface profile. This roughening occurs over a wide range of scales, ranging from nano-scale to the size of multiple grains, depending on deformation conditions and material properties [54]. During production, the polymer-steel interface thus roughens and this influences the polymer-steel adhesion and may trigger interface failure.


(a) undeformed.   **(b)** $\varepsilon = 21\%$.
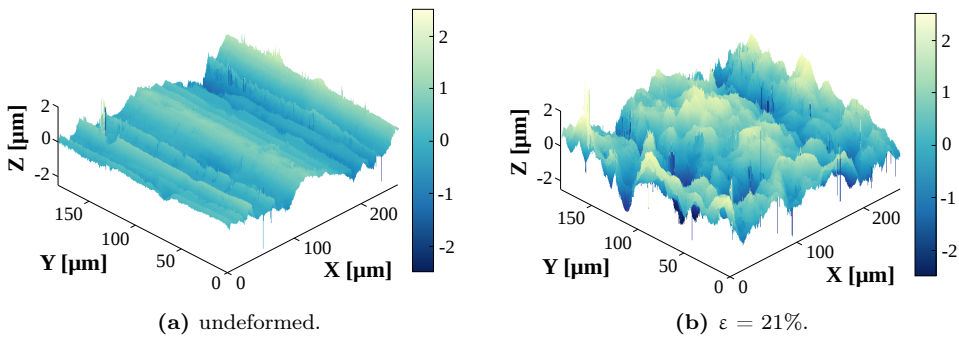
Figure 1.4: Example of deformation-induced roughening in a packaging steel deformed in tension.

1.3   Aim and scope

This thesis aims to analyze the effect of deformation-induced roughening during production on the polymer-steel interface via a numerical-experimental approach.

First, the deformation that accompanies the change in surface roughness of a packaging steel is studied experimentally. Tensile experiments are performed and the evolving steel surface profile is measured in-situ. The measured height profiles are used in a novel Finite Element based Global Digital Image Correlation technique to extract the full-field displacement field that accompanies the roughening phenomena.

The effect of this surface deformation on the polymer response and the interface integrity is then studied by exploiting the extracted displacement fields as a boundary condition in a numerical model of a thin polymer coating and a polymer-steel interface model. The simulations permit to analyze the local initiation and growth of interface damage as the steel surface roughens.

Based on the results of the numerical-experimental framework, pre-conditioning via rolling is studied to reduce the interface damage during production. The simulations show that the polymer can be pre-conditioned to delay or prevent the initiation of damage.

Finally, a numerical framework is developed that enables the study of deformation-induced interface roughening for more complex loading paths by incorporating a predictive steel constitutive model.

1.4 Outline

In chapter 2, a novel methodology for quantifying deformation-induced steel surface roughening is developed. A Finite Element based Global Digital Image Correlation technique is employed to extract the full-field three-dimensional displacement field that accompanies the change in surface roughness of a packaging steel deformed in tension. In chapter 3, the extracted displacement fields are exploited by applying them as a boundary condition in a numerical model of a polymer coating and the polymer-steel interface. A parameter study is performed with the numerical-experimental framework to identify which parameters influence the initiation of interface damage. The results of this parameter study are used in chapter 4 to investigate a novel technique for pre-conditioning the polymer-coated steels via rolling (prior to can production) to delay or even prevent interface damage. In chapter 5, a numerical framework is developed to enable study of deformation-induced interface roughening and polymer-steel interface damage in industrial forming processes where in-situ measurements of the steel surface height profile are infeasible. The developed framework is applied to study the polymer-steel interface in tension and compression. Finally, in chapter 6, conclusions are drawn and recommendations for future research are given.

QUANTIFICATION OF THREE-DIMENSIONAL SURFACE DEFORMATION USING GLOBAL DIGITAL IMAGE CORRELATION

Abstract
A novel method is presented to experimentally quantify evolving surface profiles. The evolution of a surface profile is quantified in terms of in-plane and out-of-plane surface displacements, using a Finite Element based Global Digital Image Correlation procedure.
The presented method is applied to a case study, i.e. deformation-induced surface roughening during metal sheet stretching. The surface roughness was captured in-situ using a confocal optical profiler. The Global Digital Image Correlation method with linear triangular finite elements is applied to track the three-dimensional material movement from the measured height profiles. The extracted displacement fields reveal the full-field kinematics accompanying the roughening mechanism. Local deviations from the (average) global displacements are the result of the formation, growth, and stretching of hills and valleys on the surface.
The presented method enables a full-field quantitative study of the surface height evolution, i.e. in terms of tracked surface displacements rather than average height values such as Root-Mean-Square or height-height correlation techniques. However, the technique does require that an initial surface profile, i.e. contrast, is present and that the contrast change between two measurements is minimal.

2.1   Introduction

A change in surface height profile is characteristic for many mechanical phenomena. For example, during cyclic fatigue loading of many metals, surface relief shows steps in the outer surface due to the extrusion and intrusion of plastic slip bands [46, 51]. Likewise, many creep experiments reveal significant grain boundary sliding, causing changes in the local surface height [23]. Also, in a uniaxial tensile test, the surface height profile of a metal locally changes, due to the crystallographic orientation differences between grains and dislocations escaping at the free surface [54, 56]. As a final example, surface height profile evolution occurs in contact and wear problems [65]. In all these examples, pronounced local variations in the surface height appear. Quantifying the in-plane and out-of-plane evolution of the surface height profile can provide valuable information on

the underlying mechanisms.

In the case of the deformation-induced surface roughening, which is found in many metals, it may be important to accurately determine the local deformation at the metal surface. This is particularly the case for polymer-coated steels used for food and beverage packaging (Fig. 2.1). This material is deformed in an industrial process using subsequent deep drawing, deep redrawing, and wall ironing to produce a can or canister. Compared to the traditional production process, which consists of first producing a steel can and then applying the coating, the use of pre-coated packaging steel leads to not only a 30% reduction of energy consumption and CO_2 emission, and a reduction of process water consumption, but also a reduction of solid waste to practically zero [1]. Unfortunately, however, pre-coating the steel comes with a number of challenges, since the coating undergoes the same deformation steps as the steel. As previous work by Boelen et al. [9], Van den Bosch et al. [14] and Fedorov et al. [28] showed, the interface adhesion is strongly influenced by deformation, and even though damage is often not optically visible after can production, the damage may become apparent during the prolonged shelf-life of the product. This is not desirable, since application for food packaging demands that the material does not exhibit any damage on the inside of the can, even after a relatively long shelf-life period, since this triggers corrosion and compromises the quality of the can content [9, 14].
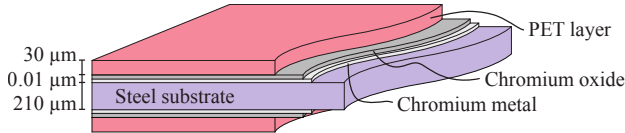
Figure 2.1: Different material layers in a polymer-coated steel (after [15]).

A possible cause of interface damage is the deformation-induced heterogeneous change in surface height of the steel. It is well known that the free surface of a polycrystalline metal roughens when it is deformed, due to crystallographic orientation differences between grains and other plasticity related phenomena. This roughening occurs over a wide range of length scales, ranging from the nanoscale to the size of multiple grains, depending on deformation conditions and material properties (see Fig. 2.2) [54].

Many different techniques for visualizing a surface topography are found in literature, e.g. stylus-type techniques, Atomic Force Microscopy (AFM), optical techniques (confocal and interferometry) [14, 54, 56, 59, 65].

A surface topography, and the change thereof, is typically characterized by average height values, e.g. Root-Mean-Square (RMS), average (AVG), and maximum peak-to-valley (MPV) [54, 56, 59, 65]. Another characterization method is the statistical height-height correlation method [14, 67].

While these techniques give insight into the amplitude of the height change and how the (average) height evolves, they do not provide actual information on local material deformation. This shortcoming was circumvented by Van Tijum et al. [67]. In contrast to using local surface deformations, they used a numerically generated out-of-plane deformation and a global in-plane deformation to predict the interface integrity of a polymer-coated steel. However, while these simulations give valuable insight into the effect of roughening on the adhesion between the polymer and the steel, the authors did not take into account the local evolving deformation fields that resulted from the steel roughening (e.g., due to the evolving rotation of grains).

Figure 2.2: Schematic examples of roughening phenomena, (a) sub-grain roughening (e.g. crystallographic slip steps) and (b) grain-scale roughening (orange peel) (c) poly-grain-scale roughening (ridging); scale-bars indicate the typical scale of the phenomenon.

This chapter presents a new methodology, which uses Global Digital Image Correlation (GDIC) to track three-dimensional surface deformations from evolving surface height profiles. The method is independent of the measurement t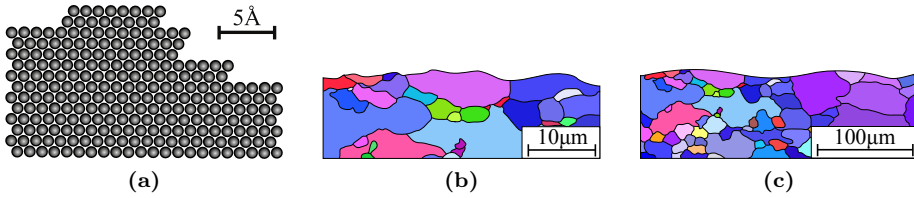echnique used to obtain the profiles, and the methodology is verified using well-defined displacement fields and measured height profiles of a steel surface. A case study was used to validate the technique, i.e. the deformation-induced surface roughening of a polymer-coated steel during a uni-axial tensile test. The surface height profile is captured in-situ using confocal microscopy. This case study was chosen because of its complexity, i.e. a) the initial surface roughness of the steel is smooth in the rolling direction of the steel, creating a low (height) contrast image in this direction, b) the steel shows Lüder-bands in a uniaxial tensile test, which is accompanied by a sudden change in the surface profile, c) the surface profile continuously changes when the deformation is increased, due to the deformation-induced roughening, and d) compared to other profilometers (e.g. AFM), the confocal profiler has a relatively low number of pixels. Confocal microscopy is used in the presented work, because the technique is well suited for measuring an evolving surface height profile in-situ. Other techniques that can be applied within the presented framework are, for example, AFM, stereo-correlation microscopy, and X-ray tomography. These techniques are also capable of measuring a surface profile.

This chapter is organized as follows. First, in section 2.2, the GDIC method is explained in detail, followed by a derivation of the equations and some aspects regarding its implementation. In the next section, an extensive verification analysis of the GDIC method is given for several well-defined virtual experiments. The validation experiments performed with the polymer-coated steel are discussed in section 2.4. The chapter ends with some concluding remarks.

2.2 Global Digital Image Correlation

2.2.1 Background and motivation

Digital Image Correlation (DIC) is a well-established method to extract material displacement from images. Within the framework of DIC there are two methodologies, i.e. "local" DIC and "global" DIC (GDIC) [37]. Local DIC is the traditional, older, and widely used method, while GDIC was more recently developed and is less well-known. The difference between the two methodologies is that in GDIC some properties of the kinematics of the problem are assumed to be known (e.g. continuity of the displacement field), and the displacement field is calculated using the entire field of view (FoV), rather than local

facet information. The fundamental basis of DIC is the conservation of brightness, i.e. the image contrast of a material point does not change between two images.

However, the assumption of brightness conservation is almost always violated when using experimentally measured images. This violation occurs, for example, due to (a) the formation of slip steps on a steel surface in the presence of large deformations, affecting light reflection, (b) out-of-plane sample motion as a result of bending or the Poisson's Ratio, (c) the camera and sample not being perpendicular, (d) fluctuations in the light-source, (e) noise stemming from the used camera, (f) geometric distortions from SEM scanning, (g) pattern evolution, and more [4, 50, 61, 63].

As such, a change in grayscale or height value does not strictly relate to motion or deformation of the material in the experimental images. To reduce or deal with this change in image contrast, several methods were developed, e.g averaging several images, or applying corrections functions, or incrementally applying the deformation to prevent large changes between two images, or by inserting some kinematics into the solution procedure [4, 50, 61, 69]. The latter method is used in GDIC. Hild and Roux [38] have shown that Global DIC generally out-performs local DIC due to the assumed kinematics, which reduce the sensitivity to changes in brightness and restricts the solution space. In all cases, an optimization algorithm is applied to find the displacement field iteratively, minimizing the contrast difference between the two images.

Measured surface height profiles are two-dimensional (or one-dimensional) images, where the pixel value indicates a local height value at the pixel location in a spatial frame. This requires a DIC method capable of extracting the three-dimensional material displacements from these "Quasi-3D" spatial height images. The available DIC methodologies have been developed for two-dimensional and three-dimensional (optical and SEM) images (also known as *Digital Volume Correlation*), with gray-valued pixels or voxels, respectively [5, 50]. So far, exploiting spatial height profiles to extract material displacement fields has only been done by Vendroux et al. [71] to obtain the three-dimensional displacement fields from Scanning Tunneling Microscopy (STM) data. The local DIC methodology was adapted to allow for out-of-plane movement by adding the out-of-plane displacement to the degrees-of-freedom. As a result, the three-dimensional displacement field could be extracted from the STM profiles. The method was applied to rigid body rotation. However, no (gradual) change in roughness pattern was tracked using this methodology. Later, Knauss et al. [43] showed that including the out-of-plane displacement is vital when using height profiles to determine the in-plane displacements. Furthermore, height profilometry has also been used in the GDIC method to determine the stress intensity factors around a crack tip from AFM height profiles by Han et al. [36]. The method used was Integrated DIC (I-DIC), where a-priori kinematic information of the crack tip intensity factors is used in the GDIC solution procedure. This a-priori information is typically not available when attempting to determine the material displacements from spatial height profiles. It is not known beforehand where material points will move, since this depends on many different properties, e.g. in the case of deformation-induced roughening this depends on grain orientation and size, material, etc. Thus, I-DIC methods cannot be applied trivially here. A Finite Element based GDIC method (FE-DIC) does not require a-priori knowledge of the kinematics, except for the assumed C0 continuity of the used finite element shape functions. A Quasi-3D FE-DIC method allows tracking of material displacements in evolving surface height profiles. FE-DIC has been applied before on two-dimensional optical images [8, 30, 44]; however, the method has not yet been extended to Quasi-3D height profiles.

2.2.2   Quasi-3D FE-DIC for spatial height profiles

The goal in Quasi-3D FE-DIC is to identify the displacement field, $\vec{u}(\vec{x}_0) = \vec{u}_{xy}(\vec{x}_0) + u_z(\vec{x}_0)\vec{e}_z$, with $\vec{u}_{xy}(\vec{x}_0) = u_x(\vec{x}_0)\vec{e}_x + u_y(\vec{x}_0)\vec{e}_y$, that correlates two height images, namely a reference image, $f(\vec{x}_0)$, and a "deformed" image, $g(\vec{x}) = g(\vec{x}_0 + \vec{u}_{xy}(\vec{x}_0))$. Here, an image in mathematical terms is a matrix of spatial pixel positions, $\vec{x}_0$ or $\vec{x}$, and a matrix of scalar pixel *height values*. This goal, schematically shown in Fig. 2.3(a), can be written at the pixel level as

$$f(\vec{x}_0) - g(\vec{x}_0 + \vec{u}_{xy}(\vec{x}_0)) + u_z(\vec{x}_0) = \eta(\vec{x}_0), \quad \forall \vec{x}_0 \in \mathcal{B}_0, \tag{2.1}$$

where $\eta(\vec{x}_0)$ contains the residual difference between the two images, e.g. measurement noise, and $\mathcal{B}_0$ is the region of interest. The traditional assumption of brightness conservation is thus redefined to allow for some *minor* changes in the surface height profile, i.e. the image contrast.

(a) Schematic of the problem to be solved.   **(b)** Element discretization.
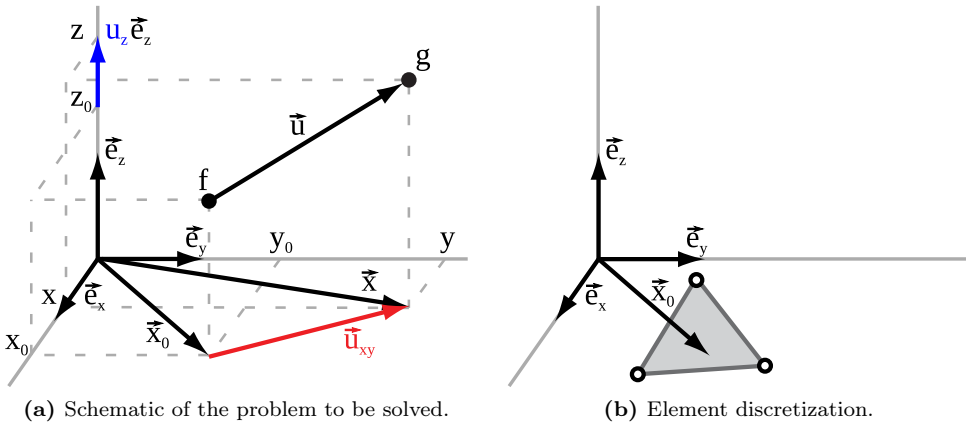
Figure 2.3: Problem description.

The goal is thus to find the displacement field that minimizes this residual difference within $\mathcal{B}_0$. Thus, Eq. (2.1) is set up for each pixel within $\mathcal{B}_0$. For each pixel with one measured quantity (i.e. its height), there are three unknowns (i.e. u_x, u_y and u_z). In order to find the displacement field, a finite element discretization is applied, which greatly reduces the number of unknowns by assuming that the kinematics can be captured by means of the adopted finite element discretization.

In each element, the displacement $\vec{u}(\vec{x}_0)$ of an internal point is interpolated between the displacement, $\underline{u}$, of n nodal points, using n shape functions, φ, which are a function of the local isoparametric coordinate, $\vec{\xi}$,

$$\vec{u}(\vec{x}_0) \approx \sum_{k=1}^{n} \varphi_k(\vec{\xi}(\vec{x}_0))\vec{u}_k = \underline{\varphi}^{\mathrm{T}}(\vec{\xi}(\vec{x}_0))\underline{u}. \tag{2.2}$$

After assembling all the elements, and taking into account the continuity of the nodal displacements, the total system (in components) reads

$$\underline{\eta}(\underline{x}_0) = \underline{f}(\underline{x}_0) - \underline{g}\left(\underline{x}_0 + \underline{\underline{M}}(\underline{x}_0)\underline{\underline{A}}\underline{u}\right) + \underline{\underline{M}}(\underline{x}_0)\underline{\underline{B}}\underline{u}, \tag{2.3}$$

$$\underline{u}_{xy} = \underline{\underline{A}}\underline{u} \quad \& \quad \underline{u}_z = \underline{\underline{B}}\underline{u}. \tag{2.4}$$

The size of $\underset{\sim}{f}$, $\underset{\sim}{g}$ and $\underset{\sim}{\eta}$ is $(p \times 1)$, of $\underline{M}(\underset{\sim}{x}_0)$ is $(p \times 3n)$, of $\underline{A}$ and $\underline{B}$ is $(3n \times 3n)$ and of $\underset{\sim}{u}$ is $(3n \times 1)$, where p is the number of pixels. In general $3n \ll p$, whereby a solution can be obtained via the least-squares method, minimizing the error Φ with respect to the displacement field, i.e.

$$\underset{\underset{\sim}{u}}{\operatorname{argmin}}\left(\Phi(\underset{\sim}{u})\right), \quad \text{with } \Phi(\underset{\sim}{u}) = \underset{\sim}{\eta}(\underset{\sim}{u})^{\mathrm{T}}\underset{\sim}{\eta}(\underset{\sim}{u}). \tag{2.5}$$

Minimization using Eq. (2.5) gives

$$\underset{\sim}{\Psi}(\underset{\sim}{u}) = \frac{\partial \Phi}{\partial \underset{\sim}{u}} = 2\left(\frac{\partial \underset{\sim}{\eta}}{\partial \underset{\sim}{u}}\right)^{\mathrm{T}}\underset{\sim}{\eta}(\underset{\sim}{u}) = \underset{\sim}{0}. \tag{2.6}$$

To solve this non-linear equation in the degrees-of-freedom, $\underset{\sim}{u}$, an iterative procedure is applied. First, Eq. (2.6) is linearized with respect to the degrees-of-freedom,

$$\underset{\sim}{u}^{(i+1)} = \underset{\sim}{u}^{(i)} + \delta\underset{\sim}{u}, \tag{2.7}$$

$$\underset{\sim}{\Psi}^{(i+1)} = \underset{\sim}{\Psi}^{(i)} + \frac{\partial\underset{\sim}{\Psi}^{(i)}}{\partial\underset{\sim}{u}}\delta\underset{\sim}{u} = \underset{\sim}{0}. \tag{2.8}$$

Here, i is the iteration index. Expressions for the separate contributions in Eq. (2.8) are

$$\underset{\sim}{\Psi}^{(i)} = -2\underline{K}^{(i)\mathrm{T}}(\underset{\sim}{x}_0)\left(\underset{\sim}{f}(\underset{\sim}{x}_0) - \underset{\sim}{g}^{(i)}(\underset{\sim}{x}_0)\right), \tag{2.9}$$

with

$$\underset{\sim}{g}^{(i)}(\underset{\sim}{x}_0) = \underset{\sim}{g}\left(\underset{\sim}{x}_0 + \underline{M}(\underset{\sim}{x}_0)\underline{A}\underset{\sim}{u}^{(i)}\right) - \underline{M}(\underset{\sim}{x}_0)\underline{B}\underset{\sim}{u}^{(i)}, \tag{2.10}$$

$$\frac{\partial\underset{\sim}{\eta}^{(i)}}{\partial\underset{\sim}{u}} = -\frac{\partial\underset{\sim}{g}^{(i)}}{\partial\underset{\sim}{x}}\frac{\partial\underset{\sim}{x}}{\partial\underset{\sim}{u}} + \underline{M}(\underset{\sim}{x}_0)\underline{B},$$

$$= -\underline{\nabla g}^{(i)}(\underset{\sim}{x}_0)\underline{M}(\underset{\sim}{x}_0)\underline{A} + \underline{M}(\underset{\sim}{x}_0)\underline{B},$$

$$= -\underline{K}^{(i)}(\underset{\sim}{x}_0), \tag{2.11}$$

and

$$\frac{\partial\underset{\sim}{\Psi}^{(i)}}{\partial\underset{\sim}{u}} = -2\underline{K}^{(i)\mathrm{T}}(\underset{\sim}{x}_0)\frac{\partial\underset{\sim}{\eta}^{(i)}}{\partial\underset{\sim}{u}} = 2\underline{K}^{(i)\mathrm{T}}(\underset{\sim}{x}_0)\underline{K}^{(i)}(\underset{\sim}{x}_0). \tag{2.12}$$

Note that matrix $\underline{K}^{(i)}(\underset{\sim}{x}_0)$ contains the iterative gradient, $\underline{\nabla g}^{(i)}(\underset{\sim}{x}_0)$, which is a surface gradient, i.e. $\vec{\nabla}g \cdot \vec{e}_z = 0$. Substituting Eqs. (2.9) and (2.12) into Eq. (2.8) and rewriting yields

$$\delta\underset{\sim}{u} = \left(\underline{K}^{(i)\mathrm{T}}\underline{K}^{(i)}\right)^{-1}\underline{K}^{(i)\mathrm{T}}\left(\underset{\sim}{f} - \underset{\sim}{g}^{(i)}\right), \tag{2.13}$$

where $(\underset{\sim}{x}_0)$ was omitted for clarity. To save on computational cost, the iterative gradient, $\underline{\nabla g}^{(i)}(\underset{\sim}{x}_0)$ in $\underline{K}^{(i)}(\underset{\sim}{x}_0)$ is replaced by $\underline{\nabla f}(\underset{\sim}{x}_0)$, which does not require iterative updating, since it does not depend on the displacement field. This replacement leads to a slower convergence rate, as the gradients are only equal when the iterative solution approaches the real solution, near the end of the iterative procedure.

2.2.3 Image coarsening

As mentioned in the derivation of the GDIC system of equations, the solution is found iteratively. This procedure requires that the displacement is smaller than the dominant correlation length in the roughness pattern, e.g. the grain size. Thus, an adequate initial guess is required in order to converge to the correct solution. This is accomplished by creating so-called "*coarse grained images*" [8]. The two images, $f(\vec{x}_0)$ and $g^{(i)}(\vec{x}_0)$, are coarsened using so-called "*superpixels*" consisting of 2×2, 4×4, 8×8, etc pixels. This coarsening eliminates the small-scale fluctuations. First, the system is solved for the largest superpixel size, which gives a coarse approximation of the displacement field. This field is next used as an initial guess for the second-largest superpixel size, and so on, until the original image is used. To keep the number of pixels within each element constant, a new mesh is used in each coarse grained image. All the presented results are obtained using three coarsening steps, i.e. the maximum superpixel size was set to 8×8 pixels.

2.2.4 Finite element discretization

The finite elements used in the current framework can in principle be taken arbitrarily, but the choice made, and the discretization used, do control the constraints on the kinematics of the field to be identified. In all of the following examples and results, linear triangular finite elements are used.

Following [38], the elements of the edges of the FoV are increased in size, such that the corner and edge elements contain four and two times more pixels than the inner elements, respectively. This increases the stability of the FE-DIC calculation, due to the reduction in degrees-of-freedom per pixel in the edge elements.

2.3 Verification analysis

To gain insight into the quality and efficiency of the method and its implementation, several (virtual) experiments are performed on height profiles characteristic for the problem presented in section 2.4. Different mesh sizes are used to correlate the displacements and to study the discretization influence.

Two height profiles are used as image $f(\vec{x}_0)$ in the verification analysis, namely the initial and final roughness profile of a steel deformed by tension. These profiles were obtained using the experimental setup of the proof-of-principle experiments, described in Section 2.4.1. The height profiles are shown in Fig. 2.4. Note that these two profiles were obtained on different parts of the tensile sample. The initial roughness pattern (Fig. 2.4(a)) clearly shows (horizontal) grooves induced by rolling steel sheet material, while the final roughness pattern (Fig. 2.4(b)) is dominated by the deformation-induced roughness. Yet, the initial surface roughness pattern remains visible. The difference between these patterns is large and it needs to be verified if the implemented FE-DIC method properly handles this.

First, the error due to measurement noise of the experimental setup, combined with the correlation procedure, is investigated. To this purpose, multiple height measurements are performed on the same location of an undeformed and deformed steel tensile sample. These profiles are then used as images $f(\vec{x}_0)$ and $g(\vec{x})$ to calculate the displacement field, i.e. two undeformed or two deformed profiles.

The resulting deviation from zero displacement due to the measurement noise, as calculated by the correlation algorithm, for different mesh sizes is shown in Fig. 2.5(a). The error increases with decreasing element size (reduced number of pixels per element). The increased number of degrees-of-freedom increases the sensitivity to noise in the FE-DIC calculation. The errors in the x and y displacement are noticeably larger than the error in the z displacement. This is because a) no interpolation is required for a displacement in z direction in order to obtain the iterative deformed image $\tilde{g}(\vec{x}_0)$, b) the resolution in z is much higher (order of 20 [nm] compared to 332 [nm] in x and y), and c) the gradient is a surface gradient and thus only defined in-plane.

Comparing the calculated error in the x and y displacement for the initial surface roughness shows that the error in x is larger. This is explained by the fact that the roughness profile is initially smoother in x direction (RD) than in y direction (TD), see Fig. 2.4(a). This difference in error is smaller in the case of the final roughness profile, as the roughness profile is then nearly identical in both directions.

The mean error remains below 10% of the pixel dimension (332 [nm]) in both cases, which is relatively small, i.e. in the order of the measurement noise ($\sim$20 [nm]), considering the large number of degrees-of-freedom in the Quasi-3D FE-DIC method.

(a) Initial roughness.   **(b)** Final roughness.
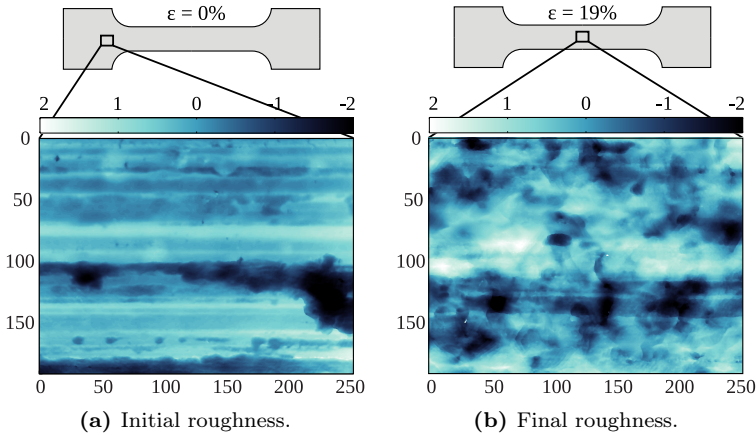
Figure 2.4: Two height profiles of a packaging steel, (a) the initial rolling roughness, and (b) the roughness after a tensile test close to fracture; the profiles are used in the verification analysis as reference image $f(\vec{x}_0)$; dimensions are in microns; horizontal and vertical direction correspond to the x and y directions, respectively; colors indicate the local height value.

Next, the error as a result of the interpolation algorithms used in the FE-DIC calculation is investigated. This is accomplished by virtually displacing the two roughness profiles (Figs. 2.4(a) and 2.4(b)) uniformly by 166 [nm] (half the pixel dimension) simultaneously in x, y and z, creating two new (virtually deformed) images, g. This displacement is a worst case scenario for any interpolation algorithm [8, 37]. This deformed image is then used in the FE-DIC calculation. The resulting error, presented in Fig. 2.5(b), contains two contributions, 1) the error due to the interpolation used to obtain the deformed image, and 2) the error due to the iterative interpolation required to obtain the displacement fields in the FE-DIC calculation.

The results clearly show that the calculated displacements in the FE-DIC algorithm become less accurate when the element size is decreased. The explanation lies in the increase of the number of degrees-of-freedom (nodes) in the system. This increases the sensitivity to errors in the interpolation algorithm. Similar to the error due to measurement noise, the in-plane displacements $(x,\ y)$ are more sensitive to the errors in the interpolation compared to the out-of-plane displacement (z). The error for the initial and final roughness profiles, in this case, shows a similar trend and value. Compared to the error found in the analysis of the experimental setup, the error is smaller (less than 2%), since the displacements used to construct $g(\vec{x}_0)$ were virtual and noise-free.

So far, only rigid body displacements were used to characterize the experimental error and interpolation error. A more realistic displacement field, including locally heterogeneous deformations at the surface, is investigated next. The virtual displacement field prescribed, again simultaneously, to the roughness profiles (Figs. 2.4(a) and 2.4(b)) is shown in Fig. 2.6(top). To simulate measurement noise, random white noise with an amplitude of 20 [nm] was added to the virtually displaced height profile.

The resulting error is shown in Fig. 2.5(c). The trends in the error for the x and y directions are similar. Decreasing the element size initially decreases the error value to a minimum. Further decrease of the element size once more increases the error. Smaller elements can more accurately describe the prescribed complex non-linear displacement field. However, the interpolation error and noise sensitivity become increasingly dominant upon further reduction of the element size.

A different minimum results when comparing the errors in the x and y displacement for the initial surface profile. In y direction (TD), the minimum is found at approximately 450 pixels per element (30 pixels in each direction), while no clear minimum error is visible in x direction (RD). This difference is due to the smoothness of the initial roughness profile in x direction, see Fig. 2.4(a). Comparing the error in the z displacement with the errors in x and y displacement once again confirms that the error in z is significantly smaller.

The calculated displacement fields for the deformed reference image (Fig. 2.4b) and a mesh containing approximately 450 pixels per element (near the optimum) are shown in Fig. 2.6(bottom). Comparing the prescribed virtual displacement fields (Fig. 2.6(top)) with the calculated fields shows that the FE-DIC method accurately captures the prescribed heterogeneous displacement field. However, some differences can be seen as a result of the linear interpolation functions of the triangular elements. Furthermore, comparing the difference between the virtual and calculated displacement fields in x and y direction with the displacement field in the z direction shows that the z displacement field is more accurately captured. Thus, the conclusion drawn from the average error in Fig. 2.5 is confirmed, i.e. the error in the calculated z displacement field is smaller than in x and y direction.

From this error analysis, an optimum element size can be identified. The element size must be sufficiently small to capture the fine-scale fluctuations of the displacement field. However, reducing the element size leads to an increase in the number of degrees-of-freedom, which in turn increases the sensitivity to measurement noise. Based on the error analysis discussed above, the optimum element size is around 450 pixels per element for the particular problem considered here. This translates to an element size of approximately 10 [µm] by 10 [µm] in the case of the confocal optical height profiles used here. For this element size, the average error in the calculated displacement fields is below 10% of a pixel dimension for both the initial and the final surface profile. The optimal element size is thus relatively large compared to the spatial resolution of the measured profiles, i.e.

the pixel size of 332 [nm]. Clearly, to reduce the error to a minimum, a large number of data points (pixels) per DOF is required. A smaller element discretization is achievable at the expense of increasing the error.
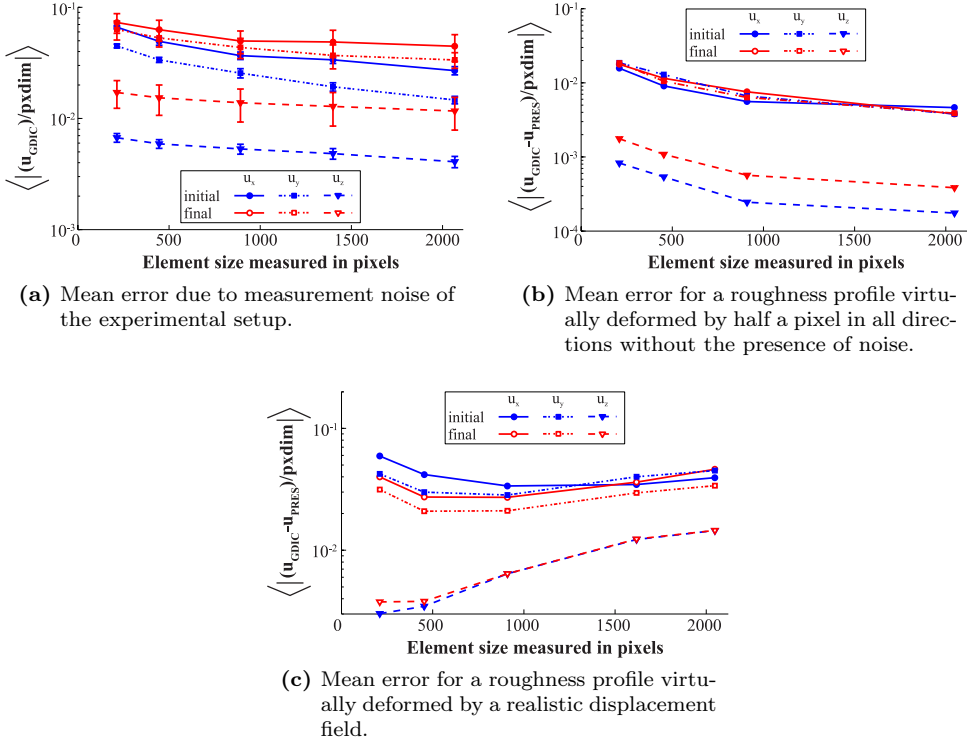

(a) Mean error due to measurement noise of the experimental setup.

(b) Mean error for a roughness profile virtually deformed by half a pixel in all directions without the presence of noise.

(c) Mean error for a roughness profile virtually deformed by a realistic displacement field.

Figure 2.5: Mean error in the FE-DIC calculation for three test cases, expressed as a fraction of a pixel, where a pixel is 332 [nm].

2.4 Proof-of-principle experiments

2.4.1 Methodology

The material investigated is a polymer-coated steel known as TH340. The material consists of a continuously annealed, single reduced, DWI (draw-redraw-wall ironing) quality aluminium-killed low carbon ferritic, electrolytic chromium coated steel (ECCS) sheet, 210 [µm] thick, lacquered with a protective coating on each side. Tensile samples, with the rolling direction (RD) aligned with the tensile axis, were produced using standard milling. To reduce edge effects, a stack of 5 samples was produced and the top and bottom samples were not used. The tensile samples had a gauge length of 20 [mm] and a width of 4 [mm].

Uniaxial tensile tests show that the material forms a Lüders band after the onset of plasticity, i.e. plasticity initiates in a localization band on one side of the tensile sample, which extends towards the other side. The entire sample deforms plastically after an engineering strain of $\varepsilon \approx 5\%$. Failure of the material occurs at $\varepsilon \approx 19\%$.

(a) Virtual u_x.   **(b)** Virtual u_y.   **(c)** Virtual u_z.

(d) Calculated u_x.   **(e)** Calculated u_y.   **(f)** Calculated u_z.
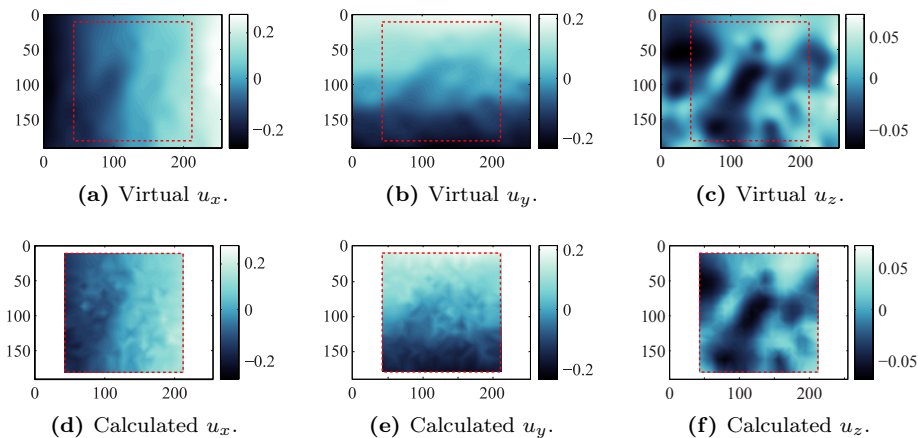
Figure 2.6: (top) Realistic virtual displacement field used in the error calculation; (bottom) displacement fields calculated by the FE-DIC procedure; displacements in microns; x direction is horizontal; dashed red line indicates the data region used in the FE-DIC calculation.

The tensile tests were performed on a Kammrath&Weiß micro tensile stage, using a 500N load cell. The strain rate was set to $5 \cdot 10^{-4}$ [s^{-1}]. The surface profile was measured in-situ using a Sensofar PLμ2300 confocal optical profiler with a 50x objective. The image pixel dimensions are 332 [nm] $\times$ 332 [nm]. The accuracy of the height measurement is in the order of 20 [nm]. The experimental setup is shown in Fig. 2.7.

It is assumed that the thin polymer layer is sufficiently compliant and hence does not influence the roughening of the steel surface. Therefore, the polymer coating is removed prior to the experiment to improve the accuracy of the height measurement of the steel surface. This is accomplished by using N-Methyl-2-Pyrrolidone (NMP) in a two-step process, due to the large amounts of polymer that have to be removed. The NMP is first heated to 80 [°C], removing most of the coating. The coating residuals are removed at 130 [°C].

The Quasi-3D FE-DIC method requires 1) the presence of an initial surface profile, which is the case here, as shown in Fig. 2.4(a); and 2) that the contrast change between the two correlated height profiles is small. To guarantee that the second demand is met, an incremental method was adopted. The uniaxial tensile experiments were performed in a stepwise manner. Prior to the tensile test, a height measurement was made on the sample. This defined the FoV for the measurement and the undeformed initial roughness. Next, a loading step of $\Delta\varepsilon = 0.25\%$ at the prescribed strain rate was performed. Hereafter, a new height measurement was made. The FoV has shifted, as it does not remain centered on the sample. This shift was corrected by comparing the two height profiles and moving the FoV back into view. After this correction step another height measurement was performed, which was stored for later post-processing in the FE-DIC correlation. This completed the measurement cycle and a new incremental loading step was performed. This process was continued until the material started to fail. Thus, a height profile was measured after each strain increment of $\Delta\varepsilon = 0.25\%$, during which the changes in height were progressive and small. This procedure is schematically shown in Fig. 2.8
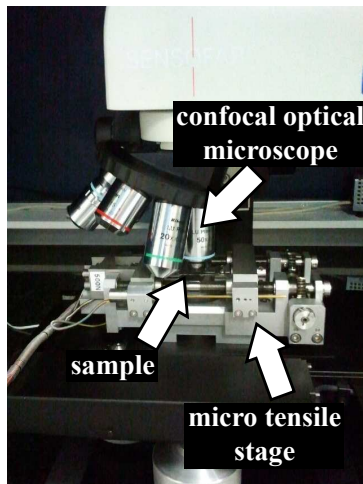
Figure 2.7: Experimental setup.

2.4.2 Results

Surface roughness evolution

Height profiles obtained in-situ during the tensile test are shown in Fig. 2.9(left). The initial rolling-induced roughness is shown in Fig. 2.9(a). Between 0% and 2.75% global strain, no real change in surface roughness is noticed, as the material within the FoV deforms elastically, see Fig. 2.9(c).

Plasticity initiates locally at ∼2.75% of global (engineering) strain on the sample. This strain is relatively large, due to Lüdering, which delays the local plasticity initiation within the FoV. An abrupt change in roughness appears, i.e. a new roughness pattern overtakes the existing initial surface roughness (Fig. 2.9(e)). This pattern consists of hills and valleys throughout the FoV. Also visible is a slight rotation of the material within the FoV, due to the formation of a shear band, indicated by the dashed lines.

When the strain is increased further, this new roughness pattern grows in height direction, see Figs. 2.9(g) and 2.9(i). The initial surface roughness slowly disappears with increasing deformation, as the new pattern becomes more dominant. No clear formation of new hills and valleys is observed at higher strains. The material slowly realigns the RD with the tensile direction with increasing strain.

Material surface deformation

An initial finite element mesh (see Fig. 2.9(b)), using linear triangular finite elements, is used to discretize the image of the undeformed height profile (Fig. 2.9(a)). The element size equals approximately 450 pixels per element, as discussed in section 2.3. The initial mesh does not cover the full FoV, as a linearly growing displacement is expected in the x direction during the tensile test. FE-DIC calculations are performed in an incremental manner, starting with the initial height profile and the first deformed profile. The latter profile is used as the reference image, $f(\vec{x}_0)$, in the next increment. The location of the element nodes is updated between each step. The incremental procedure is schematically shown in Fig. 2.8. This incremental way of calculating the displacement field leads to

an incremental error, as the error from the previous increment is added to the error of a new increment. Another possibility is calculating the displacement field using the initial roughness profile as the reference image. However, the displacement field cannot be determined accurately when the two profiles used in the FE-DIC calculation drastically change, which is the case here (see also Figure 2.9). Thus, while using the reference image will initially give accurate results, the accuracy will decrease when the deformation increases.
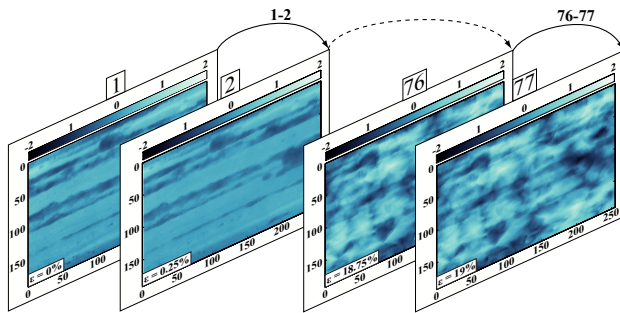

Figure 2.8: Schematic of the incremental FE-DIC calculation procedure; note that the strain increment between two sequential images was $\Delta\varepsilon = 0.25\%$.

The FE-DIC discretization at different levels of strains is shown on the right side of Fig. 2.9. The initial mesh remains more or less undistorted in the elastic regime (Figs. 2.9(b) and 2.9(d)). A large mesh update results at the onset of plasticity (Fig. 2.9(f)). The small rotation noticeable in the experimental height profiles (see the dashed lines in Figs. 2.9(a) and 2.9(e)) is captured by the correlation, see Figs. 2.9(d) and 2.9(f). Further increase in the tensile strain does not lead to significant changes in the mesh. Comparing the discretization close to material failure (Fig. 2.9(j)) with the initial one (Fig. 2.9(b)) clearly reveals a positive strain in the x direction (tensile direction) and a negative strain in the perpendicular y direction.

The material displacements in the out-of-plane (z) and tensile direction (x) of the blue, black and red nodes on the right side of Fig. 2.9 are shown in Fig. 2.10. The profiles reveal the positive strain in the rolling (tensile) direction, i.e. points on the left side move to the left and vice versa. The hills and valleys formed on the material surface are captured, as well as their growth in amplitude as the strain increases.

The calculated three-dimensional displacement fields for the profiles taken just before and after the onset of plasticity are shown in Fig. 2.11. The deformation is clearly not homogeneous, as the strain locally fluctuates. The strain in x and y direction can be seen as a displacement gradient in x and y. The rotation seen in the experimental profiles (see the dashed lines in Figs. 2.9(c) and 2.9(e)) is also visible in the gradient, i.e. the gradient is not strictly in RD and TD for x and y, respectively, but rather rotated. The displacement field in z direction clearly shows the formation of hills and valleys during the onset of plasticity.

(a) profile, ε=0%.

(b) mesh, $\varepsilon = 0$%.

(c) profile, $\varepsilon = 2.75$%.

(d) mesh, $\varepsilon = 2.75$%.

(e) profile, $\varepsilon = 3$%.

(f) mesh, $\varepsilon = 3$%.

(g) profile, $\varepsilon = 12$%.

(h) mesh, $\varepsilon = 12$%.

(i) profile, $\varepsilon = 19$%.

(j) mesh, $\varepsilon = 19$%.
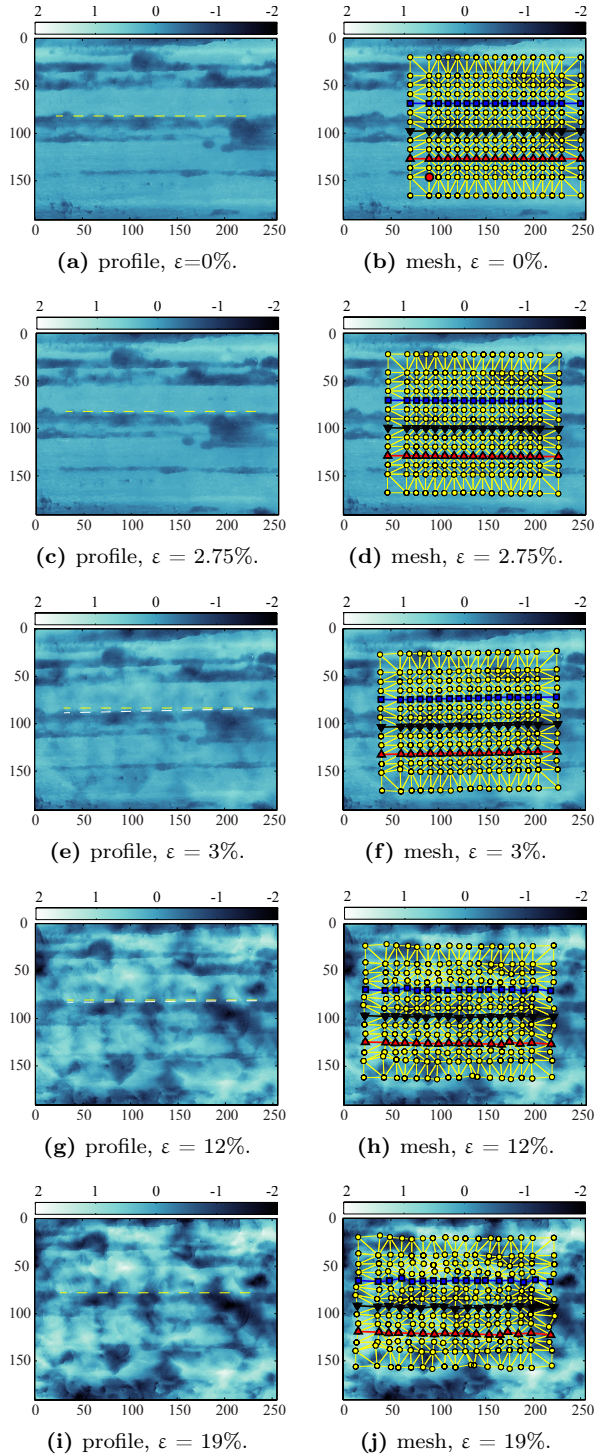
Figure 2.9: (left) Surface height profiles at different strain levels during the tensile experiment, dashed lines indicate the local material rotation; (right) the corresponding correlated FE-DIC solution; the blue, black and red nodal lines are used in Fig. 2.10; the red circular node shows sensitivity to the steep height change of the initial roughness (see also Fig. 2.11); all values are in microns, the tensile (x) direction is horizontal and the colors indicate the local height.

(a) Blue line in Fig. 2.9.

(b) Black line in Fig. 2.9.

(c) Red line in Fig. 2.9.
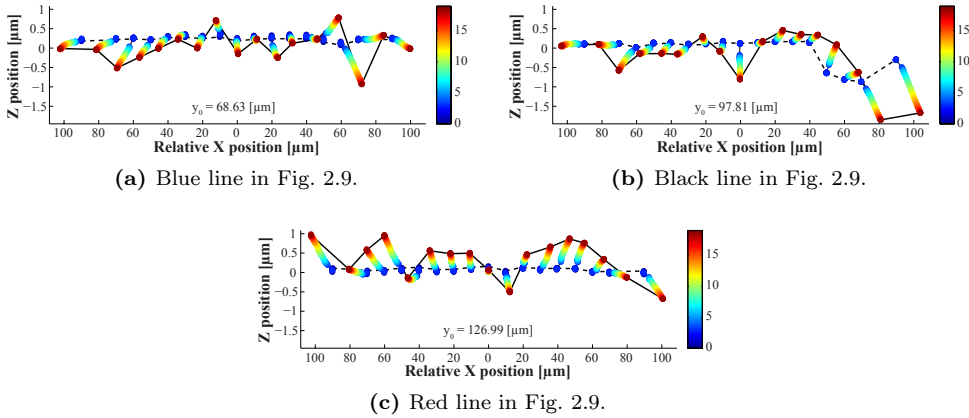
Figure 2.10: The evolution of the surface roughness for the blue, black and red nodes (see right side of Fig. 2.9) in x and z direction; colors indicate the global strain level.

Note that the displacement field around the red circular node in Fig. 2.9(b) strongly differs from the surrounding displacement field, see the yellow arrow in Fig. 2.11(b). This node is initially positioned at an almost vertical slope in the roughness profile. During the onset of plasticity, a new roughness pattern forms over the existing pattern. As a result, the displacement of this node is calculated erroneously, as the node clearly moves away from the material it is supposed to track (see also Fig. 2.9(f)). Clearly, the FE-DIC calculation is sensitive to a strong vertical slope in the surface profile, because the confocal profiler cannot accurately measure these slopes.
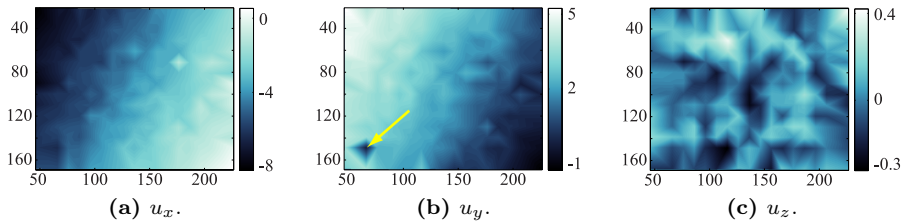

(a) u_x.

(b) u_y.

(c) u_z.

Figure 2.11: Calculated displacement fields for the height profiles just before (Fig. 2.9(d)) and after (Fig. 2.9(f)) plasticity initiates (around 3% strain); the yellow arrow indicates the location of the red circular node in Fig. 2.9(b); the values are in microns, the tensile (x) direction is horizontal and the colors indicate the respective displacement amplitudes.

A comparison between the measured roughness profile and the calculated roughness profile for two data lines perpendicular to the RD at different strains is shown in Fig. 2.12. The calculated profile was obtained by adding the incremental full-field FE-DIC displacement field to the initial surface profile. In the elastic regime (Fig. 2.12(a)), the roughness pattern is captured accurately by the FE-DIC calculation. After the onset of plasticity, some differences are seen between the calculated and measured profile. These differences are initially small (Fig. 2.12(b)), but increase for larger deformation. At the end of the
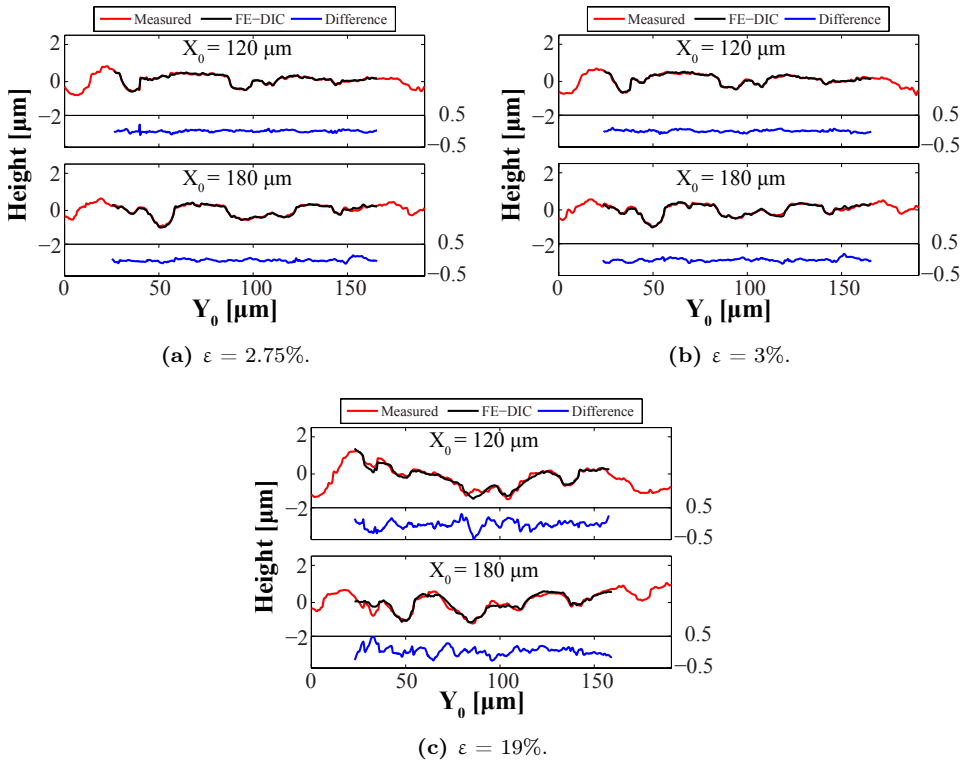
Figure 2.12: Comparison between a cut out of two lines perpendicular to the RD of the measured roughness profile and the roughness profile which is obtained via FE-DIC displacement fields at different strains during the tensile experiment.

experiment, the calculated and measured profiles show clear differences (Fig. 2.12(c)). Clearly, some of the small hills and valleys that form are not captured by the finite element discretization. However, the trend in the roughness profile is captured accurately.

2.4.3   Discussion

The error analysis shows that there exists an optimum value for the element size. This obviously limits the resolution of the roughening phenomena that can be resolved in the correlated displacement field. All phenomena that occur at a scale below the element size are constrained by the linear element shape functions. The validity thereof can be assessed in the residual height difference between the measured surface profile and the surface profile obtained with the calculated displacement fields. Examples of this difference were given in Fig. 2.12. If the element shape functions entirely resolved the real displacement field, only small differences would be visible between the two profiles, i.e. the measurement noise. This is not the case, however, since small peaks and valleys are seen in the measured surface profile, which are not captured by the calculation. Thus, some of the fine-scale details are not fully resolved and hence have to be viewed as non-random noise in the FE-DIC calculation. The elements initially have a size of approximately

10 [µm] by 10 [µm] (30 pixels in x and y direction), which is large compared to these small peaks and valleys.

To resolve these fine-scale details, either the element size or the pixel dimensions have to be reduced. The former gives rise to a larger correlation error, as discussed in section 2.3, whereas the latter depends on the imaging by the confocal optical microscope, i.e. the optical resolution is limited by the wavelength of the used light. Non-optical techniques, e.g. AFM, might be used to increase the details in the displacement field that are captured in the correlation. Resolving these fine-scale displacements may be important for some applications, e.g. when a steel surface roughens on a wide range of length scales [54]. Furthermore, an AFM can more accurately measure the steep slopes that are present on the initial surface profile (see also Fig. 2.9(a)) and thus possibly prevent the error seen in the calculation of the displacement field during the onset of plasticity (see the yellow arrow in Fig. 2.11b).

Another possibility is changing the finite element interpolation. Six-nodal triangular elements look promising, as the shape functions allow for quadratic changes in the displacement field within the elements. Quadratic finite elements have been used in the realistic test case described in section 2.3 for the final roughness profile (see Fig. 2.4b). The error in the calculation for both linear and quadratic triangular elements is shown in Fig. 2.13. Comparing the error in x and y direction shows that the difference between the linear and quadratic elements is relatively small for large elements, while the linear elements out-perform the quadratic elements for small elements. For the z displacement error it can be seen that the quadratic elements are more accurate up to small element sizes. The number of degrees-of-freedom per element for the quadratic triangular elements is larger, which leads to an increase in sensitivity to noise. However, for larger elements, the shape functions do allow for a more accurate description of the non-linear out-of-plane displacement field. Thus, depending on the required scale and expected displacement fields, quadratic elements can perform better. Note that the computational cost is significantly increased.
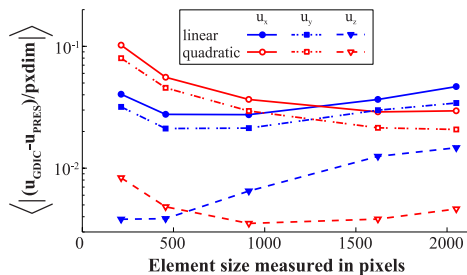
Figure 2.13: Comparison of the mean error for linear and quadratic elements for a roughness profile virtually deformed by a realistic displacement (see also section 2.3).

A comparison between the average values of the measured and calculated surface profiles, both for the Root-Mean-Square (R_{RMS}, Eq. (2.14)) and average (R_{AVG}, Eq. (2.15)) value, is shown in Fig. 2.14. Comparing the curves shows that the trend corresponds well. However, clear differences between the average values can be seen, especially at relatively small strains. These differences are explained by the finite element discretization. The element size is larger than some of the fine-scale details of the roughening phenomena. These fine-scale details initially contribute to the average surface values, thus explaining

the difference.   At large strains, the large-scale roughening phenomena dominate the average values. These phenomena are accurately captured by the FE-DIC calculation and thus the average values overlap. A comparison for the height-height correlation and the maximum peak-to-valley (MPV) value is not shown here, as the conclusion drawn is the same.

$$R_{RMS} = \sqrt{\langle \tilde{f}^2 \rangle} \tag{2.14}$$

$$R_{AVG} = \langle |\tilde{f}| \rangle \tag{2.15}$$

Correlating the height profiles before and after the onset of plasticity (see Figs. 2.9(c) and 2.9(e)) was difficult. In the elastic regime, the roughness pattern remains relatively constant (simple stretching only). This initial roughness pattern drastically changes in the plastic regime, where hills and valleys form at the surface. Correlating this sudden change in overall pattern is difficult, especially for fine meshes, due to the large number of degrees-of-freedom involved. The current experiment was performed stepwise with strain increments of $\Delta\varepsilon = 0.25\%$. This step size can be reduced in order to increase the number of height profile images during the early stages of plasticity and thereby decrease the amplitude of the incremental height changes.

Finally, note that the adopted incremental FE-DIC calculation technique (see Fig. 2.8) is prone to an incremental error. Different techniques have been developed in an attempt to decrease this error, e.g. the work of Tang et al. [62]. These methods may reduce this incremental error, while still being capable of calculating the displacement field after large changes in contrast have occurred due to the roughening phenomenon.
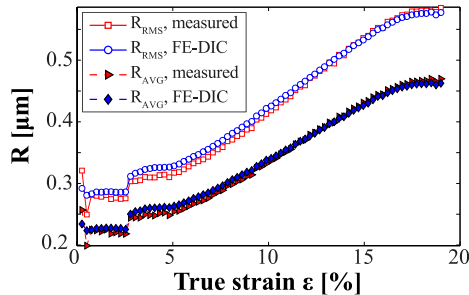

Figure 2.14: Comparison between the average values (RMS and AVG) of the height profiles obtained via the calculated displacement fields and the experimental profiles.

2.5   Conclusion

An experimental surface deformation measurement methodology has been presented, using a Finite Element based Global Digital Image Correlation (FE-DIC) technique. This methodology allows for full-field tracking of material displacements of an evolving surface, both in-plane and out-of-plane. This new way of characterizing an evolving surface height profile provides quantitative information for various surface deformation phenomena, and hence out-performs conventional methods using average height values. However, two requirements have to be met before the technique can be applied, i.e. a) the presence of an initial surface profile, i.e. contrast; and b) a minimal contrast change between the two correlated height profiles.

Accurate information on local material displacements is important in, for example, the case study used in this research. A polymer-coated steel has been investigated, where deformation-induced interface roughening has an important effect on the interface integrity. A proof-of-principle experiment has been performed. The local surface height profile of a sheet metal was measured in-situ as it evolves under applied uniaxial deformation and the FE-DIC method was applied to extract the local material displacements of the metal surface. This local deformation field can be used in numerical simulations of roughening-induced interfacial loading problems, directly affecting the local interface integrity.

NUMERICAL-EXPERIMENTAL ASSESSMENT OF ROUGHNESS-INDUCED METAL-POLYMER INTERFACE FAILURE

Abstract
A numerical-experimental method is presented to study the initiation and growth of interface damage in polymer-steel interfaces subjected to deformation-induced steel surface roughening. The experimentally determined displacement field of an evolving steel surface is applied to a numerical model consisting of a polymer coating and an interface layer. The measured displacement field is obtained with a Finite Element based Digital Image Correlation method.
The resulting simulations provide novel insights into the mechanical behavior of the polymer-steel interface during interface roughening. The appearance of local hills and valleys on the evolving steel surface results in local bands of intensified stress in the polymer layer. These localized deformation bands trigger interface damage, which grows as the surface deformation increases. Polymer aging initially delays the initiation of interface damage. However, for increased polymer ages the average interface damage increases. Likewise, the critical strain, at which the interface integrity is locally compromised, decreases.
The presented method allows for a detailed study of the interface integrity during deformation-induced steel surface roughening. With properly identified material parameters, it becomes possible to tailor the polymer-steel material properties to minimize interface damage during production and storage of cans or canisters, e.g. for food and beverages.

3.1   Introduction

3.1.1   Metal-polymer laminates

In recent years, metal-polymer laminates of electrolytic chromium coated steel (ECCS) sheets coated with a polymer layer (see Fig. 3.1(a)) have become increasingly popular for packaging of food and beverages. Producing cans or canisters from these pre-coated steels offers several advantages over the traditional production method. In the latter, a can is made from blank steel sheet after which it is lacquered with a protective coating on the inside and a decorative coating on the outside. Compared to this traditional production process the use of pre-coated packaging steel leads to a reduction of energy consumption

and CO_2 emission with one third. Moreover, the process water used and the resulting solid wastes are reduced to practically zero [1].

The use of polymer-coated steels entails a number of challenges, since the coating is applied before the actual can forming process. This implies that the coating undergoes the same deformation steps as the ECCS substrate, i.e. deep (re-)drawing (DRD) and wall ironing. Large deformations are induced at high strain rates, pressures and temperatures. During this production process, the coating must fully adhere to the ECCS substrate. Boelen et al. [9] have shown experimentally that damage is introduced at the interface during production and sterilization, see Fig. 3.1(b). After product fabrication, damage is often not visible for the human eye, however it becomes apparent during the prolonged shelf-life of the product. Application for food packaging demands a material that does not exhibit any visible or even measurable corrosion on the inside, even after a relatively long shelf-life period [9, 14].

Several authors studied the influence of deformation on the adhesion between the polymer coating and the steel substrate. Boelen et al. [9] and Van den Bosch et al. [14] performed peel-off experiments and found that the bonding between polymer and steel is reduced by (pre-)deformation of the steel substrate. Laser-induced delamination experiments by Fedorov et al. [28] showed a similar result. Recent results from Faber et al. [25] revealed the presence of interface damage in DRD materials by exploring the interface in cross-sections using Focused Ion Beam milling. These papers suggest that the deformation-induced roughening of the interface is the cause of the loss of adhesion and possible delamination.
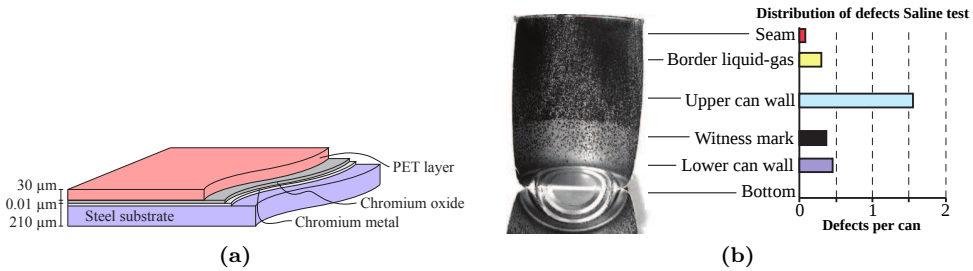

Figure 3.1: (a) Different material layers in a polymer-coated ECC steel (after [15]) and (b) experimentally observed interface damage (after [9]).

3.1.2 Challenges

It is well known that a polycrystalline metal, such as ECCS, roughens at its free surface when deformed, due to crystallographic differences between grains and other plasticity related phenomena. An example of the deformation-induced surface roughening for an ECC steel in tension is shown in Fig. 3.2. The initial height profile (Fig. 3.2(a)) reveals the presence of an initial rolling profile (grooves along the y direction, i.e. in the rolling direction (RD)). Tension was applied along the x direction (transverse direction (TD)). Upon deformation, the initial profile transforms to a new roughness profile during the tensile test (Fig. 3.2(b)). Clearly, this roughening occurs over a wide range of length scales, ranging from the scale of individual dislocations to the size of multiple grains. The resulting profile depends on the deformation conditions and the detailed material prop-
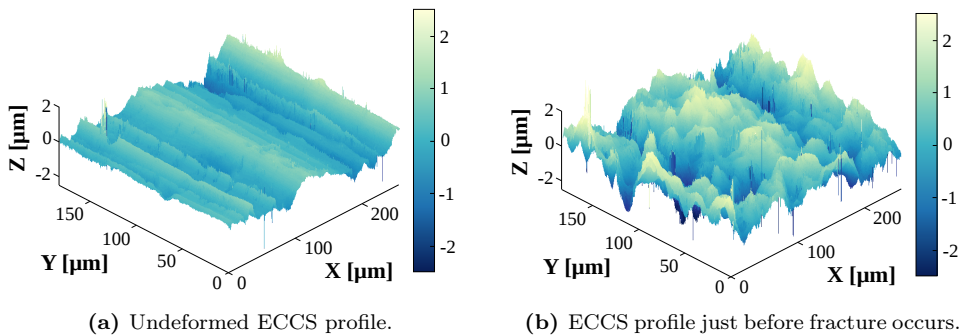
(a) Undeformed ECCS profile.   **(b)** ECCS profile just before fracture occurs.

Figure 3.2: Initial and final surface profile of an ECC steel during a uniaxial tensile test, measured with a confocal optical profiler; X direction is the tensile direction; colors indicate the local surface height in microns.

erties [54]. The roughening phenomenon occurs at the polymer-steel interface during can production, which may result in interface damage. To predict the deformation and potential damage of these polymer-coated steels, an appropriate model has to be developed that incorporates the micro-scale phenomena governing the interface roughening.

In previous research, Van Tijum et al. [66, 67] studied the influence of roughening on the interface properties by numerically generating a roughness profile. While these simulations give valuable insight into the influence of the out-of-plane displacements that can be expected during deformation of a polymer-steel interface, they do not include local in-plane deformations. Furthermore, the numerically generated surface profiles only resemble the average values of experimental measurements. Van den Bosch et al. [14] also studied the effect of a change in interface roughness by including a roughness parameter, based on the Root-Mean-Square (RMS) roughness, in the adopted exponential cohesive zone law. This method reduced the work-of-separation of the cohesive zone elements as a function of the applied pre-deformation, but did not include the actual physical process of roughening. Hence, while these studies provide valuable knowledge on the effect of the change in interface roughness on the interface integrity, they do not incorporate the actual full-field displacement field that accompanies the roughening phenomenon.

In this chapter, a numerical-experimental methodology is developed to study the effect of deformation-induced steel surface roughening on the polymer-steel interface. A methodology to experimentally quantify the three-dimensional displacement field of an evolving surface profile was developed and discussed in chapter 2. A Finite Element based Digital Image Correlation (FE-DIC) methodology was developed to extract the full-field displacements of an evolving surface. The FE-DIC method is applied here to obtain the full-field surface displacements of an ECC steel deformed in tension. The displacement field is applied to a two-dimensional plane strain simulation of a polymer-coated steel. As a result, the steel does not have to be modeled explicitly, since the measured experimental displacements are directly applied to the interface. A sketch of the computational model is shown in Fig. 3.3. The Polyethylene terephthalate (PET) coating is modeled using the parameters for a different PET grade to predict realistic PET behavior. The parameters for the interface are close to the expected real parameters.

The chapter is organized as follows. The experimental methodology to extract the full-field surface deformations is explained in section 3.2. The constitutive and computational

models are discussed in section 3.3. The results of the simulations are given in section 3.4 and discussed in section 3.5.
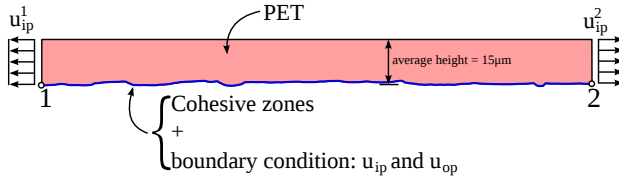

Figure 3.3: Sketch of the computational framework, u_{ip} is the in-plane displacement field and u_{op} the out-of-plane displacement field.

3.2   Steel surface deformation

Quantitative predictions of the interface integrity during deformation-induced steel surface roughening requires either a) a steel constitutive model that accurately predicts the roughening process; or b) the quantified full-field displacement fields that accompany the roughening phenomenon. Since it is very difficult to accurately simulate the roughening process with an advanced constitutive model for the steel, we will here rely on the experimentally quantified displacement field of the steel surface as it evolves. The method is outlined below.

3.2.1   Experimental

Point of departure is the newly developed methodology for characterizing an evolving surface profile, see chapter 2. A Finite Element based Digital Image Correlation (FE-DIC) technique enables extraction of the three-dimensional surface displacements from measured sequential surface height profiles, taken from confocal optical measurements. The methodology is applied here to quantify the surface displacements during roughening of a packaging steel.

The studied polymer-coated steel is TH340, which is a continuously annealed, single reduced, DWI (draw-redraw-wall ironing) quality aluminium-killed low carbon ferritic, electrolytic chromium coated steel (ECCS) sheet. The steel layer is 210 [µm] thick and is lacquered with a protective coating on each side. The coating is a mixture of PET and additives to improve the adhesion to the steel [15]. The thickness of the coating is 15 [µm] on one side of the ECCS and 25 [µm] on the other side.

Tensile samples (20×4 [mm]), with the transverse direction (TD) aligned with the tensile axis, were produced by simultaneously milling stacks of 5 samples to reduce edge effects. Prior to the tensile test, the polymer coating was removed in a two-step process using N-Methyl-2-Pyrrolidone (NMP). The NMP was first heated to 80 [°C] to remove the bulk coating. The coating residuals were removed at 130 [°C]. Removing the coating is essential to improve the accuracy of the confocal height measurement. It can be readily assumed that the absence of the thin compliant coating does not effect the steel roughening process. Tensile testing was performed on a Kammrath&Weiß micro tensile stage with a 500N load cell. The strain rate was set to $5 \cdot 10^{-4}$ [s^{-1}]. *In-situ* measurement of the surface profile was carried out with a Sensofar PLµ2300 confocal optical profiler using a 50x objective. The experimental setup is shown schematically in Fig. 3.4. The image pixel dimensions

were 332 [nm] × 332 [nm]. The height measurement accuracy is approximately 20 [nm]. Because the FE-DIC calculations require the difference between two height profiles to be small, an incremental method was used. A new height profile was measured after each strain increment ($\Delta\varepsilon = 0.25\%$), during which the progressive changes in height were small (see also chapter 2).

The mechanical response of TH340 revealed that the material forms a Lüders band, i.e. plasticity initiates locally on one side of the tensile sample, which extends towards the other side, after which the entire sample deforms plastically. The globally applied engineering strain is then $\varepsilon \approx 5\%$. Note that the local yield strain is much smaller ($\varepsilon_l \approx 0.1\%$). Failure of the material occurs at $\varepsilon \approx 21\%$.

The measured surface height profiles at the start and end of the tensile experiment are shown in Fig. 3.5(left). Three-dimensional profiles are shown in Fig. 3.2. Due to Lüdering, plasticity initiates within the measured region after a relatively large global (engineering) strain of $\varepsilon \approx 3.5\%$. A new roughness pattern is formed on top of the existing initial roughness (see Figs. 3.5(a) and (c)) and it grows upon further deformation, see Fig. 3.5(e). From the measured surface height profiles, the full-field displacement field was extracted using FE-DIC with a linear triangular discretization. The discretization size was based on the optimum of the verification analysis discussed in section 2.3, i.e. approximately 450 pixels per triangular element. The images are analyzed in a sequential manner, i.e. the first and second image are first correlated, followed by the second and third image and so on. The FE-DIC displacements at the start and end of the experiment are shown in Fig. 3.5(right). Comparison of the discretization at the start (Fig 3.5(b)) and end (Fig. 3.5(f)) shows a positive strain in the x (tensile) direction and a negative strain in the y direction. The roughening process is clearly dominated by local deformation mechanisms, as the deformation is inhomogeneous throughout the surface.
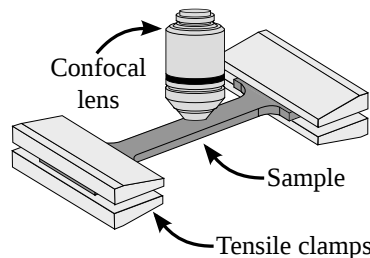
Figure 3.4: Sketch of the experimental test setup.

3.2.2 Surface displacements

Upon closer investigation of the measured displacement fields, small fluctuations between consecutive displacement steps can be identified. These fluctuations are likely due to the adopted incremental calculation procedure, measurement noise and small-scale roughening events that are not captured by the adopted discretization as discussed in section 2.4.3. The experimentally acquired displacement fields therefore still require filtering, since these fluctuations may cause non physical behavior if used directly in numerical simulations.

Singular Value Decomposition (SVD) is an effective tool to filter out spurious fluctuations while preserving the essential kinematics [31]. Here, SVD was applied to the in-plane displacement fields (u_x and u_y) and the out-of-plane displacement field (u_z). The singular

(a) profile, $\varepsilon = 0\%$.

(b) FE-DIC, $\varepsilon = 0\%$.

(c) profile, $\varepsilon = 3.5\%$.

(d) FE-DIC, $\varepsilon = 3.5\%$.

(e) profile, $\varepsilon = 20.75\%$.

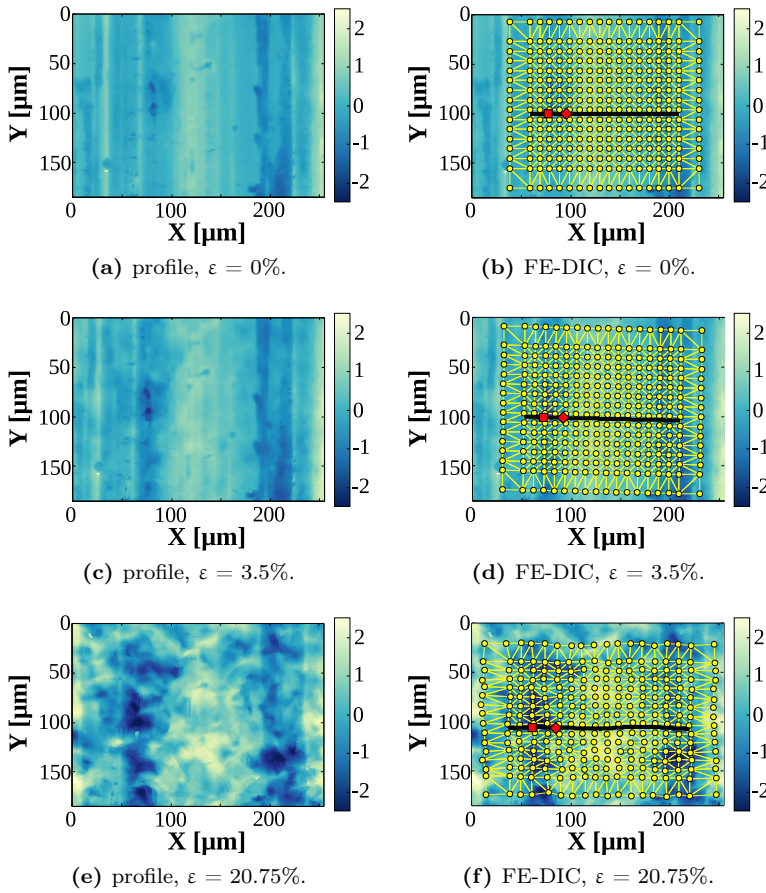**(f)** FE-DIC, $\varepsilon = 20.75\%$.

Figure 3.5: (left) Surface height profiles measured at different strains; (right) the corresponding correlated FE-DIC displacements; the black line is a central deforming line initially parallel to x; all values are in microns, the tensile (x) direction is horizontal and the colors indicate the local surface height; red square and diamond on the black line are used in Fig. 3.6.

values are truncated when the singular values are less than 1% of the largest singular value. The reconstructed displacement fields sufficiently captured the roughening kinematics while eliminating nonphysical fluctuations at the scale of interest. The unfiltered and filtered displacements in two points are shown in Fig. 3.6. The fluctuations are especially visible in the out-of-plane displacements (Fig. 3.6(b)) as the amplitude of the out-of-plane displacements is considerably smaller than the in-plane displacements.

In the two-dimensional plane strain computational model, two scalar displacement fields are prescribed to the polymer-steel interface, i.e. a parallel in-plane displacement and an out-of-plane displacement along a line profile on the initial surface, here a line parallel to the tensile direction. While this line is initially aligned with the tensile direction, it may not stay aligned, due to the three-dimensional nature of the roughening process, e.g. see the line shown in Figs. 3.5(right). Therefore, the scalar in-plane displacement parallel
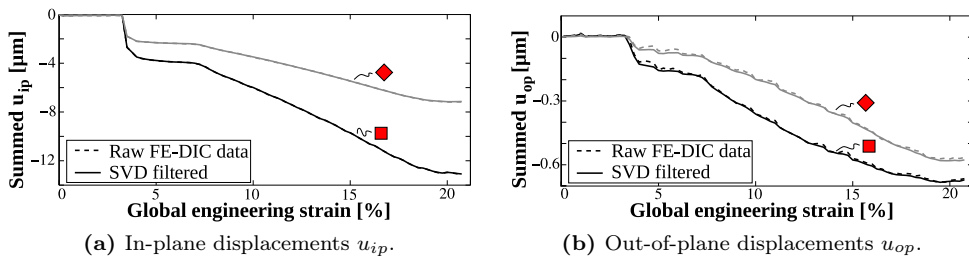
(a) In-plane displacements u_{ip}.   **(b)** Out-of-plane displacements u_{op}.

Figure 3.6: Displacements of two points (see red square and diamond in Fig. 3.5); raw FE-DIC displacements are the dashed lines; displacements after SVD are the solid lines; note that the difference between the unfiltered and filtered in-plane displacements in (a) is negligible.

to the line (u_{ip}) is extracted from the u_x and u_y displacement fields by determining the length change of each line segment, i.e.

$$u_{ip,i} = l_i - L_i, \quad i = 1 \ldots n, \tag{3.1}$$

where n is the number of line segments and L_i and l_i are the previous and new segment length, respectively, and can be determined via the line position and the calculated displacement fields. This is schematically shown in Fig. 3.7

The out-of-plane displacement field does not require a projection and is equal to u_z. After applying SVD and determining the in-plane displacement field, the evolution of the black line in Fig. 3.5(right) can be calculated. The evolving surface profile is shown in Fig. 3.8. The evolution clearly shows that the steel surface is elongated in-plane. Furthermore, since plasticity initiates locally at an increased strain rate due to Lüdering, a jump in the surface height profile is calculated (see Fig. 3.8). Finally, the initiation and growth of hills and valleys along the line profile is also visible. It is this evolving surface profile that will be prescribed to the two-dimensional polymer-steel interface model to study the mechanical response of the polymer coating and interface.
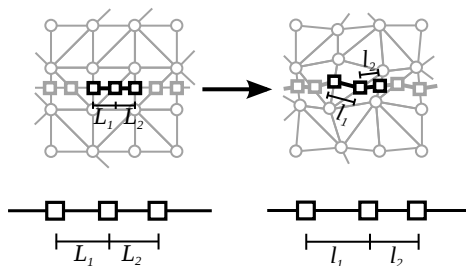

Figure 3.7: Sketch of the projection method; (top) two-dimensional evolution of the line profile; (bottom) evolution of the projected line.
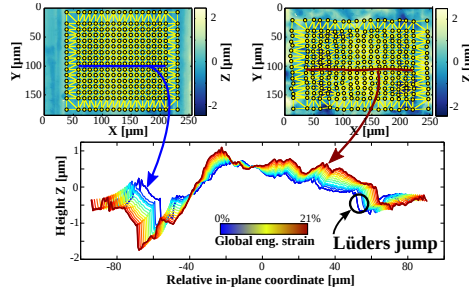
Figure 3.8: Evolution of the line profile initially located at $y = 100$ [µm].

3.3 Constitutive and computational model

In this section, the material models for the polymer and interface are presented, along with their numerical implementation.

3.3.1 Polymer model

To accurately predict the mechanical response of the PET, the Eindhoven Glassy Polymer (EGP) model is used. Previous research has shown that the EGP model adequately captures the mechanical behavior of amorphous polymers [17, 41]. The typical mechanical behavior of amorphous glassy polymers is shown in Fig. 3.9(a). During a compression test, the polymer first behaves nearly linear elastic, followed by non-linear visco-elastic behavior. When the yield point is reached, depending on the polymer age, a softening regime sets in. The softening is overtaken by strain hardening at higher strains. The yield point depends on the applied strain rate. Note that PET is not fully amorphous, but rather semi-crystalline. However, the crystallinity of the used PET coating is small, about 8%. The EGP model is a multi-mode, multi-process polymer constitutive model [17]. In the present work only one mode and one process is considered, giving a single-mode, single-process approximation (SM-SP). The mechanical analogue of the SM-SP EGP model is shown in Fig. 3.9(b). The essential equations of the SM-SP EGP model are detailed below.

The EGP model splits the total stress in two contributions, i.e. the driving stress $\boldsymbol{\sigma}_s$ and the hardening stress $\boldsymbol{\sigma}_r$ (see also Fig. 3.9(b)),

$$\boldsymbol{\sigma} = \boldsymbol{\sigma}_s + \boldsymbol{\sigma}_r. \tag{3.2}$$

The hardening stress contains the rubber elastic contribution of the oriented entangled network and is described by a neo-Hookean relation,

$$\boldsymbol{\sigma}_r = G_r \tilde{\mathbf{B}}^d, \tag{3.3}$$

where G_r is the strain hardening modulus and $\tilde{\mathbf{B}}^d$ the deviatoric part of the isochoric left Cauchy-Green deformation (Finger) tensor. The driving stress incorporates the intermolecular interactions and is decomposed in a hydrostatic ($\boldsymbol{\sigma}_s^h$) and a deviatoric stress ($\boldsymbol{\sigma}_s^d$), i.e.

$$\boldsymbol{\sigma}_s = \boldsymbol{\sigma}_s^h + \boldsymbol{\sigma}_s^d = \kappa(J-1)\mathbf{I} + G\tilde{\mathbf{B}}_e^d, \tag{3.4}$$

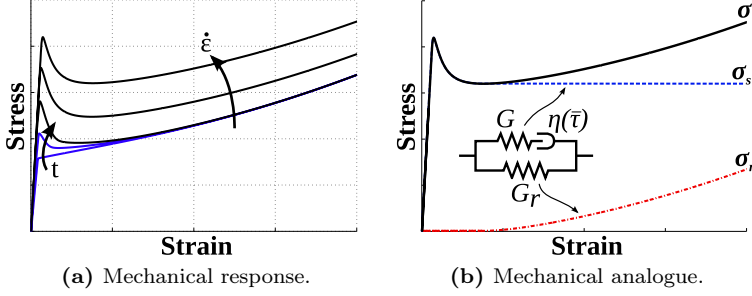(a) Mechanical response.   (b) Mechanical analogue.

Figure 3.9: Typical mechanical behavior of amorphous polymers and the mechanical analogue of the SM-SP EGP model (after [17]).

where κ is the bulk modulus, J is the volume change ratio, $\mathbf{I}$ is the unity tensor, G is the shear modulus and $\tilde{\mathbf{B}}_e^d$ the deviatoric part of the elastic isochoric Finger tensor. The evolution of J and $\tilde{\mathbf{B}}_e^d$ is calculated from

$$\dot{J} = J\mathrm{tr}(\mathbf{D}), \tag{3.5}$$

$$\dot{\tilde{\mathbf{B}}}_e = (\tilde{\mathbf{L}} - \mathbf{D}_p) \cdot \tilde{\mathbf{B}}_e + \tilde{\mathbf{B}}_e \cdot (\tilde{\mathbf{L}}^{\mathrm{T}} - \mathbf{D}_p). \tag{3.6}$$

Here $\mathbf{L}$ is the velocity gradient tensor and $\mathbf{D}$ the deformation rate tensor. The plastic deformation rate tensor, $\mathbf{D}_p$ is related to $\boldsymbol{\sigma}_s^d$ via a non-Newtonian flow rule,

$$\mathbf{D}_p = \frac{\boldsymbol{\sigma}_s^d}{2\eta}, \tag{3.7}$$

with the viscosity

$$\eta = \eta_{0,ref} \frac{\bar{\tau}/\tau_0}{\sinh(\bar{\tau}/\tau_0)} \exp\left(\frac{\mu p}{\tau_0}\right) \exp(S), \tag{3.8}$$

where $\eta_{0,ref}$ is the zero-viscosity defined according to the reference state, τ_0 is the characteristic equivalent stress and μ is a pressure dependency parameter. The total equivalent stress, $\bar{\tau}$ and the pressure, p, are defined as

$$\bar{\tau} = \sqrt{\tfrac{1}{2}\boldsymbol{\sigma}_s^d : \boldsymbol{\sigma}_s^d}, \tag{3.9}$$

$$p = -\tfrac{1}{3}\mathrm{tr}(\boldsymbol{\sigma}). \tag{3.10}$$

The state parameter S incorporates the thermodynamic history dependency and is related to the equivalent plastic strain, $\bar{\varepsilon}_p$, i.e.

$$S(\bar{\varepsilon}_p) = S_a \cdot R(\bar{\varepsilon}_p). \tag{3.11}$$

Here S_a captures the initial state of the polymer. R ranges between 0 (rejuvenated) and 1 (fully aged). In the current implementation the time dependence of S_a, i.e. physical aging, is not included. Therefore, the yield stress does not increase with time and only the effect of mechanical rejuvenation can be predicted with the current model.

The equivalent plastic strain rate is defined as

$$\dot{\bar{\varepsilon}}_p = \frac{\bar{\tau}}{\eta}. \tag{3.12}$$

The softening function, $R(\bar{\varepsilon}_p)$, describes the influence of the strain on the polymer age. Following Klompen et al. [41], the softening function is described by a modified Carreau-Yasuda function,

$$R(\bar{\varepsilon}_p) = \frac{\left(1 + (r_0 \cdot \exp{(\bar{\varepsilon}_p)})^{r_1}\right)^{(r_2-1)/r_1}}{(1 + r_0^{r_1})^{(r_2-1)/r_1}}, \tag{3.13}$$

where r_0, r_1, r_2 are fitting parameters.

The material parameters for the PET coating used in this work are listed in Table 3.1. The parameters were determined by Poluektov et al. [52] for an amorphous PET grade. These parameters may not be fully exact for polymer-coated steels, e.g. TH340, but they do predict realistic PET behavior. The corresponding mechanical response during a uniaxial tensile test for an aged ($S_a = 13.3$ [-]) and rejuvenated ($S_a = 0$ [-]) PET layer is shown in Fig. 3.10.

Table 3.1: Material properties of PET for the EGP model.

G_r [MPa]	κ [MPa]	G [MPa]	$\eta_{0,ref}$ [MPa·s]	τ_0 [MPa]
4.7	1800	812	$3 \cdot 10^8$	1.262

μ [-]	S_a [-]	r_0 [-]	r_1 [-]	r_2 [-]
$4.8 \cdot 10^{-2}$	13.3	0.98	20	-3.5
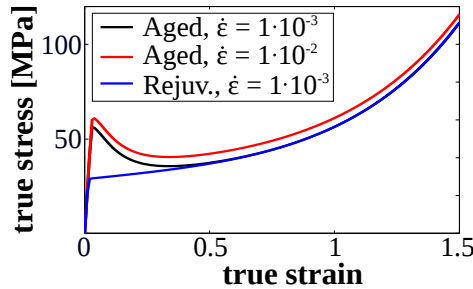
Figure 3.10: Mechanical response at different strain rates and PET ages (S_a) during a uniaxial tensile test for the EGP parameters of PET shown in Table 3.1.

3.3.2   Interface model

The interface between the PET and ECCS is modeled using Cohesive Zone elements. The modified Xu and Needleman exponential traction-separation law developed by Van den Bosch et al. [12] is used to describe the adhesion between the PET and steel. The law for

normal (n) and tangential (t) traction is defined as

$$T_n\left(\Delta_n, \Delta_t\right) = \frac{\phi_n \Delta_n}{\delta_n^2} \exp\left(-\frac{\Delta_n}{\delta_n}\right) \exp\left(-\frac{\Delta_t^2}{\delta_t^2}\right), \tag{3.14}$$

$$T_t\left(\Delta_n, \Delta_t\right) = 2\frac{\phi_t \Delta_t}{\delta_t^2}\left(1 + \frac{\Delta_n}{\delta_n}\right) \exp\left(-\frac{\Delta_n}{\delta_n}\right) \exp\left(-\frac{\Delta_t^2}{\delta_t^2}\right), \tag{3.15}$$

where Δ is the cohesive zone opening, ϕ is the work of separation and δ is the characteristic opening length. This is a coupled interfacial law, as the traction depends on both opening directions. As shown by Van den Bosch et al. [12], the coupling ensures a realistic work of separation during multi-directional opening, see also Fig. 3.11. The maximum reached traction in one direction decreases with prior opening in the other direction.
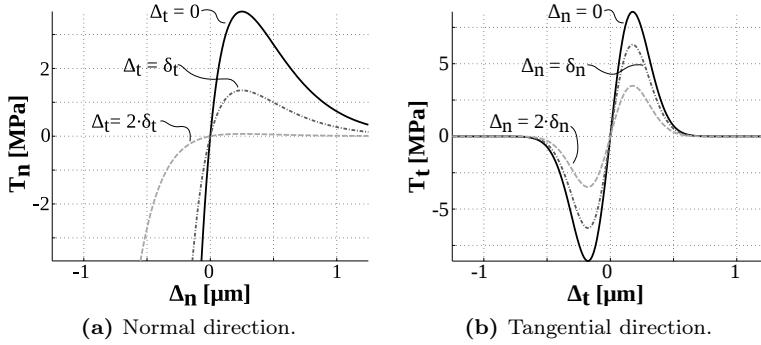

(a) Normal direction.   **(b)** Tangential direction.

Figure 3.11: The coupled exponential traction-separation law of Van den Bosch et al. [12], using the parameters of Table 3.2.

Because strain reversal may occur during roughening, an unloading behavior must be included in the cohesive zone model. Van den Bosch et al. [13] introduced two types of unloading, elasticity-based damage and elasto-plastic unloading. Here, elastic damage unloading is assumed, see also Fig. 3.12(c), i.e. during unloading of the cohesive zone (points 2 to 3) the traction decreases linearly back to zero, i.e. with a degraded stiffness. The interface damage is quantified by an integrity parameter. The total energy ($\Phi = \Phi_t + \Phi_n$) stored in the cohesive zone during opening is calculated stepwise between each deformation increment, i.e.

$$\Phi_n^{i+1} = \Phi_n^i + \delta\Phi_n = \Phi_n^i + \int_{\Delta_n^i}^{\Delta_n^{i+1}} T_n|_{\Delta_t = \Delta_t^{i+1}} d\Delta_n, \tag{3.16}$$

$$\Phi_t^{i+1} = \Phi_t^i + \delta\Phi_t = \Phi_t^i + \int_{\Delta_t^i}^{\Delta_t^{i+1}} T_t|_{\Delta_n = \Delta_n^{i+1}} d\Delta_t, \tag{3.17}$$

where i is the increment number and $\Delta_j^{i+1} = \Delta_j^i + \delta\Delta_j$, $j = n, t$. Note that the current opening in the other direction (e.g. Δ_t^{i+1} for Φ_n^{i+1}) is used. This definition requires that the incremental change of the cohesive opening is small. Not all energy is dissipated in the cohesive zone. The stored energy which is returned during unloading is

$$\Psi_i = \frac{1}{2}T_j(\Delta_{j,max})\Delta_{j,max}, \quad j = n, t \tag{3.18}$$

Here, elastic damage unloading is assumed and $\Delta_{j,max}$ is the (absolute) maximum opening reached in the loading history. The total dissipated energy is then

$$\Omega = \sum_{i=n,t} \Phi_i - \Psi_i \qquad (3.19)$$

The integrity is then defined as the fraction of energy that can still be dissipated, i.e.

$$\xi = 1 - \frac{\Omega}{\phi}, \quad \xi \in [0,1], \qquad (3.20)$$

where it is assumed that $\phi_n = \phi_t = \phi$. An example of the evolution of the interface integrity during multi-directional opening using the parameters in Table 3.2 is given in Fig. 3.12. First, a cohesive zone element is opened and partly closed in normal direction. Hereafter, the element is opened in tangential direction until the traction is almost zero. Fig. 3.12(d) shows that the integrity never increases and drops to zero when the tangential traction becomes negligible, indicating complete interface failure.
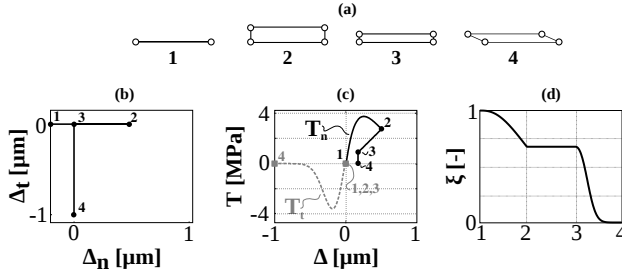

Figure 3.12: Evolution of the interface integrity during multi-directional opening; (a) cohesive zone element at the different steps of opening; (b) prescribed cohesive zone opening; (c) resulting normal and tangential tractions, including unloading (2-3); (d) evolution of the interface integrity parameter ξ; the used cohesive zone parameters are listed in Table 3.2.

The constants for the interface model have to be determined via dedicated experiments. It is known from literature that different values for the work of separation ϕ may result for different experiments at different scales, see e.g. Fedorov et al. [28] versus Van den Bosch et al. [15]. These differences result from the dissipated energy adjacent to the interface (in the process zone), which is typically lumped in ϕ of the cohesive zone. In the present work, small-scale interfacial phenomena are of interest, and values for ϕ have to be characteristic for de-adhesion only. The adhesion energy determined by Fedorov et al. [28] is used here. The interface parameters are listed in Table 3.2. Note that here $\phi_n = \phi_t = \phi$ and $\delta_n = \delta_t = \delta$.

Table 3.2: Cohesive zone parameters used in the simulations.

ϕ_n [J·m^{-2}]	ϕ_t [J·m^{-2}]	δ_n [µm]	δ_t [µm]
2.5	2.5	0.25	0.25

3.3.3   Geometry and boundary conditions

To model the mechanical response of the polymer and polymer-steel interface as a result of deformation-induced roughening of the steel substrate, it is assumed that the steel dictates the bottom interfacial deformation. The steel is therefore not modeled explicitly. As discussed in the introduction, a two-dimensional plane strain computational model is used, see also Fig. 3.3. While the full three-dimensional displacement field is available for the numerical simulation, it is computationally expensive to simulate a 3D situation. It is therefore assumed that the displacements perpendicular to the modeled line profile are small, see also Fig. 3.8.

For the 2D plane strain state considered, the out-of-plane (u_{op}) and in-plane (u_{ip}) displacements are prescribed to the interface elements, see also Fig. 3.8. The simulated time frame is identical to the experimental one. To simulate more realistic strain rates, the loading time can be reduced. However, the surface roughening mechanisms may also change when the strain rate is increased.

The geometry of the computational model is shown in Fig. 3.3. In this model, the bottom of the interface has the topology of the initial surface profile obtained from the undeformed height profile. This initial surface profile is complex and therefore a mix of quadrilateral 4-node and triangular 3-node elements is used for the polymer layer. The left and right boundaries are kept straight during the simulation. A mesh convergence study was performed to determine the optimal element size. The cohesive elements have an initial size of 100 [nm].

3.4   Results

3.4.1   Polymer response

The equivalent Von Mises stress and equivalent plastic strain in the PET coating at a global engineering strain of $\varepsilon = 10\%$ and $\varepsilon = 20.75\%$ are shown in Figs. 3.13 and 3.14, respectively. The displacements of the line initially located on $y = 100$ [µm] (see also Figs. 3.5 and 3.8) are prescribed to the interface elements.

The results reveal the localized stress and strain bands in the PET coating due to the local variations of the steel surface displacements. Interface damage is clearly visible near the regions of high stress/strain in the PET coating, see arrows in Fig. 3.13. The local nature of the roughening phenomenon results in localization bands with high stresses at the interface. Damage typically initiates at or near these high stress locations. Localization is triggered by the softening branch in the polymer behavior (see also Fig. 3.9) [48]. This local necking of the PET coating leads to an accumulation of strains in this region with interface damage as a result. This necked region is initially small, but grows as the deformation is increased due to strain hardening of the PET coating. This growth is accompanied by further opening of the interface. At $\varepsilon = 20.75\%$, the interface is almost fully delaminated, see Fig. 3.14. The high stresses in the delaminated PET coating near the left boundary are a result of the applied boundary condition.

Next, a rejuvenated PET coating was studied, i.e. $S_a = 0$ [-]. By rejuvenating the polymer coating, the softening branch in the mechanical behavior vanishes (see also Fig. 3.10). The stress and strain within the rejuvenated polymer at $\varepsilon = 20.75\%$ are shown in Fig. 3.15. Note that the colors represent the same levels of stress and strain as in Figs. 3.13 and 3.14. It is clear that the stresses within the PET coating are now smaller and less localized. Only small stress and strain bands appear and no necking is yet seen. Furthermore, no
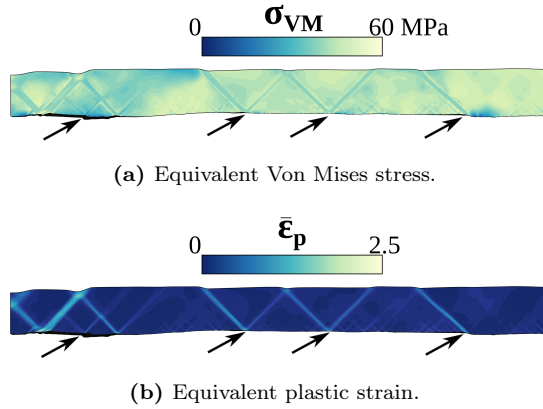
(a) Equivalent Von Mises stress.

(b) Equivalent plastic strain.

Figure 3.13: Predicted equivalent Von Mises stress and equivalent plastic strain in the polymer coating along the line initially located at $y = 100$ [µm] at a globally applied tensile strain of $\varepsilon = 10\%$; the failed interface elements are colored black; visible interface damage is indicated by the arrows.

(a) Equivalent Von Mises stress.
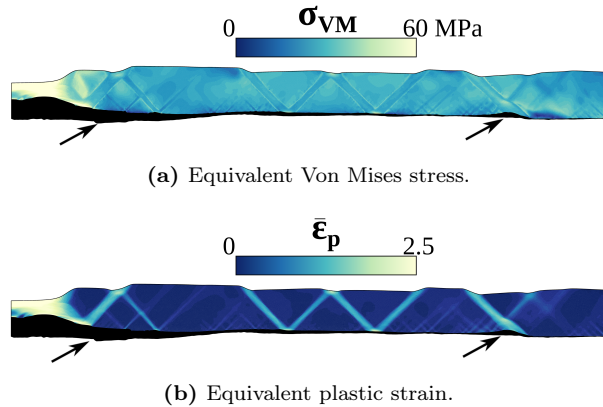

(b) Equivalent plastic strain.

Figure 3.14: Predicted equivalent Von Mises stress and equivalent plastic strain in the polymer coating along the line initially located at $y = 100$ [µm] at a globally applied tensile strain of $\varepsilon = 20.75\%$; the failed interface elements are colored black; visible interface damage is indicated by the arrows.

large interface damage is visible. Some minor interface damage can be identified (see arrow in Fig. 3.15) due to high stresses and strains at the interface as a result of the initial surface profile and the applied displacement field.

Clearly, the polymer age influences the scale of the predicted damage events due to the softening branch that is formed at increased polymer ages. Furthermore, the formation, stabilization and growth of the localization band results in delamination of the coating. Growth of this band further damages the interface. Thus, the rate at which the interface damage grows depends strongly on the polymer age.
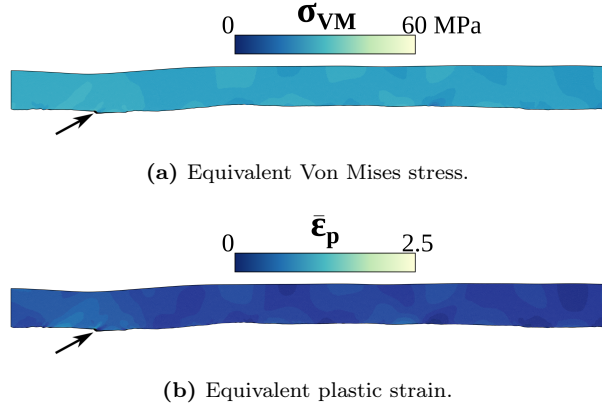
(a) Equivalent Von Mises stress.

(b) Equivalent plastic strain.

Figure 3.15: Predicted equivalent Von Mises stress and equivalent plastic strain in the rejuvenated polymer coating along the line initially located at $y = 100$ [µm] at a globally applied tensile strain of $\varepsilon = 20.75\%$; the failed interface elements are colored black; visible interface damage is indicated by the arrows.

3.4.2   Interface integrity

Figs. 3.13-3.15 allow for a qualitative comparison of damage only since small-scale damage events are not resolved in the discretization used. To clarify the interface damage in these simulations, the interface integrity ξ is studied. The interface integrity at $\varepsilon = 10\%$ and $\varepsilon = 20.75\%$ is shown in Fig. 3.16 for both the rejuvenated and aged PET coating. Both profiles show that the interface integrity decreases locally during deformation, but the reduction for aged PET is more severe. More locations along the line profile show a large reduction in interface integrity at a low strain and the integrity becomes zero for most of the interface at large strains. The rejuvenated PET also reveals a local reduction in interface integrity, but the damage is clearly less severe, indicating that damage is delayed due to the absence of strain softening in the PET.

3.4.3   Parameter sensitivity

The polymer age greatly influences the predicted interface damage. To further study this influence, the polymer age parameter S_a is varied between 0 and 17.5 to study the effect on the predicted interface damage along the line initially located at $y = 100$ [µm]. The average interface integrity ξ_{av} as a function of the global engineering strain and the polymer age is shown in Fig. 3.17. The average interface integrity is calculated by averaging the interface integrity of all interface elements at each increment. The difference in interface integrity for low values of S_a is initially small. For $S_a < 5$ [-] the average integrity decreases slightly with S_a. However, for $S_a > 5$ [-], the integrity rapidly decreases with S_a and the applied engineering strain. The localization band that forms for aged PET drastically increases the size of the delaminated area (see also Fig. 3.16), thereby lowering the average interface integrity. It can be seen that the simulations were unable to converge in cases where the interface integrity drops rapidly towards zero.

The average interface integrity provides valuable insight into the global influence of polymer aging. However, this parameter does not indicate when the interface integrity locally drops below a certain value. Descending below a threshold value for the interface integrity
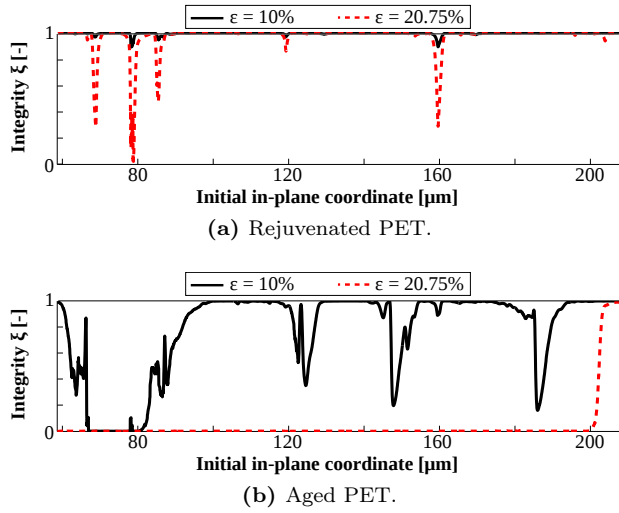
(a) Rejuvenated PET.

(b) Aged PET.

Figure 3.16: Interface integrity profile at $\varepsilon = 10\%$ and $\varepsilon = 20.75\%$ for the rejuvenated and aged PET over the line initially located at $y = 100$ [µm].
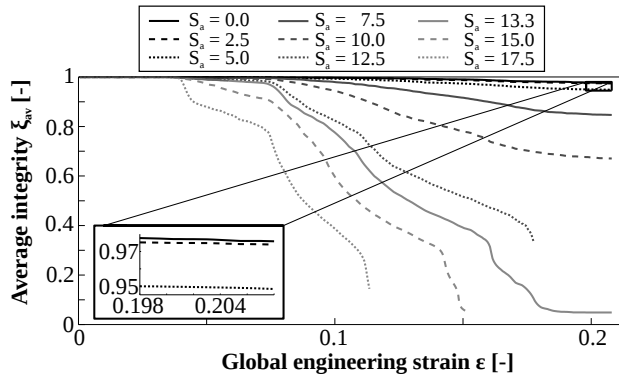

Figure 3.17: Average interface integrity as a function of the globally applied strain and the polymer age for the line initially located at $y = 100$ [µm].

is an indication of local interface failure. To study this parameter, 11 different line profiles were simulated and the average global engineering strain was calculated at the moment when the integrity drops below 10%. This critical strain ε_c is an indication for local crack nucleation at the interface. Again, the polymer age parameter is varied to study the effect of aging.

The result of this analysis is shown in Fig. 3.18. Note that the average values were obtained using only those line profiles that actually reveal a drop below the critical value of the interface integrity. Two trends can be noticed: (1) the critical strain slightly increases to a maximum around $S_a = 2.5$ [-] (this point changes between individual line profiles); (2) beyond this value, the critical strain decreases as S_a increases. The initiation of interface damage is dependent on two phenomena, i.e. a) the prescribed roughness evolution and b) localization due to strain softening. For rejuvenated PET, the localization is determined by the initial surface profile and its evolution. For relatively young PET coatings, mild

localization occurs and the localization tends to spread more before the critical integrity is reached in the localization band, delaying the initiation of interface damage compared to rejuvenated PET. This explains the upward trend in Fig. 3.18. However, when the polymer age is increased further the interface at the localization band is already damaged before the band spreads, due to the high stresses within the localized region. Further increase of the polymer age results in a decrease of the critical strain. The explanation of this trend is found in the competition between strain softening and hardening [48]. Strain hardening stabilizes the localization phenomenon, but this effect is decreased since an increased polymer age also entails an increased yield stress. The stabilizing effect of strain hardening is illustrated in Fig. 3.19. Note that only a single line profile is shown, i.e. the line initially located at $y = 88$ [µm] (the line located at $y = 100$ [µm] did not show a drop below 10% integrity for low values of S_a). The hardening modulus G_r was increased to study the effect of the strain hardening branch. The optimum value for the polymer age shifts with the hardening modulus. Increasing the hardening modulus increases the optimal S_a value and vice versa, indicating that the presence of strain hardening delays the localization instability to higher values of S_a.
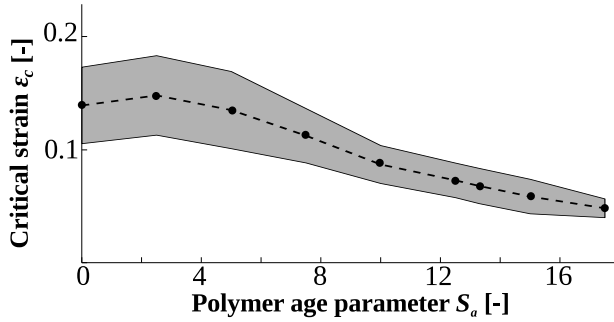
Figure 3.18: Influence of the polymer age parameter on the critical strain ε_c when the integrity locally drops below 10%; bands indicate the standard deviation between the different line profiles passing this threshold.

Figure 3.19: (a) Mechanical response of PET for two values of the strain hardening modulus G_r; (b) corresponding predicted critical strain at which the local integrity first drops below 10% for the line profile initially located at $y = 88$ [µm].

3.5   Discussion

The simulations predict the initiation and growth of interface damage as a result of the prescribed evolution of the steel surface profile.

The presence of interface damage in these materials was experimentally verified by Faber et al. [25]. They explored cross-sections of the deformed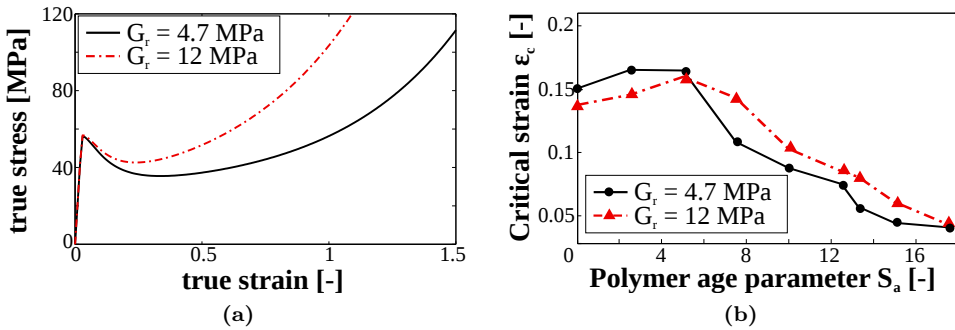 polymer-steel interface in DRD cans. An example of the experimentally identified interface damage is shown in Fig. 3.20. The experiments revealed that the polymer coating locally delaminates during can production. The damage events are small and typically occur near highly deformed regions of the steel surface, indicating that deformation-induced steel surface roughening plays an important role in the initiation of interface damage. These experiments verify the presence of damage, however they do not reveal the evolution of the interface roughness or the damage initiation and hence only allow for a qualitative comparison with the simulations. To the best of our knowledge, the in-situ observations required for quantitative comparison are not available and challenging to obtain at a micron scale or smaller.
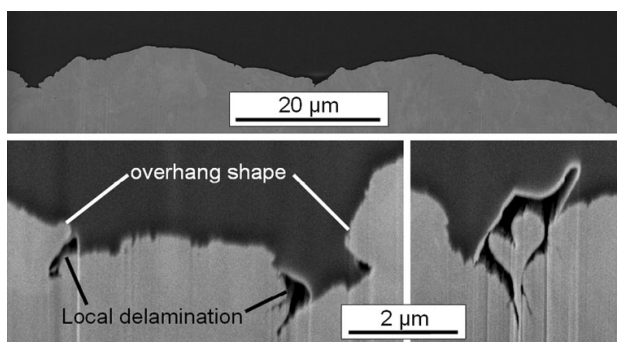

Figure 3.20: Experimental results of the deformed polymer-steel interface after can production for a pre-coated packaging steel; results obtained via Focused Ion Beam milling (reproduced from [25]; with kind permission from Springer Science+Business Media B.V.).

Finally, quantitative prediction of the interface integrity during forming operations requires properly identified parameters for the particular PET grade used. The mechanical response of a thin PET coating with additives to promote adhesion has been studied by Van den Bosch et al. [15]. They performed tensile experiments on a PET coating after the steel substrate was chemically removed. These experiments may be used to identify the model parameters. Furthermore, a truly quantitative study of the interface damage may require the full three-dimensional displacement field, which has to be coupled to a three-dimensional computational model.

3.6   Conclusion

A numerical-experimental methodology has been presented, using a Global Digital Image Correlation technique combined with a computational model of a polymer and interface layer. The presented method allows for a detailed study of the mechanical behavior of a polymer-steel interface during deformation-induced steel surface roughening. The method incorporates the experimentally obtained displacement field into a numerical framework

to predict the initiation and growth of interface damage and hence outperforms the use of average surface roughness characteristics.

The numerical predictions show that the change in surface height profile of the steel and the displacements that accompany this process can cause the polymer-steel interface to locally delaminate. Polymer aging increases the damage and triggers an initial increase, followed by a decrease of the critical strain at which the interface integrity locally drops below a certain value. An optimum for the polymer age is found, where the competition between strain hardening and softening delays interface failure. These results provide valuable insight into the required processing and storage conditions in industrial applications, where these polymer-coated steels are used, e.g. for food and beverage cans. These applications demand that no interface damage is present, even after prolonged shelf-life.

PREVENTING INTERFACE DAMAGE BY PRE-CONDITIONING POLYMER-COATED STEELS VIA ROLLING

Abstract
A novel methodology is presented for pre-conditioning a polymer-coated steel used in food and beverage packaging. Mechanical rejuvenation of the coating via rolling is studied in order to prevent interface damage in subsequent forming operations. The simulations reveal that the thermodynamic state of the polymer coating after rolling depends on the rolling reduction. This dependency can be used to tailor the thermodynamic state of the coating prior to can production. A proof-of-principle simulation was performed to study the effects of rejuvenation on subsequent deformation processes. Deformation-induced interface roughening was studied for the initial and rejuvenated polymer coating. The predictions for a rejuvenated polymer coating indicate a significant decrease in interface damage.
The presented numerical framework allows for a detailed study of the effects of pre-conditioning on the interface integrity during subsequent forming operations. With properly identified material parameters, it becomes possible to tailor the polymer-steel material properties before and during production to minimize interface damage during production and storage of cans or canisters, e.g. for food and beverage packaging.

4.1 Introduction

Recent years show an increase in the use of metal-polymer laminates in the form of electrolytic chromium coated steel (ECCS) sheets coated with a polymer layer (see Fig. 4.1) for packaging of food and beverages. Producing cans and canisters using pre-coated steel leads to a significant reduction of the environmental impact of the production process compared to conventional production methods. Traditionally, a can is first made from blank steel sheet after which several lacquering steps are necessary to apply a protective coating on the inside and a decorative coating on the outside. The reduction in environmental impact results from a reduction in energy consumption and CO_2 emission with one third and a reduction in process water and resulting solid wastes to practically zero [1]. However, the pre-coated steel is subjected to several forming stages during production, i.e. deep (re-)drawing (DRD) and wall ironing (see Fig. 4.2). These processes induce
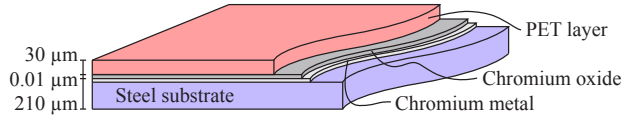
30 μm
0.01 μm
210 μm

PET layer
Chromium oxide
Chromium metal
Steel substrate

Figure 4.1: Different material layers in a polymer-coated ECC steel (after [15]).

large deformations at high strain rates, pressures and temperatures. It has been shown experimentally that the interface accumulates damage during production and sterilization. While this damage is often not visible after production, it may become apparent during the prolonged product shelf-life. The food packaging industry demands that the polymer coating fully adheres to the ECCS substrate, even after a relatively long shelf-life, since this triggers corrosion and compromises the quality of the canned content [9, 14].
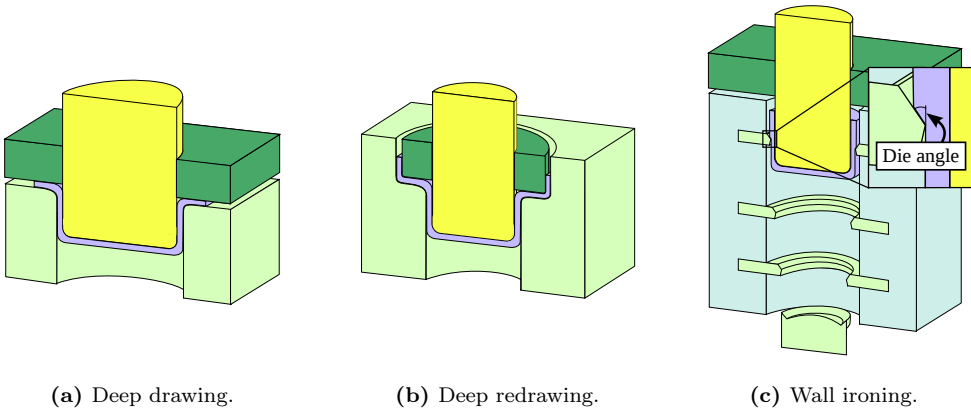

Die angle

(a) Deep drawing.   **(b)** Deep redrawing.   **(c)** Wall ironing.

Figure 4.2: Different production methods used to produce a can or canister (after `CustomPartNet.com`).

An example of the typical intrinsic response of glassy polymers under uniaxial compression is shown in Fig. 4.3. First, the polymer shows a nearly linear elastic response (1) after which the response becomes non-linear visco-elastic (2). After the yield point (3) is reached, depending on the thermodynamic state of the polymer (i.e. its age), softening is observed (4), which is overtaken by strain hardening at high strains (5). A key characteristic of polymer glasses is the fact that the yield point depends on the strain rate applied [17].

The yield point thus depends on the thermodynamic state. The thermodynamic state refers to the (non-)equilibrium state of a glassy polymer, i.e. whether the polymer is close to or far away from its equilibrium state. When a polymer is cooled below its glass transition temperature (T_g), the mobility of the chains is decreased and the polymer moves away from equilibrium. However, the chain mobility is not zero and equilibrium will only be reached after an extended time, i.e. physical aging. The amount of softening seen in the mechanical response increases with physical aging. The process of moving the thermodynamic state of the polymer away from equilibrium, i.e. reverse aging, is called rejuvenation. Rejuvenation can be accomplished through a thermo-mechanical treatment [42, 48].
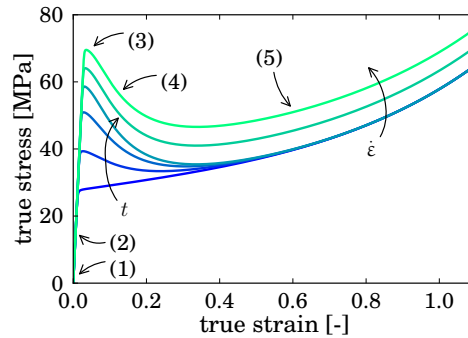
Figure 4.3: Typical mechanical behavior of amorphous polymers; numbers indicate typical trends; (1) linear elastic; (2) non-linear visco-elastic; (3) yield point; (4) strain softening; and (5) strain hardening.

The results presented in chapter 3 revealed the importance of the thermodynamic state of the polymer coating prior to deformation on the predicted interface damage. A numerical-experimental study of the effect of deformation-induced interface roughening on the interface integrity of a polymer-coated steel indicated the existence of an optimum in the initial thermodynamic state of the PET (Polyethylene terephthalate) coating, i.e. the polymer age prior to deformation. A rejuvenated polymer shows (almost) no softening during mechanical deformation, while an aged polymer typically softens, see also Fig. 4.3. The simulations, which were performed using experimentally obtained full-field displacement fields of an evolving steel surface profile, predicted noticeably less interface damage for a rejuvenated coating compared to an aged coating. The changes in steel surface roughness trigger localization in the aged polymer coating, resulting in interface delamination. This localization behavior is significantly reduced for a rejuvenated coating, resulting in less damage.

After coating the steel substrate, the material is typically stored for extended periods of time. During this time, the coating ages continuously. Hence, rejuvenating the polymer coating towards the optimal initial thermodynamic state prior to production may decrease or even prevent the formation of interface damage.

It is well known that the thermodynamic state of a polymer can be tailored through a thermo-mechanical treatment [48]. Thermal rejuvenation is accomplished by heating the polymer to a temperature above the glass transition temperature and then reducing the chain mobility via quenching. However, while a thermal treatment is relatively straight-forward to apply in an industrial forming process, in the case of a polymer-coated steel it may lead to interface failure due to a mismatch in thermal expansion between the PET coating and steel substrate. Furthermore, the increased temperature required for rejuvenation may result in additional crystallization of the coating.

Another possibility is a mechanical rejuvenation procedure, e.g. rolling or ironing. The deformation imposed on the polymer-coated steel during such a procedure will induce stresses at the interface, i.e. normal and shear stresses, which may result in interface failure. However, a study by Van der Aa et al. [1] showed that during wall ironing of a polymer-coated steel the coating hardens due to the high pressure imposed on it. This hardening reduces the stress difference between the typically compliant polymer coating and the stiff steel substrate, since the post-yield response of the polymer depends on

the hydrostatic pressure [22]. However, wall ironing induces large shear stresses in the material. Rolling may provide a more suitable mechanical rejuvenation method as the roll moves with the material to reduce the shear stresses. Similar to wall ironing, a pressure is induced which is expected to reduce the stress mismatch further. Furthermore, the high pressure may delay or prevent crystallization of the PET coating [76]. Rolling the polymer-coated steel to tailor the thermodynamic state of the coating prior to production is thus an interesting pre-processing step to explore.

Several authors studied the effect of cold-rolling on the mechanical properties of polymers [19, 47, 48]. Rolling of a coated material was investigated by Usov et al. [70] by deriving the exact solution in case of an elastic coating and a rigid substrate material. A functionally graded elastic coating was recently studied by Guler and coworkers [2, 35]. While these studies provide valuable insight into the mechanical behavior of a polymer during rolling, the behavior of a non-linear visco-elasto-plastic polymer coating on a steel substrate and the evolution of its thermodynamic state during rolling has not yet been investigated.

In this chapter, the mechanical response of a metal-polymer bi-layer material during rolling is investigated numerically using a non-linear visco-elasto-plastic material model for the PET coating. Furthermore, the change in the thermodynamic state is investigated as a means of pre-conditioning the material to prevent interface damage in subsequent deformation steps. Finally, the effect of the pre-conditioning on further deformation is studied in a proof-of-principle simulation of deformation-induced steel surface roughening.

This chapter is organized as follows. The constitutive model and computational procedures for the rolling simulations are presented in section 4.2. The simulation results are discussed in section 4.3. The proof-of-principle simulations are presented in section 4.4. The chapter ends with a discussion in section 4.5.

4.2 Constitutive and computational model

In this section, the material models for the polymer and steel are presented, along with their numerical implementation.

4.2.1 Polymer model

The studied coating consists of a PET layer with several additives to improve the PET-steel adhesion [15]. PET is a glassy polymer and almost fully amorphous (crystallinity is approx. 8%). An example of the typical intrinsic behavior of amorphous glassy polymers under uniaxial compression is shown in Fig. 4.3. The intrinsic behavior of glassy polymers is thus complex and accurate modeling requires an advanced constitutive model.

In the past two decades, strong effort was put into accurately modeling the behavior of glassy polymers, e.g. the work of Boyce et al [16] and Govaert and co-workers [17, 41]. These models incorporate the non-linear visco-elastic behavior, as well as strain softening and hardening and the effects of temperature and time. Here, the so-called Eindhoven Glassy Polymer (EGP) model is adopted which adequately captures the complete intrinsic mechanical response of amorphous polymers [17, 41]. The EGP model is a multi-mode, multi-process constitutive model [17]. In the present work only one mode and one process is considered due to limited set of known PET parameters, i.e. a single-mode, single-process approximation (SM-SP) is used. The mechanical analogue of the SM-SP EGP
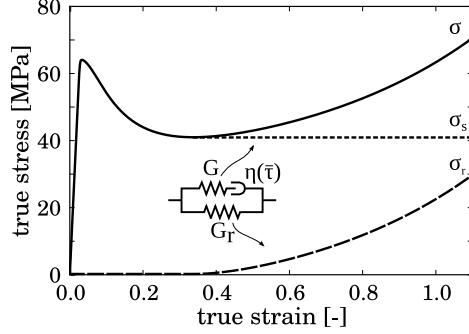
Figure 4.4: Mechanical analogue of the SM-SP EGP model (after [17]).

model is shown in Fig. 4.4. The essential equations of the SM-SP EGP model are detailed below.

In the EGP model the total stress is the addition of two contributions, i.e. the driving stress $\boldsymbol{\sigma}_s$ and the hardening stress $\boldsymbol{\sigma}_r$ (see also Fig. 4.4),

$$\boldsymbol{\sigma} = \boldsymbol{\sigma}_s + \boldsymbol{\sigma}_r. \tag{4.1}$$

The hardening stress originates from the rubber elastic contribution of the oriented entangled network and is described by a neo-Hookean relation,

$$\boldsymbol{\sigma}_r = G_r \tilde{\mathbf{B}}^d, \tag{4.2}$$

where G_r is the strain hardening modulus and $\tilde{\mathbf{B}}^d$ the deviatoric part of the isochoric left Cauchy-Green deformation (Finger) tensor. The driving stress incorporates the intermolecular interactions, i.e.

$$\boldsymbol{\sigma}_s = \boldsymbol{\sigma}_s^h + \boldsymbol{\sigma}_s^d = \kappa(J-1)\mathbf{I} + G\tilde{\mathbf{B}}_e^d, \tag{4.3}$$

where $\boldsymbol{\sigma}_s^h$ and $\boldsymbol{\sigma}_s^d$ are the hydrostatic and deviatoric stresses, respectively, κ is the bulk modulus, J is the volume change ratio, $\mathbf{I}$ is the second-order unity tensor, G is the shear modulus and $\tilde{\mathbf{B}}_e^d$ is the deviatoric part of the elastic isochoric Finger tensor. The quantities J and $\tilde{\mathbf{B}}_e^d$ evolve according to

$$\dot{J} = J\mathrm{tr}(\mathbf{D}), \tag{4.4}$$

$$\dot{\tilde{\mathbf{B}}}_e = (\tilde{\mathbf{L}} - \mathbf{D}_p) \cdot \tilde{\mathbf{B}}_e + \tilde{\mathbf{B}}_e \cdot (\tilde{\mathbf{L}}^\mathrm{T} - \mathbf{D}_p). \tag{4.5}$$

Here $\mathbf{L}$ is the velocity gradient tensor and $\mathbf{D}$ the deformation rate tensor. The plastic deformation rate tensor, $\mathbf{D}_p$ and $\boldsymbol{\sigma}_s^d$ are related by a non-Newtonian flow rule,

$$\mathbf{D}_p = \frac{\boldsymbol{\sigma}_s^d}{2\eta}, \tag{4.6}$$

with the viscosity

$$\eta = \eta_{0,ref} \frac{\bar{\tau}/\tau_0}{\sinh(\bar{\tau}/\tau_0)} \exp\left(\frac{\mu p}{\tau_0}\right) \exp(S), \tag{4.7}$$

where $\eta_{0,ref}$ is the zero-viscosity defined according to the reference state, τ_0 is the characteristic equivalent stress and μ is a pressure dependency parameter. The total equivalent stress, $\bar{\tau}$ and the pressure, p, are defined as

$$\bar{\tau} = \sqrt{\tfrac{1}{2}\boldsymbol{\sigma}_s^d : \boldsymbol{\sigma}_s^d}, \tag{4.8}$$

$$p = -\tfrac{1}{3}\mathrm{tr}(\boldsymbol{\sigma}). \tag{4.9}$$

The thermodynamic state parameter S contains the thermodynamic history dependence and is related to the equivalent plastic strain, $\bar{\varepsilon}_p$, i.e.

$$S(\bar{\varepsilon}_p) = S_a \cdot R(\bar{\varepsilon}_p). \tag{4.10}$$

Here S_a reflects the initial state of the polymer and $R(\bar{\varepsilon}_p)$ is a softening function, which incorporates the strain dependency of S. The softening function is described by a modified Carreau-Yasuda function [41],

$$R(\bar{\varepsilon}_p) = \frac{\left(1 + (r_0 \cdot \exp{(\bar{\varepsilon}_p)})^{r_1}\right)^{(r_2-1)/r_1}}{(1 + r_0^{r_1})^{(r_2-1)/r_1}}, \tag{4.11}$$

where r_0, r_1, r_2 are fitting parameters. R ranges between 0 (rejuvenated) and 1. In the current implementation the time dependence of S_a, i.e. physical aging is not included. Therefore, the yield stress does not increase with time and only the effect of mechanical rejuvenation is predicted with the present model. The equivalent plastic strain rate is defined as

$$\dot{\bar{\varepsilon}}_p = \frac{\bar{\tau}}{\eta}. \tag{4.12}$$

The PET material parameters used in this work are listed in Table 4.1 and the corresponding mechanical response during a uniaxial tensile test for an aged ($S_a = 13.3$ [-]) and rejuvenated ($S_a = 0$ [-]) PET layer is shown in Fig. 4.5(a). The parameters were taken from [52] for a similar amorphous PET grade. The parameters are not fully exact for the PET coating considered here. However, the parameters predict realistic PET behavior.

Table 4.1: Material properties of PET for the EGP model.

G_r [MPa]	κ [MPa]	G [MPa]	$\eta_{0,ref}$ [MPa·s]	τ_0 [MPa]
4.7	1800	812	$3 \cdot 10^8$	1.262

μ [-]	S_a [-]	r_0 [-]	r_1 [-]	r_2 [-]
$4.8 \cdot 10^{-2}$	13.3	0.98	20	-3.5

4.2.2   Steel

Similar to the work of Van den Bosch et al. [14], an isotropic elasto-plastic constitutive material model with a Von Mises yield criterion is used. Hardening is modeled using an isotropic power-law, i.e.

$$\sigma_y = H \left(\varepsilon_0 + \bar{\varepsilon}_p\right)^n, \tag{4.13}$$

where H, ε_0 and n are material parameters and $\bar{\varepsilon}_p$ is the effective plastic strain. The parameters are given by $H = 477$ [MPa], $\varepsilon_0 = 2 \cdot 10^{-3}$ [-] and $n = 0.1$ [-]. The Young's modulus is $E = 210$ [GPa] and the Poisson's ratio is $\nu = 0.3$ [MPa]. The mechanical response of the steel substrate is shown in Fig. 4.5(b).
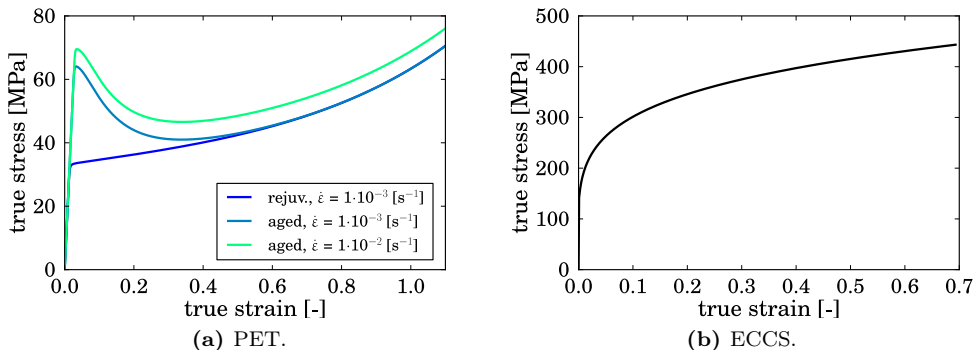
Figure 4.5: Mechanical response of the two modeled materials; note that $S_a = 0$ [-] for rejuvenated and $S_a = 13.3$ [-] for aged PET.

4.2.3 Friction model

Friction between the roll and the PET coating is modeled using the Coulomb friction law, i.e.

$$||\vec{f}_t|| < \mu_f f_n, \quad \text{(stick)}, \tag{4.14}$$

$$\vec{f}_t = -\mu_f f_n \vec{t} \quad \text{(slip)}, \tag{4.15}$$

where $\vec{f}_t$ is the tangential friction force, and f_n is the normal force, μ_f is the friction coefficient and $\vec{t}$ is the tangential vector in the direction of the relative velocity $\vec{v}_r$ between the roll and the coating,

$$\vec{t} = \frac{\vec{v}_r}{||\vec{v}_r||} \tag{4.16}$$

The transition between stick and slip is a step function, which is numerically inconvenient. Thus, $\vec{f}_t$ is approximated by an arctangent function, i.e.

$$\vec{f}_t = -\frac{2\mu_f f_n}{\pi} \arctan\left(\frac{||\vec{v}_r||}{\delta}\right) \vec{t}, \tag{4.17}$$

where the value of δ sets the value of the relative sliding velocity above which sliding occurs. In [17] it was found that $0.01 \cdot ||\vec{v}_r|| \leq \delta \leq 0.1 \cdot ||\vec{v}_r||$ gives realistic results. The friction coefficient is based on values commonly seen for PET and, unless otherwise stated, is set to $\mu_f = 0.2$ [-] [57].

4.2.4 Computational model

The two-dimensional plane strain computational model for the rolling process is shown in Fig. 4.6. Obviously, the roll radius (R = 35 [mm]) is considerably larger than the thickness of the simulated material (steel: 105 [µm], PET: 15 [µm]). The roll is assumed to be infinitely stiff and is modeled as a rigid body. Symmetry is assumed along the bottom of the steel layer.

In the industrial forming process, the steel substrate is rolled to its desired thickness prior to applying the coating. The roll creates a smooth surface in the rolling direction (see also Fig. 4.13(a)). Here, the pre-conditioning rolling step is assumed to be performed in the rolling direction of the steel. It is therefore assumed that the initial surface profile of the steel, and hence the PET-steel interface, is flat.

Rolling is performed by moving the rotating roll over the polymer-coated steel at a fixed velocity $v = \omega \cdot R$, where ω is the rotational speed and R the radius of the roll. The right edge of the polymer-coated steel is fixed in the x-direction. Furthermore, considering that only part of a polymer-coated steel plate is modeled, the left edge is kept straight. This may result in edge effects near the right and left boundaries and thus only the response of the dashed central region (see Fig. 4.6) is analyzed. The dashed region is modeled as a separate body to study the PET-steel interface stress that develops during rolling. The interface stress is calculated from the force required to fix the dashed PET region to the steel substrate.

In the current simulations, the roll rotational speed is set to $\omega = 1.745 \cdot 10^{-3}$ [rad·s^{-1}] to ensure that the applied strain rate during rolling stays within the experimental regime used to determine the EGP model parameters, i.e. the strain rate should not exceed $\dot{\varepsilon} = 1 \cdot 10^{-2}$ [s^{-1}]. The commonly used industrial strain rate is higher, in the order of $\dot{\varepsilon} = 1 \cdot 10^{3}$ [s^{-1}]. Simulating such high rolling speeds requires dedicated experiments to quantify the PET response at higher strain rates. The increased strain rate may result in additional dynamical effects, i.e. the mismatch in strain rates allows for a qualitative prediction only.

As discussed in the introduction, the work of Van der Aa et al. [1] revealed that the pressure imposed to the polymer coating during wall ironing may reduce the interface stresses to prevent delamination. As rolling also imposes a pressure to the coating it can be assumed that the polymer-steel interface remains intact during rolling. Thus, for simplicity, the interface is not modeled explicitly, i.e. perfect adhesion is assumed. This assumption is investigated by analyzing the stress at the PET-steel interface.
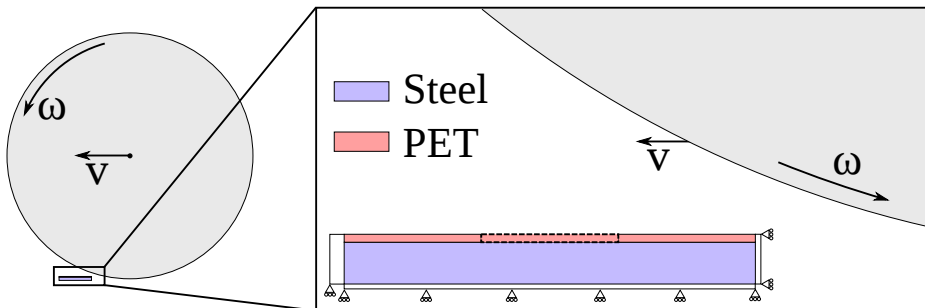

Figure 4.6: Sketch of the simulated rolling process.

4.3   Results

4.3.1   Evolution of the thermodynamic state

The evolution of the average value of the thermodynamic state parameter $\bar{S}$ as a function of time for a rolling reduction (i.e. the thickness reduction) of 10% and a friction coefficient of $\mu_f = 0.2$ [-] is shown in Fig. 4.7. $\bar{S}$ is the average thermodynamic state (S, see Eq. (4.10)) within the dashed region in Fig. 4.6. Five stages can be identified, i.e. 1) initially the value remains constant as the roll has not yet entered the dashed region; 2) as soon as the roll starts to plastically deform the PET coating, the thermodynamic state parameter drops rapidly; 3) the parameter stabilizes shortly when the material passes underneath the roll; 4) a further drop in the parameter is noticed as the region of interest leaves the roll and starts to unload; and 5) finally, the value stabilizes at a value of approximately $\bar{S} \approx 2$ [-].

The final average state parameter ($\bar{S}_{final}$, stage 5) as a function of the imposed rolling reduction is shown in Fig. 4.8. Clearly, the average thermodynamic state after rolling decreases from its initial value of $S_a = 13.3$ [-] with increasing rolling reduction. The dependence on the imposed reduction is non-linear with an initial steep decrease. Full rejuvenation ($\bar{S} = 0$ [-]) is only reached for large rolling reductions. The numerical-experimental study presented in chapter 3 showed that interface damage is minimized when the initial thermodynamic state of the coating prior to production is around $\bar{S} \approx 2$ − 2.5 [-]. Rolling to a reduction of about 10% is thus desired to reach this optimum value.
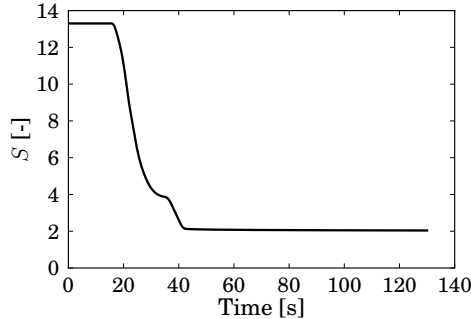

Figure 4.7: Evolution of the average thermodynamic state parameter $\bar{S}$ as a function of time; rolling reduction 10%; friction coefficient $\mu_f = 0.2$ [-].

4.3.2   Interface stress

The interface stress during rolling is shown in Fig. 4.9. The normal interface stress (Fig. 4.9(a)) is compressive during rolling and increases with increasing reduction. Compressive stresses applied to the interface typically do not result in interface damage. This is also commonly assumed in cohesive zone approaches where a negative opening results in interface strengthening [12]. The tangential interface stress (Fig. 4.9(b)) shows an initial maximum, followed by a minimum. The extreme values of the stress clearly increase (in absolute sense) with increasing reduction. The interface must remain intact during rolling to withstand the tangential interface stress. Clearly, the higher the rolling reduction, the higher the interface stress. Whether the interface remains really intact during this process should be investigated experimentally.
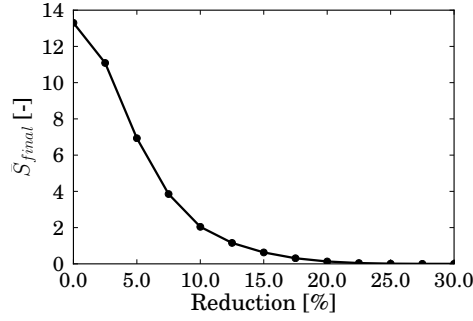
Figure 4.8: Evolution of the final average thermodynamic state parameter $\bar{S}_{final}$ as a function of the rolling reduction; time 120 [s]; friction coefficient $\mu_f = 0.2$ [-].

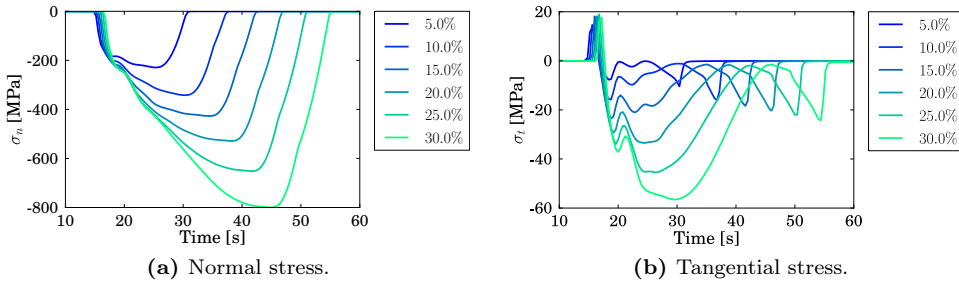(a) Normal stress.

(b) Tangential stress.

Figure 4.9: (a) Normal and (b) tangential stresses acting on the interface during rolling for different rolling reductions; friction coefficient $\mu_f = 0.2$ [-].

Influence of friction

The influence of the friction coefficient on the interface stresses during rolling was investigated. The interface stress in normal and tangential direction for a friction coefficient varying between 0 and 0.3 is shown in Fig. 4.10. The compressive normal stress (Fig. 4.10(a)) increases with an increase in the friction coefficient. The tangential stress (Fig. 4.10(b)) shows a different trend. Three different extremes are visible in the stress during rolling, i.e. 1) a maximum when the material enters the roll (=entrance); 2) a minimum just after entering the roll (=under); and 3) another minimum as the material leaves the roll (=exit). The highest stress magnitude depends on the friction coefficient. Fig. 4.11 shows the magnitude of the tangential stress reached in the different stages during rolling. Clearly, the global maximum value is seen in different regions depending on the friction coefficient. For small values of the friction coefficient, the maximum tangential stress is reached when the material enters the roll. The friction reduces the interface stress in this regime as it guides the material under the roll and thus a decrease of this maximum is seen when the friction coefficient is increased. For high values of the friction coefficient the magnitude of the stresses under the roll increases. The location of the global maximum changes. The magnitude of the exit stress shows a less pronounced increase with increasing friction coefficient and typically is lower than the other two extreme values. Clearly, the magnitude of the interface stresses depends on the friction coefficient and an optimum in the coefficient exists which minimizes the maximum.
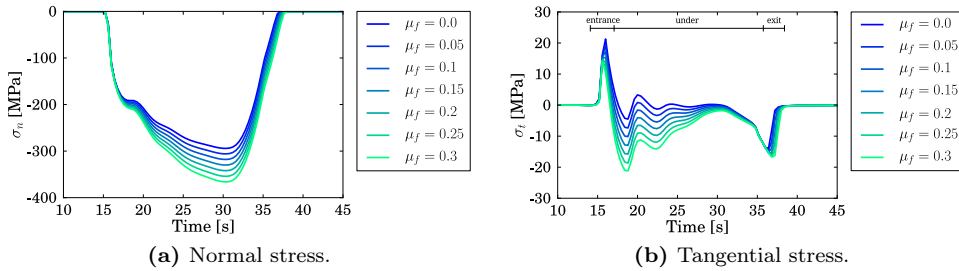
(a) Normal stress.   **(b)** Tangential stress.

Figure 4.10: (a) Normal and (b) tangential stresses acting on the interface during rolling for different friction coefficients; reduction is 10%.
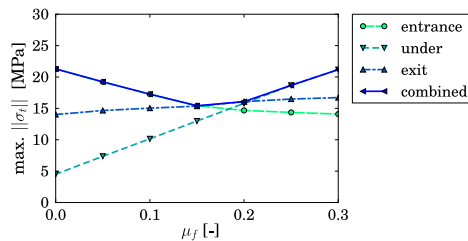

Figure 4.11: Maximum magnitude of the tangential interface stress for different values of the friction coefficient and for different moments during rolling (see also Fig. 4.10(b)); reduction is 10%.

4.3.3 Influence on mechanical behavior

To characterize the effect of the rolling process on the mechanical behavior of the PET coating after rolling, the dashed central region of the PET coating (see Fig. 4.6) was subjected to a plane-strain tensile test after rolling. The resulting engineering stress-strain response for different rolling reductions and a friction coefficient of $\mu_f = 0.2$ [-] is shown in Fig. 4.12. The results predict softening for all simulated rolling reductions, i.e. a drop in the stress emerges after the yield point is reached. After rolling, small imperfections are present which trigger localization in the subsequent tensile test. Note that the softening in the response is dependent on the rolling reduction., i.e. a larger rolling reduction shows less softening in the tensile test.

These results are compared to the work of Broutman et al. [19], who studied the influence of rolling on the mechanical response of different polymers in a tensile test. These results apply to rolling of the polymer only and not for rolling of a polymer-coated steel, i.e. the results can be compared qualitatively only. The resulting dependency on the rolling reduction was also found in [19], indicating that the predicted effect of rolling, at least qualitatively, compares well to experiments.
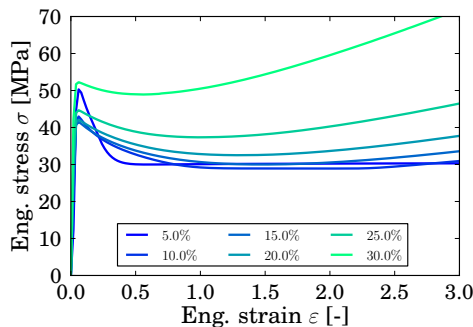
Figure 4.12: Engineering stress-strain response of the PET coating after rolling the bilayer material to different rolling reductions; friction coefficient $\mu_f = 0.2$ [-].

4.4 Proof-of-principle simulation

As mentioned in the introduction, the goal of pre-conditioning the polymer-coated steel via rolling is to delay or possibly prevent the initiation and growth of interface damage during subsequent forming operations. The previous section confirmed that rolling may provide a method to mechanically rejuvenate the coating to the desired optimal thermo-dynamic state. In order to assess the effect of the pre-conditioning, proof-of-principle simulations are performed next.

Recent experimental results revealed that deformation-induced roughening of the polymer-steel interface plays an important role in the initiation and growth of inter-face damage [25]. During production, the polymer-steel interface experiences a significant change in roughness due to the deformation-induced roughening of the steel substrate material. The polycrystalline steel roughens due to the differences in crystallographic orientation between grains and other plasticity related phenomena [54]. An example of this change in surface roughness for a packaging steel deformed in tension is shown in Fig. 4.13. The initial surface profile (Fig. 4.13(a)) is characterized by a rolling profile induced by the rolls (used to reduce the steel to its desired thickness). This profile is visible as grooves along the x-direction, i.e. in the rolling direction (RD). After performing a uniaxial tensile test in the x-direction to the steel, a change in roughness profile is measured, see Fig. 4.13(b). The comparison between the initial and final profile shows that the change in roughness occurs over a wide range of length scales, ranging from the scale of individual dislocations to the size of multiple grains. The resulting profile depends on the deformation conditions and the material properties [54].

The numerical-experimental framework developed in chapter 3 allows for a detailed study of the effect of a change in interface roughness on the interface integrity of these polymer-coated steels. This framework is here applied to illustrate the effect of the pre-conditioning on the interface integrity during subsequent deformation processes. Two simulations of deformation-induced interface roughening during a tensile test were performed, i.e. a simulation where the PET coating is aged ($S_a = 13.3$ [-]) and a simulation where the PET is rejuvenated to the optimal value ($S_a = 2.5$ [-]) prior to tensile testing.

For the simulations it is assumed that the internal stresses within the polymer layer after rolling are small. Furthermore, since it was assumed that the interface remains intact during pre-conditioning, the interface is initially intact. Finally, it is assumed that the surface roughness profile of the steel does not change during rolling. These

assumptions limit the proof-of-principle simulation to a qualitative comparison of the effect of pre-conditioning only. For a quantitative prediction the full deformation history of the PET coating, interface and steel substrate must be taken into account. Quantitative predictions of the interface integrity and the deformation-induced steel surface roughening during rolling requires a steel constitutive model that accurately predicts the roughening process. However, quantitative models for predicting roughening in steels at multiple length scales are not yet available [75].
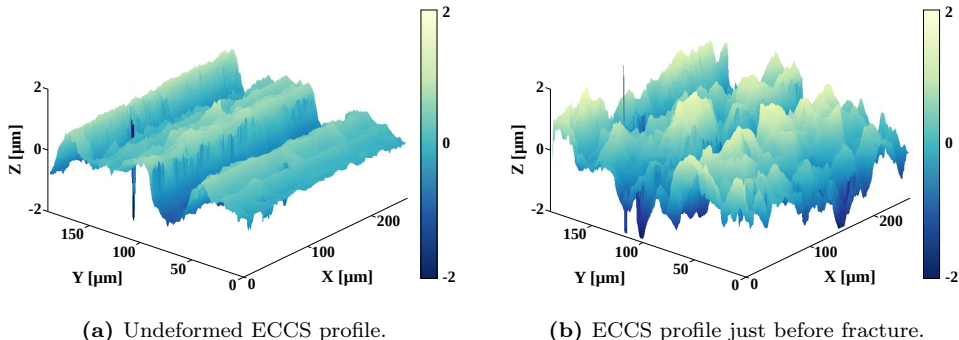

(a) Undeformed ECCS profile.　　　　　　**(b)** ECCS profile just before fracture.

Figure 4.13: (a) Initial and (b) final surface profile of an ECC steel during a uniaxial tensile test, measured with a confocal optical profiler; X-direction is the tensile direction; colors indicate the local surface height in microns.

4.4.1　Numerical-experimental framework

Experimental

A tensile test is performed along the rolling direction of TH340 packaging steel. TH340 is a continuously annealed, single reduced, DWI (draw-redraw-wall ironing) quality aluminium-killed low carbon ferritic ECCS sheet. The steel sheet is 210 [µm] thick. After each tensile strain increment of $\Delta\varepsilon = 0.25\%$, a confocal optical height measurement is taken. The initial and final surface profile are shown in Fig. 4.13. These confocal height profiles are used in a Finite Element based Digital Image Correlation method (FE-DIC) (presented in chapter 2) to extract the full-field displacement field that accompanies the change in surface roughness of the steel. The extracted displacement field along a line initially located on $y = 100$ [µm], shown in Fig. 4.14, is used in the proof-of-principle simulations.

The displacement field is applied in a two-dimensional plane strain simulation of a polymer-coated steel. As a result, the steel does not have to be modeled explicitly, since the measured experimental displacements are directly applied to the interface. A sketch of the computational model is shown in Fig. 4.15. The PET coating is modeled using the EGP model with the parameters listed in Table 4.1.
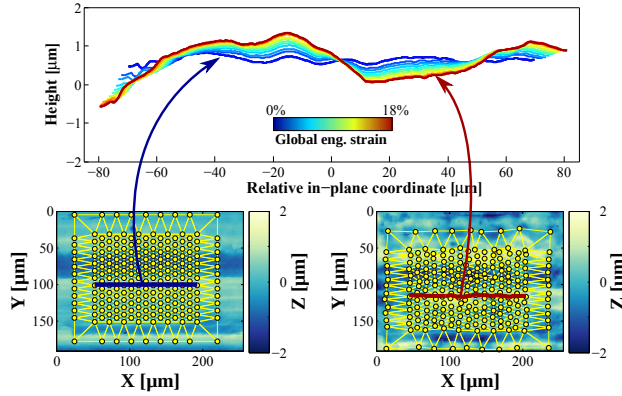
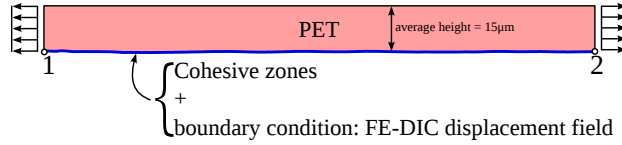**Figure 4.14:** Evolution of a line profile initially located at $y = 100$ [µm].

Figure 4.15: Sketch of the computational framework.

Interface model

The interface between the PET and ECCS is modeled using Cohesive Zone elements. The mixed-mode traction-separation law developed by Van den Bosch et al. [12] is used to describe the PET-steel interfacial decohesion. The cohesive zone law was discussed in detail in section 3.3.2. The important equations are repeated here. The exponential law is split into two contributions, i.e.

$$T_n \left(\Delta_n, \Delta_t \right) = \frac{\phi_n \Delta_n}{\delta_n^2} \exp \left(-\frac{\Delta_n}{\delta_n} \right) \exp \left(-\frac{\Delta_t^2}{\delta_t^2} \right), \qquad (4.18)$$

$$T_t \left(\Delta_n, \Delta_t \right) = 2 \frac{\phi_t \Delta_t}{\delta_t^2} \left(1 + \frac{\Delta_n}{\delta_n} \right) \exp \left(-\frac{\Delta_n}{\delta_n} \right) \exp \left(-\frac{\Delta_t^2}{\delta_t^2} \right), \qquad (4.19)$$

where n and t are the normal and tangential directions, respectively, Δ is the cohesive zone opening, ϕ is the work of separation and δ is the characteristic opening length. The typical traction-separation response is shown in Fig. 4.16.

An integrity parameter ξ is used to quantify the fraction of the work of separation that is not yet dissipated in the cohesive zone element as presented in section 3.3.2,

$$\xi = 1 - \frac{\Omega}{\phi}, \quad \xi \in [0, 1], \qquad (4.20)$$

where Ω is the consumed work of separation in the cohesive zone.

To determine the parameters of the cohesive law, dedicated experiments are needed. It is known from literature that different parameters may result from different experiments [72]. An example of two experiments that result in a different work of separation (ϕ) are the measurements of Fedorov et al. [28] and Van den Bosch et al. [15]. The differences

(a) Normal direction.
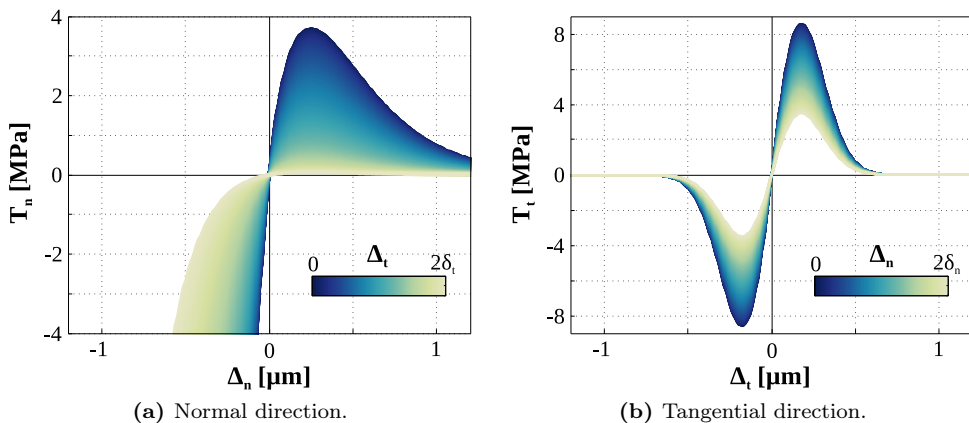
(b) Tangential direction.

Figure 4.16: The coupled exponential traction-separation law of Van den Bosch et al. [12], using the parameters of Table 4.2.

are explained by the distinct energy dissipated within the process zone, i.e. in the bulk material near the interface. For the proof-of-principle simulations, parameters are required that are characteristic for small-scale de-bonding [25]. The work of separation determined by Fedorov et al. [28] is used here. As the cohesive law used is different, the δ_n and δ_t parameters are estimated based on the results in [28]. The resulting parameters used are listed in Table 4.2. Note that $\phi_n = \phi_t = \phi$ and $\delta_n = \delta_t = \delta$.

Table 4.2: Cohesive zone constants used in the proof-of-principle simulations.

ϕ_n [J·m^{-2}]	ϕ_t [J·m^{-2}]	δ_n [µm]	δ_t [µm]
2.5	2.5	0.25	0.25

4.4.2   Results

The equivalent Von Mises stress and the equivalent plastic strain in the aged PET coating ($S_a = 13.3$ [-]) at a global tensile strain of $\varepsilon = 6\%$ and $\varepsilon = 11.5\%$ is shown in Figs. 4.17 and 4.18, respectively. The strains show pronounced localization with delamination at the interface as a result. The high stress in the localization band triggers interface damage (see Fig. 4.17). This damage grows as the deformation increases, see Fig. 4.18. The simulation of the mechanically rejuvenated coating at a global tensile strain of $\varepsilon = 11.5\%$ is shown in Fig. 4.19. A clear difference in predicted interface damage is visible compared to the damage depicted in Fig. 4.18. Rejuvenation removes or reduces the softening branch from the intrinsic PET response (see also Fig. 4.5(a)). This softening triggers the localization events in the aged PET coating. The localization in case of the rejuvenated PET coating is clearly less pronounced.

The interface integrity over the line profile at a global tensile strain of $\varepsilon = 11.5\%$ is shown in Fig. 4.20. A large drop in the interface integrity is visible for the aged coating, see Fig. 4.20(a). However, the simulation with the rejuvenated PET coating shows significantly less reduction in integrity, indicating that less interface damage occurs, see Fig. 4.20(b).
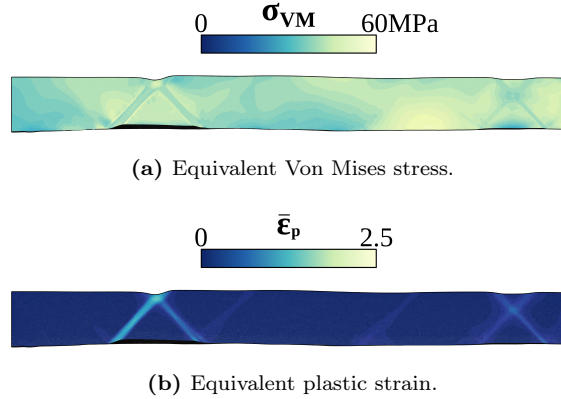
(a) Equivalent Von Mises stress.

(b) Equivalent plastic strain.

Figure 4.17: Predicted equivalent Von Mises stress (a) and equivalent plastic strain (b) in the aged polymer coating along the line initially located at $y = 100$ [µm] at a globally applied tensile strain of $\varepsilon = 6\%$; the failed interface elements are colored black.

(a) Equivalent Von Mises stress.

(b) Equivalent plastic strain.
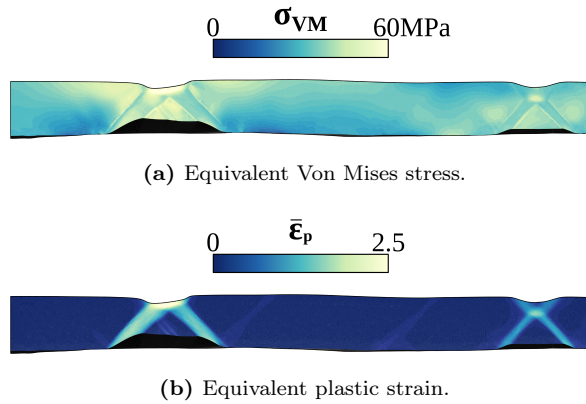
Figure 4.18: Predicted equivalent Von Mises stress (a) and equivalent plastic strain (b) in the aged polymer coating along the line initially located at $y = 100$ [µm] at a globally applied tensile strain of $\varepsilon = 11.5\%$; the failed interface elements are colored black.

4.5   Discussion

The rolling simulations of a polymer-coated steel enabled a detailed study of the evolution of the thermodynamic state of the coating as a function of the rolling reduction and other parameters.

Dedicated experiments are required to assess the validity of assumptions used in the rolling simulations, e.g. the assumed perfect adhesion. An indication of the validity of this assumption is provided by the interface stress that develops during rolling (see Fig. 4.9). Clearly, the stresses depend on the reduction. The normal interface stress (σ_n) is always in compression due to the rolling process, which typically does not damage the interface. However, the tangential interface stress also increases with increasing reduction, which may lead to interface damage. Thus, to reduce the interface stress, the reduction has to be minimized. However, a minimum reduction is required to rejuvenate the PET coating to

(a) Equivalent Von Mises stress.

(b) Equivalent plastic strain.

Figure 4.19: Predicted equivalent Von Mises stress (a) and equivalent plastic strain (b) in the rejuvenated polymer coating along the line initially located at $y = 100$ [μm] at a globally applied tensile strain of $\varepsilon = 11.5\%$; the failed interface elements are colored black.
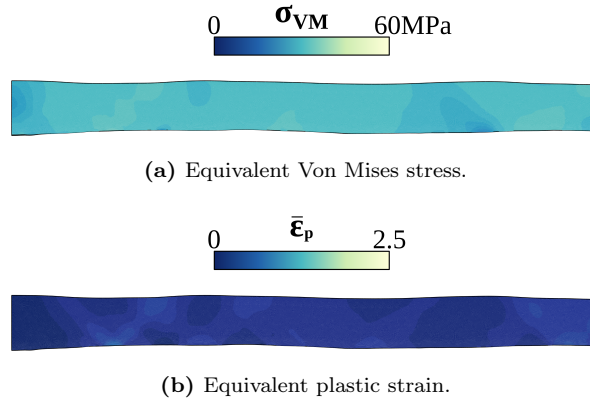

(a) Aged PET.
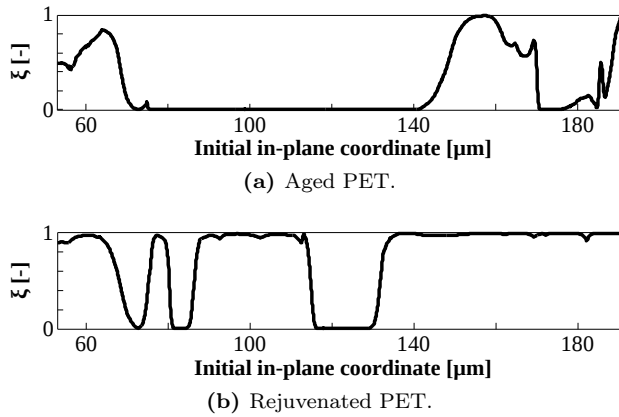
(b) Rejuvenated PET.

Figure 4.20: Interface integrity profile at $\varepsilon = 11.5\%$ for the aged (a) and rejuvenated (b) PET over the line initially located at $y = 100$ [μm].

the desired thermodynamic state and thus cannot be chosen arbitrarily. Research by Van der Aa [1] showed that during wall ironing the imposed pressure hardens the PET coating. It was found that decreasing the die angle during wall ironing (see Fig. 4.2(c)) resulted in a more distributed compressive stress. Although the deformation conditions during wall ironing are different from those in rolling, it is expected that also here the effect of pressure is paramount. The hardening of the PET coating decreases the stress mismatch between the coating and the steel substrate. This may lower the interface stress during rolling. Thus, changing the roll radius may decrease the interface stress further. Fig. 4.21 shows the effect of changing the roll radius on the magnitude of the tangential interface stress during rolling, confirming the expected influence on the interface stress. The roll must be sufficiently large to prevent interface failure. Furthermore, the study on the effect of the friction coefficient revealed an optimum value which reduces the maximum magnitude of the tangential interface stress to a minimum. Whether the friction coefficient can be

Figure 4.21: Maximum magnitude of the tangential interface stress as a function of the roll radius; reduction 10%; friction coefficient $\mu_f = 0.2$ [-].
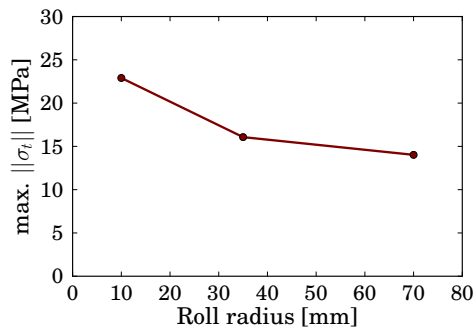
optimized has to be investigated experimentally.

The proof-of-principle simulations currently only include the change in thermodynamic state of the coating. The simulations may be extended to a coupled analysis where the polymer-coated steel is first rolled, after which a subsequent deformation process is applied. It is expected that a coupled study may reveal a different optimum for the thermodynamic state, as full rejuvenation of the coating requires a large reduction in thickness (see also Fig. 4.8), which increases the stresses at the interface. However, the conclusion that the rejuvenated material shows less interface damage is expected to persist.

4.6   Conclusion

A novel methodology was presented for pre-conditioning a polymer-coated steel used in food and beverage packaging. Previous research showed that pre-conditioning the thermodynamic state of the polymer coating prior to production may significantly reduce damage in the interface during production. In this chapter, the prior mechanical rejuvenation of the coating via rolling was explored. Numerical simulations of rolling were performed on a polymer-coated steel and the evolution of the thermodynamic state of the coating was studied. The simulations showed that changing the rolling reduction allows for optimization of the thermodynamic state. Furthermore, proof-of-principle simulations were performed using a previously developed numerical-experimental framework to study the effect of the rejuvenation on subsequent deformation. Deformation-induced steel surface roughening was simulated and the predicted interface damage was compared to a simulation without pre-conditioning. The comparison revealed a significant decrease in the predicted interface damage after rejuvenating the polymer coating.

The simulations provide valuable insight into the influence of rejuvenating a polymer coating and can be used to optimize the industrial process to reduce or even prevent interface delamination.

PREDICTING DEFORMATION-INDUCED POLYMER-STEEL INTERFACE ROUGHENING AND FAILURE

Based on
Van Beeck, J., Maresca, F., De Geus, T.W.J., Schreurs, P.J.G., Geers, M.G.D.
submitted

Abstract

A novel integrated framework is presented for the prediction of deformation-induced interface roughening and failure in polymer-coated steels. Crystal plasticity is employed to predict the change in steel surface roughness in-situ. The steel substrate is coated with a thin polymer layer and the polymer-steel interface is modeled using an exponential cohesive zone law. Uniaxial tensile simulations are performed and the results show that the predicted roughness increases with the applied deformation. The local changes in the steel surface profile result in initiation and growth of local interface failure. Furthermore, a compression simulation shows that the roughening rate of the steel is increased compared to tension, with an increase in the predicted interface damage as a result. The presented framework thus allows for a detailed numerical study of the initiation and growth of interface damage in polymer-coated steels during applied deformation. The incorporation of the crystal plasticity model to predict the changes in the steel surface profile complements the cumbersome measurements of detailed experimental displacement fields that accompany deformation-induced roughening and thus enables the analysis of deformation processes where measuring the steel surface profile is difficult if not impossible, e.g. industrial forming processes such as deep drawing.

5.1 Introduction

Deformation-induced surface roughening of steels and other crystalline materials is common in many engineering applications. This change in surface roughness can lead to several problems during manufacturing [6, 25, 55], for example: (1) a detrimental effect on the surface finish of sheet metal; (2) a change in friction, wear and corrosion resistance; (3) localization phenomena which may lead to failure; or (4) local delamination of a coating (see chapter 3).

In case of polymer-coated steels, the change in surface roughness may also result in local delamination of the coating. This is particularly the case for industrial manufacturing of food and beverage cans or canisters, see Fig. 5.1. To reduce the environmental impact of the production process, the Electrolytically Chromium Coated Steel (ECCS) sheet material is pre-coated with a Polyethylene Terephthalate (PET) layer prior to can production.

Compared to the traditional manufacturing process of producing a blank steel can which is coated after production, using a pre-coated steel reduces the energy consumption and CO_2 emission with one third and the process water and resulting solid wastes to practically zero [1].

However, it is observed in practice that the polymer-steel interface is damaged due to the large deformations at high strain rates, temperatures and pressures during production. It has been shown experimentally that this is due to the evolving steel surface roughness. The food and beverage industry demands that the material does not exhibit any visible or invisible damage after production and during the prolonged shelf-life, as this compromises the quality of the canned content [9, 25].
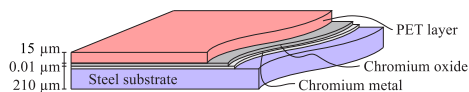

Figure 5.1: Polymer-coated steel used in the manufacturing of food and beverage cans (after [15]).

The effect of deformation-induced roughening of the steel substrate was investigated in a numerical-experimental framework in chapters 2 and 3. Experimental height profiles of a steel deformed in tension were used in a Finite Element based Digital Image Correlation (FE-DIC) calculation to extract the full-field displacement fields from height measurements (chapter 2). These displacement fields were applied as boundary conditions in a numerical analysis of a polymer coating and an interface model. It was thereby observed that the initiation and growth of interface damage is a result of the change in steel surface roughness (chapter 3).

However, applying the developed framework to other deformations than uniaxial tensile tests is infeasible. In-situ measurement of the evolving micro-scale surface height profiles in industrial forming operations like deep (re-)drawing and wall ironing is not possible. To predict the change in surface roughness and the effect on the interface integrity of coated products during manufacturing, a predictive model for the evolution of the steel surface profile is desired.

Crystal plasticity can be used to predict the anisotropic crystallographic response of a metal [18]. Several authors have studied the applicability of these models for predicting deformation-induced surface roughening. Becker [6] and Wu & Lloyd [73] studied two-dimensional roughening and reported differences in the predicted roughness amplitude compared to experimental observations. Both authors concluded that the adopted two-dimensional assumption may well result in the observed difference. More recently, Zhao et al. [75] and Lim et al. [45] studied oligocrystals using three-dimensional crystal plasticity and compared the predictions with experiments. They found a relatively good comparison with the experiments for the displacement fields and resulting height profiles. However, small differences prevailed because discrete roughening phenomena, e.g. slip extrusions, can not be captured by the continuum model.

Strain gradient crystal plasticity modeling was also explored as a means of predicting the change in surface roughness. Borg & Fleck [11] and Nygårds & Gudmundson [49] studied the effect of the internal length scale in the strain gradient model and found a strong dependency of the resulting profile on this length scale. However, so far no experimental comparison was made to determine the internal length scale.

These above mentioned studies focused on predicting deformation-induced surface roughening during uniaxial tension. Bending was recently studied by Rossiter et al. [55] for aluminium sheets using a crystal plasticity model. The simulations showed the formation of hills and valleys on the surface and the predicted roughness was found to depend on the subsurface grains. Finally, Šiška et al. [60] performed cyclic simulations on copper thin films. The roughness was found to increase with cycling and cycling between tension and compression resulted in a larger roughness than cycling in pure tension or pure compression. The predicted roughness was smaller than seen in experiments due to the limited number of simulated cycles.

Deformation-induced roughening and its influence on the interface integrity of a coating has not yet been investigated numerically using a predictive model for the steel roughening. In this chapter, a numerical framework is developed that enables study of deformation-induced interface roughening in polymer-coated steels. A crystal plasticity model [18] is employed to qualitatively predict the change in surface roughness of a polymer-coated packaging steel. The polymer coating is modeled using the Eindhoven Glassy Polymer model [17] to accurately predict the mechanical response of the coating. The interface between the polymer and steel is modeled using an exponential cohesive zone law [12], enabling analysis of the interface integrity during the deformation process. Uniaxial tension and compression simulations are performed and the results are qualitatively compared to experimental measurements of a packaging steel deformed in tension. The presented framework may be incorporated into a global-local approach to allow the analysis of a particular industrial forming processes such as deep drawing, e.g. by embedding the modeled domain into a bulk simulation or a multi-scale approach. Since the objective of this chapter is focused on a qualitative predictions, some assumptions have to be made that impose limitations on the presented results. 1) The continuum assumption in the crystal plasticity framework limits the predicted roughening to grain-scale features only, i.e. micro-scale discrete roughening phenomena are not incorporated into the current framework. 2) The adopted steel crystallography is numerically generated based on available experimental data using a representative method. However this can never capture the complete experimental texture. 3) Due to computational limitations, the finite element discretization is relatively coarse, limiting the amount of bending that can be described by the discretization. Nevertheless, it will be shown that the predicted roughness patterns do not drastically change with mesh refinement.

This chapter is organized as follows. The problem, constitutive models and computational procedures for the simulations are presented in section 5.2. The simulation results are discussed in section 5.3. The chapter ends with a discussion and conclusion.

5.2 Constitutive and computational model

5.2.1 Problem statement

The studied material is a packaging steel used in the production of food and beverage cans known as TH340. The material consists of an Electrolytically Chromium Coated steel (ECCS) substrate, coated with a 15 [µm] thick PET coating, see also Fig. 5.1. A small block with in-plane dimensions 100×100 [µm] of the packaging material is modeled, whereby the steel surface is initially flat (schematically shown in Fig. 5.2(a)). The steel thickness is 20 [µm]. This block is assumed in-plane periodic (i.e. parallel to the interface). In addition to the in-plane periodic boundary conditions, the boundary conditions are

set to prevent rigid body rotations and global shear perpendicular to the interface, see Fig. 5.3(a). Furthermore, the presence of the bulk steel below the modeled block is considered using specific boundary conditions that take into account the restrictions imposed by the bulk on the steel substrate. While different choices for these boundary conditions are possible, here parts of the bottom steel face (areas of 20×20 [µm], i.e. an average of 2×2 grains) are constrained with an average z-displacement of zero. The effect of this boundary condition was studied by varying the constrained domain size and it was found that the boundary condition does not drastically change the predicted results.

An average uniaxial tension and compression strain is applied at a linear strain rate of $\dot{\varepsilon} = 3.75 \cdot 10^{-2}$ [s^{-1}]. The steel is modeled using the crystal plasticity model detailed in the next section. The polymer-steel interface is described using an exponential cohesive zone law, discussed further in section 5.2.3. The PET coating is modeled using the Eindhoven Glassy Polymer model described in section 5.2.4.

An EBSD measurement was performed on the packaging steel to analyze the average grain size and distribution of Euler angles, see Fig. 5.2(b). The measurement revealed that the steel grains have a BCC ferrite crystal structure and are approximately equi-axed with an average grain diameter of about 10 [µm].
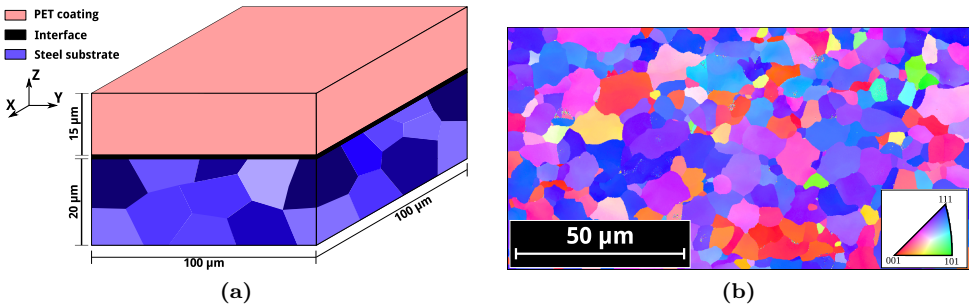
Figure 5.2: (a) Sketch of the modeled part of the polymer-coated steel; (b) results of an EBSD measurement on TH340 packaging steel; the colors indicate the crystal orientations.

5.2.2 Steel crystal plasticity framework

A conventional crystal plasticity model [18] is adopted for the BCC ferritic steel. Within this continuum approach, the effect of dislocation glide on slip systems is modeled in an average sense. Effects due to e.g. dislocation pile-ups are disregarded.

The deformation gradient $\mathbf{F}$ is multiplicatively split into an elastic $\mathbf{F}_e$ and plastic $\mathbf{F}_p$ contribution, i.e.

$$\mathbf{F} = \mathbf{F}_e \cdot \mathbf{F}_p. \tag{5.1}$$

The multiplicative split introduces an intermediate configuration, which is distorted by the plastic deformation only (see Fig. 5.4). The elastic deformation, as well as rotations, are included in $\mathbf{F}_e$. The plastic part of the velocity gradient $\mathbf{L}$ is $\mathbf{L}_p = \dot{\mathbf{F}}_p \cdot \mathbf{F}_p^{-1}$. In the crystal plasticity setting, the crystallographic decomposition of $\mathbf{L}_p$ is

$$\mathbf{L}_p = \sum_{\alpha=1}^{n_s} \dot{\gamma}^\alpha \mathbf{P}_0^\alpha, \tag{5.2}$$

Figure 5.3: (a) Boundary conditions used in the tension and compression simulations, and (b) sketch of the bottom face of the modeled steel volume 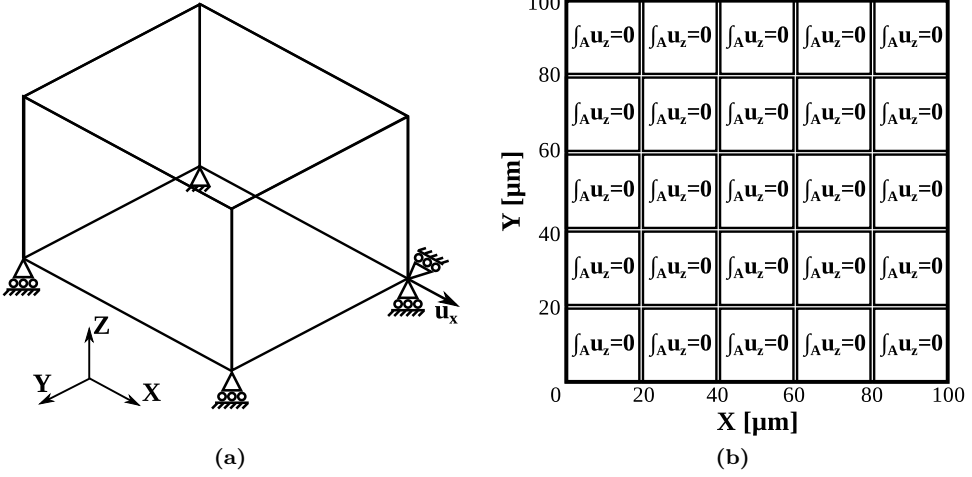illustrating the bottom boundary condition used to account for the presence of bulk steel below the modeled steel region; the average z-displacement of each region is constrained to zero.

where $\mathbf{P}_0^\alpha = \vec{s}_0^\alpha \otimes \vec{n}_0^\alpha$ is the Schmid tensor of the slip system α, $\vec{s}_0^\alpha$ is the slip direction and $\vec{n}_0^\alpha$ the slip normal, both defined in the reference configuration, $\dot{\gamma}^\alpha$ is the plastic slip rate on slip system α and $n_s = 12$ is the number of slip systems in the BCC crystal. The elastic constitutive law is

$$\mathbf{S} = {}^4\mathbf{C} : \mathbf{E}_e, \tag{5.3}$$

where ${}^4\mathbf{C}$ is the fourth-order elasticity tensor, $\mathbf{E}_e = \frac{1}{2}(\mathbf{F}_e^\mathrm{T} \cdot \mathbf{F}_e - \mathbf{I})$ is the elastic Green-Lagrange strain and $\mathbf{S}$ is

$$\mathbf{S} = \mathbf{F}_e^{-1} \cdot \boldsymbol{\tau} \cdot \mathbf{F}_e^{-\mathrm{T}}. \tag{5.4}$$

The plastic slip rate $\dot{\gamma}^\alpha$ is determined via a visco-plastic slip law [39],

$$\dot{\gamma}^\alpha = \dot{\gamma}_0 \left(\frac{|\tau^\alpha|}{\nu^\alpha} \right)^{\frac{1}{m}} \mathrm{sign}(\tau^\alpha), \tag{5.5}$$

where $\dot{\gamma}_0$ is the reference slip rate, m is the strain rate sensitivity parameter, τ^α is the shear stress resolved on the slip system α, and ν^α is the current slip resistance. Schmid's law states that the slip systems with the highest resolved stress are active. However, this law is violated in BCC crystals and thus non-Schmid effects in the BCC phase are incorporated by redefining the resolved shear stress as

$$\tau^\alpha = \left(\mathbf{F}_e^\mathrm{T} \cdot \mathbf{F}_e \cdot \mathbf{S} \right)^\mathrm{T} : \left(\mathbf{P}_0^\alpha + \boldsymbol{\eta}^\alpha \right), \tag{5.6}$$

where $\boldsymbol{\eta}^\alpha$ is defined by [74]

$$\boldsymbol{\eta}^\alpha = \eta_{ss}\vec{s}_0^\alpha \otimes \vec{s}_0^\alpha + \eta_{nn}\vec{n}_0^\alpha \otimes \vec{n}_0^\alpha + \eta_{zz}\vec{z}_0^\alpha \otimes \vec{z}_0^\alpha. \tag{5.7}$$
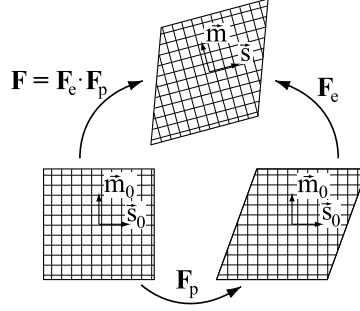
Figure 5.4: Schematic representation of the multiplicative split of the deformation gradient tensor (after [24]).

Here, η_{ss}, η_{nn} and η_{zz} are three non-Schmid parameters and $\vec{z}_0^\alpha = \vec{s}_0^\alpha \times \vec{n}_0^\alpha$. The evolution law of the current slip resistance ν^α is

$$\dot{\nu}^\alpha = \sum_{\beta=1}^{n_s} h^{\alpha\beta} |\dot{\gamma}^\beta|, \tag{5.8}$$

where $h^{\alpha\beta}$ is a hardening matrix taken in the form

$$h^{\alpha\beta} = h_0 \left(1 - \frac{\nu^\alpha}{\nu_\infty}\right)^a q^{\alpha\beta}, \tag{5.9}$$

with $q^{\alpha\beta}$ a matrix with ones on the diagonal and q_n everywhere else (q_n is the ratio of the latent hardening with respect to the self-hardening for non-coplanar slip systems), h_0, ν_∞ and a are material parameters. For BCC steel, only the $\{110\}_{\alpha'}$ slip system family is assumed to be active at room temperature (e.g. [34, 20]).
The material parameters are obtained from literature. First, the anisotropic elastic constants (C_{11}, C_{12} and C_{44}) in the BCC ferrite have been determined based on data in [68], where they were determined from indentation experiments [29]. Next, the initial slip resistance ν_0 of the BCC ferrite has been determined such that macroscopic yielding is predicted at approx. 300 [MPa] for a polycrystal with random orientations (similar to [68]), while the strain rate sensitivity is given by $m = 0.2$ [-] and the reference slip rate by $\dot{\gamma}_0 = 0.01$ [s^{-1}]. The non-Schmid parameters for the BCC phase have been taken from the literature [74]. Finally, the initial hardening rate h_0 and the slip resistance saturation value ν_∞ have been determined while assuming a hardening exponent $a = 1.5$ [-] and a ratio between latent and self hardening $q_n = 1.4$ [-]. The material parameters used in the simulations are listed in Table 5.1.

Table 5.1: Material constants used in the crystal plasticity model.

ν_0 [MPa]	ν_∞ [MPa]	h_0 [MPa]	$\dot{\gamma}_0$ [s^{-1}]	m [-]	a [-]	q_n [-]
65	150	1000	0.01	0.20	1.50	1.40

η_{ss} [-]	η_{nn} [-]	η_{zz} [-]	C_{11} [GPa]	C_{12} [GPa]	C_{44} [GPa]
0.0544	-0.0293	-0.0267	233	135.5	118

5.2.3   Interface cohesive zone model

The PET-steel interface is modeled using a three-dimensional cohesive zone model. The mixed-mode exponential traction-separation law of Van den Bosch et al. [12] is used to model the PET-steel decohesion. The 2D cohesive zone law was discussed in detail in section 3.3.2. The important equations are repeated here. In 3D, the cohesive zone opening vector $\vec{\Delta}$ is split into a contribution normal and tangential to the interface, i.e. $\Delta_t = \vec{\Delta} \cdot \vec{e}_t$ and $\Delta_n = \vec{\Delta} \cdot \vec{e}_n$, respectively. Here, $\vec{e}_n$ is normal to the interface and $\vec{e}_t$ is an in-plane unit vector by projecting $\vec{\Delta}$ on the interface. The traction-separation law in the two directions is defined as

$$T_n\left(\Delta_n, \Delta_t\right) = \frac{\phi_n \Delta_n}{\delta_n^2} \exp\left(-\frac{\Delta_n}{\delta_n}\right) \exp\left(-\frac{\Delta_t^2}{\delta_t^2}\right), \tag{5.10}$$

$$T_t\left(\Delta_n, \Delta_t\right) = 2\frac{\phi_t \Delta_t}{\delta_t^2}\left(1 + \frac{\Delta_n}{\delta_n}\right) \exp\left(-\frac{\Delta_n}{\delta_n}\right) \exp\left(-\frac{\Delta_t^2}{\delta_t^2}\right), \tag{5.11}$$

where Δ is the cohesive zone opening, ϕ is the work of separation and δ is the characteristic opening length. The typical traction-separation response is shown in Fig. 5.5. This is a coupled law, as the maximum reached traction in one direction decreases with prior opening in the other direction. Note that in case of negative normal opening the coupling does not occur to simulate realistic interface closure.

The interface integrity is characterized by the parameter ξ which quantifies the fraction of the work of separation that is not yet dissipated in the cohesive zone element,

$$\xi = 1 - \frac{\Omega}{\phi}, \quad \xi \in [0, 1], \tag{5.12}$$

where Ω is the consumed work of separation in the cohesive zone.
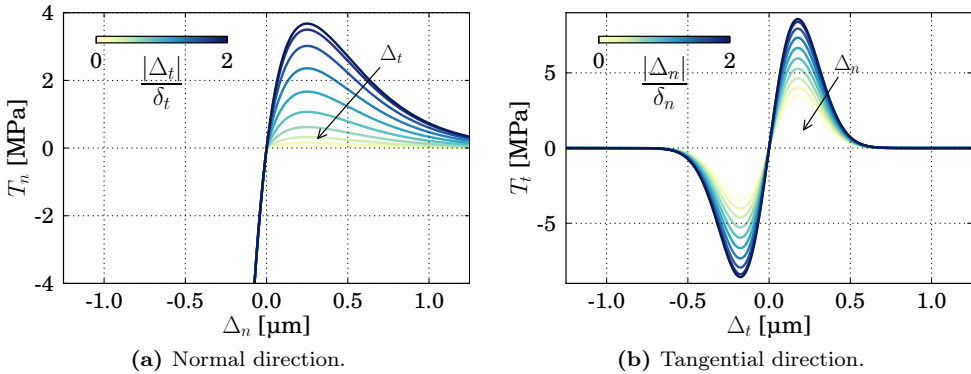
Figure 5.5: The coupled exponential traction-separation law of Van den Bosch et al. [12], using the parameters of Table 5.2.

The cohesive zone parameters (i.e. δ_i and ϕ_i, $i = n, t$) have to be determined from dedicated experiments. However, the parameters may depend on the experiment used to determine them [72]. An example of two experiments of the same material which resulted in different values for the work of separation ϕ is the work of Fedorov et al. [28] and Van den Bosch et al. [15]. The differences arise from the dissipated energy in the process

zone (i.e. the bulk material close to the interface). The simulations presented in this work require parameters that are characteristic for small-scale debonding [25], i.e. close to physical adhesion. Therefore, the results of Fedorov et al. [28] are used here. Using the adopted cohesive zone law, the δ_n and δ_t parameters are estimated on the results in [28]. The resulting parameters are given in Table 5.2. Note that $\phi_n = \phi_t = \phi$ and $\delta_n = \delta_t = \delta$.

Table 5.2: Cohesive zone constants.

ϕ_n [J·m^{-2}]	ϕ_t [J·m^{-2}]	δ_n [µm]	δ_t [µm]
2.5	2.5	0.25	0.25

5.2.4   Polymer constitutive model

The polymer coating investigated here is a 15 [µm] thick PET layer with several additives to improve adhesion [15]. PET is a glassy polymer and almost fully amorphous (crystallinity is approx. 8%). The typical intrinsic response of glassy polymers is shown in Fig. 5.6(a) for a uniaxial compression test. Initially, the response is nearly linear elastic (1), followed by non-linear visco-elasticity (2) up to yielding (3). Softening occurs directly after yielding depending on the age of the polymer (4). Finally, softening is overtaken by strain hardening at large strains (5). The yield point depends on the applied strain rate [17].

The model employed here to predict this complex mechanical behavior is the so-called "Eindhoven Glassy Polymer" (EGP) model. This model was shown to accurately capture the behavior of glassy polymers [17, 41]. While the EGP model is a multi-mode, multi-process constitutive model, here only one mode and one process are considered as only a limited set of PET parameters is known. The mechanical analogue of the single-mode, single-process EGP model is shown in Fig. 5.6(b) and detailed below.
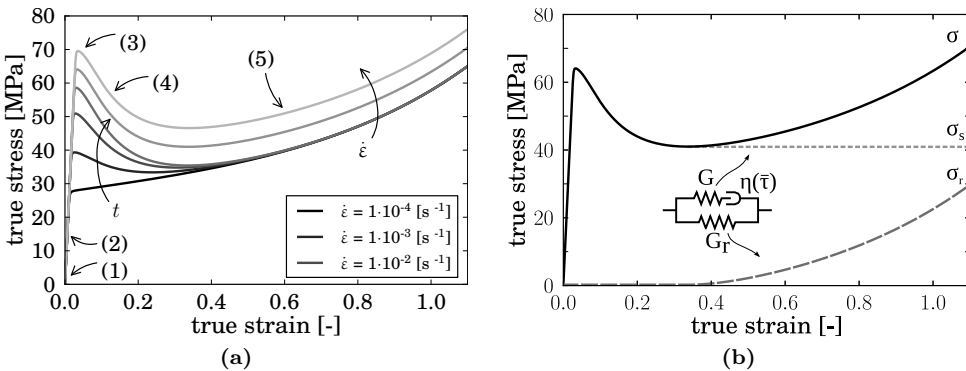

Figure 5.6: (a) Typical response of glassy polymers; the numbers indicate different responses: (1) linear elastic; (2) non-linear visco-elastic; (3) yield point; (4) strain softening; and (5) strain hardening; (b) Mechanical analogue of the SM-SP (single-mode, single-process) EGP model used (after [17]).

The total stress is separated into two contributions, i.e. a driving stress $\boldsymbol{\sigma}_s$ and a hardening stress $\boldsymbol{\sigma}_r$ (see also Fig. 5.6(b)),

$$\boldsymbol{\sigma} = \boldsymbol{\sigma}_s + \boldsymbol{\sigma}_r. \tag{5.13}$$

Hardening originates from the oriented entangled network and is modeled by a neo-Hookean relation,

$$\boldsymbol{\sigma}_r = G_r \tilde{\mathbf{B}}^d, \tag{5.14}$$

where G_r is the strain hardening modulus and $\tilde{\mathbf{B}}^d$ the deviatoric part of the isochoric left Cauchy-Green deformation (Finger) tensor. The intermolecular interactions are modeled via the driving stress,

$$\boldsymbol{\sigma}_s = \boldsymbol{\sigma}_s^h + \boldsymbol{\sigma}_s^d = \kappa(J-1)\mathbf{I} + G\tilde{\mathbf{B}}_e^d. \tag{5.15}$$

Here, $\boldsymbol{\sigma}_s^h$ and $\boldsymbol{\sigma}_s^d$ are the hydrostatic and deviatoric stresses, respectively, κ is the bulk modulus, J is the volume change ratio, $\mathbf{I}$ is the second-order unity tensor, G is the shear modulus and $\tilde{\mathbf{B}}_e^d$ is the deviatoric part of the elastic isochoric Finger tensor. The kinematic evolution of J and $\tilde{\mathbf{B}}_e^d$ is given by

$$\dot{J} = J\mathrm{tr}(\mathbf{D}), \tag{5.16}$$

$$\dot{\tilde{\mathbf{B}}}_e = (\tilde{\mathbf{L}} - \mathbf{D}_p) \cdot \tilde{\mathbf{B}}_e + \tilde{\mathbf{B}}_e \cdot (\tilde{\mathbf{L}}^{\mathrm{T}} - \mathbf{D}_p). \tag{5.17}$$

Here $\tilde{\mathbf{L}}$ is the isochoric velocity gradient tensor and $\mathbf{D}$ the deformation rate tensor and $\mathbf{D}_p$ is the plastic deformation rate tensor, which is coupled to $\boldsymbol{\sigma}_s^d$ via a non-Newtonian flow rule,

$$\mathbf{D}_p = \frac{\boldsymbol{\sigma}_s^d}{2\eta}, \tag{5.18}$$

with viscosity η

$$\eta = \eta_{0,ref} \frac{\tau_{eq}/\tau_0}{\sinh(\tau_{eq}/\tau_0)} \exp\left(\frac{\mu p}{\tau_0}\right) \exp(S), \tag{5.19}$$

where $\eta_{0,ref}$ is the reference zero-viscosity, τ_0 is the characteristic equivalent stress and μ captures the pressure dependency. The total equivalent stress, τ_{eq} and the pressure, p, are defined as

$$\tau_{eq} = \sqrt{\tfrac{1}{2}\boldsymbol{\sigma}_s^d : \boldsymbol{\sigma}_s^d}, \tag{5.20}$$

$$p = -\tfrac{1}{3}\mathrm{tr}(\boldsymbol{\sigma}). \tag{5.21}$$

The thermodynamic state parameter S typically depends on the equivalent plastic strain $\varepsilon_{p,eq}$ [17]. However, the research presented in chapter 3 revealed a dependency of the interface damage on the initial thermodynamic state of the polymer coating, i.e. the dependence on the initial value of S. Deformation-induced interface roughening was investigated in a two-dimensional numerical-experimental framework. The simulations predicted that a rejuvenated coating shows noticeably less interface damage compared to an aged coating. The change in steel surface profile triggers localization in an aged coating, which results in interface damage. The localization is significantly less for a rejuvenated coating resulting in less damage. Here it is assumed that the polymer has been rejuvenated (i.e. $S = 0$ [-]) prior to can manufacturing, e.g. via a pre-conditioning treatment such as presented in chapter 4. The material parameters for the PET coating are listed in Table 5.3 and the corresponding mechanical response is shown in Fig. 5.6(a).

Table 5.3: Material properties of PET for the EGP model.

G_r [MPa]	κ [MPa]	G [MPa]	$\eta_{0,ref}$ [MPa·s]	τ_0 [MPa]	μ [-]
4.7	1800	812	$3 \cdot 10^8$	1.262	4.8

5.2.5   Computational model

The modeled domain (see Fig. 5.2(a)) is discretized using three-dimensional linear cube elements to create a regular finite element grid, similar to [55], which results in non-conforming grain boundaries. Another possible discretization relies on using tetrahedral elements (similar to e.g. [45, 75]), which accommodate conforming grain boundaries. However, this requires a large number of elements, which drastically increases the computational cost. The adopted finite element discretization is shown in Fig. 5.7.

The dominant Euler angles and their respective fractions are extracted from the EBSD measurement shown in Fig. 5.2(b) using the methodology proposed by Jöchen & Böhlke [40]. The representative Euler space (the rotation angles ϕ_1, Φ, ϕ_2) is divided into 432 (24 ϕ_1, 3 Φ and 6 ϕ_2 divisions) boxes within which the average Euler angle and fraction is calculated. This results in a set of 333 unique Euler angles with their associated volume fractions. Using this reduced set of Euler angles and fractions, the experimental Orientation Distribution Function (ODF) is approximated within a 5% error of the L2 norm.

As the subsurface crystallographic steel microstructure is not readily available, a Voronoi tessellation is used to generate realistic grain geometries. The Voronoi tessellation is performed using the *Neper* software package [53]. The average grain size is taken from the EBSD measurement and equals 10 [µm]. Within the modeled domain, 200 grains are generated for the steel substrate using an equi-axed, in-plane periodic tessellation. An example of one of the tessellations is shown in Figure 5.7.
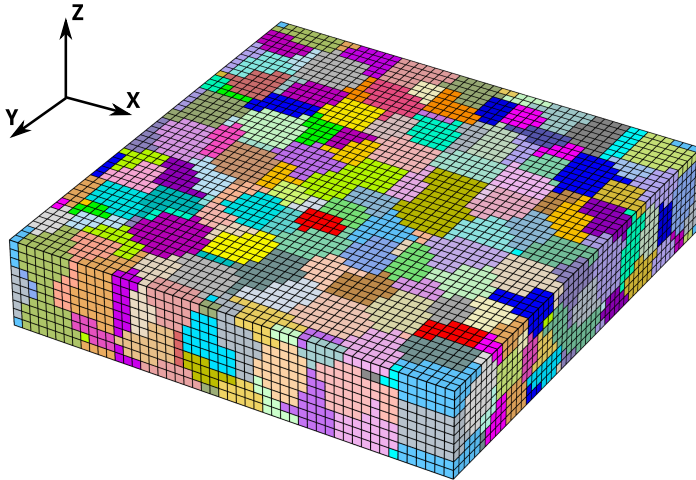

Figure 5.7: Example of a Voronoi tessellation and the finite element discretization used in the tension and compression simulations; colors only serve to distinguish the respective grains.

5.3   Results

5.3.1   Deformation-induced roughening

Four tensile simulations were performed along the x-direction of the material using differ-
ent tessellations and Euler angles. The resulting height profiles for the tessellation shown
in Fig. 5.7 at an average linear strain of $\varepsilon = 7.5\%$ and $\varepsilon = 15\%$ are shown in Fig. 5.8(a)
and (b), respectively. The results show the formation of hills and valleys on the steel sur-
face. The roughness pattern grows in amplitude with increasing deformation, but reveals
the same qualitative behavior. The size of the roughness features varies and depends on
the size of the grains.

The root-mean-square (RMS) roughness value of the resulting height profile of the four
simulations is compared to experimentally obtained values presented in chapter 3. The
RMS value is defined as

$$\text{RMS} = \sqrt{\langle u_z(\vec{x})^2 \rangle}, \tag{5.22}$$

where $\langle \dots \rangle$ indicates the spatial average of the top steel surface. The evolution of the
RMS value (with thick lines to indicate the minimum and maximum) for the different
simulations, together with the experimental result, as a function of the applied average
strain is shown in Fig. 5.9. Note that this strain is a global measure, i.e. the applied
linear strain in the simulation and the measured linear strain in the field of view of the
experiments.

The results show that varying the grain geometry and orientations affects the predicted
roughness amplitude and roughening rate ($\frac{\partial \text{RMS}}{\partial \varepsilon}$), leading to a spread in the predicted
RMS values. The microstructure clearly influences the predicted roughness. Comparing
the two curves shows that the experimental RMS values coincide with the lower bound
predicted by the simulations. Note that only a single experiment is shown and that a
similar spread may exist in the experiments. Both the experiment and the simulations
predict an almost linear increase in the RMS value as a function of the strain.

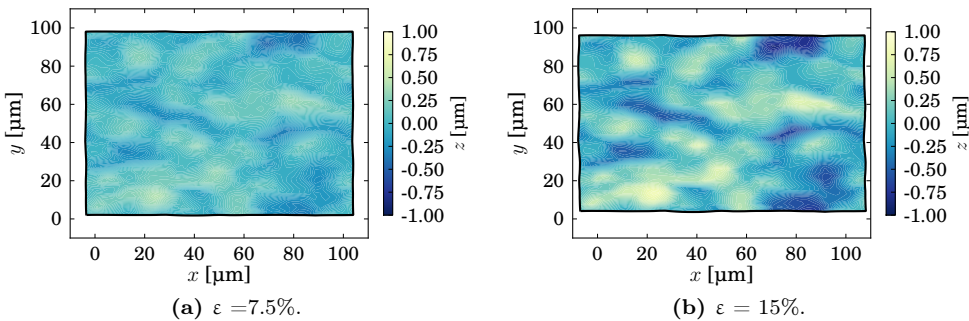(a) $\varepsilon = 7.5\%$.   (b) $\varepsilon = 15\%$.

Figure 5.8: Surface roughness at different strains in a tensile simulation of a polymer-
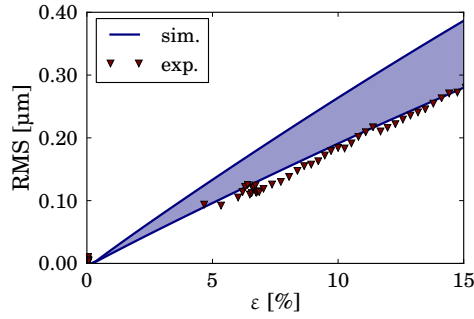coated steel; the microstructure is shown in Fig. 5.7.

Figure 5.9: Evolution of the RMS values predicted in four tensile simulations for different underlying steel microstructures; the thick lines correspond to the lower and upper bound of the simulations.

5.3.2 Interface integrity

The interface integrity (ξ, see Eq. (5.12)) at $\varepsilon = 7.5\%$ and $\varepsilon = 15\%$ for the tensile simulation is shown in Fig. 5.10. At a strain of $\varepsilon = 7.5\%$ the interface is still almost fully intact. However, at $\varepsilon = 15\%$, damage has clearly initiated locally, see Fig. 5.10(b). This is visible in the localized regions where the interface integrity tends towards zero. The evolution of the average interface integrity $\langle\xi\rangle$ in the four simulations is shown in Fig. 5.11(a) and the minimum integrity ξ_{min} is shown in Fig. 5.11(b). The average interface integrity remains relatively high for all simulations, even at a strain of $\varepsilon = 15\%$. Clearly, the interface fails locally as is visible in the rapid decay towards zero of the minimum value.

(a) $\varepsilon = 7.5\%$.　　　　　　　　　　**(b)** $\varepsilon = 15\%$.
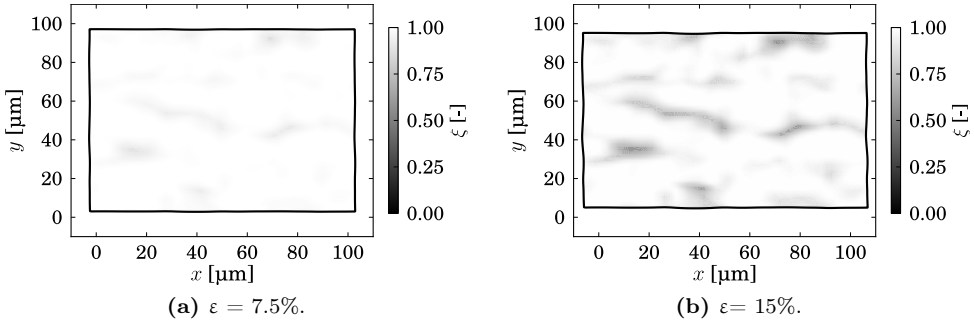
Figure 5.10: Interface integrity ξ at different strains in a tensile simulation of a polymer-coated steel; the microstructure is shown in Fig. 5.7.

The correlation between the roughness profile in Fig. 5.8(b) and the interface integrity in Fig. 5.10(b) is investigated next. To this end, the local deformations at the interface are decomposed in three characteristic scalar (but position dependent) quantities: (a) the positive out-of-plane displacement field which forms hills (Eq. (5.23)); (b) the absolute out-of-plane displacement field that forms valleys (Eq. (5.24)); and (c) the local in-plane displacement field (Eq. (5.25)).

(a) average. **(b)** minimum.

Figure 5.11: The average and minimum interface integrity for four tensile simulations of a polymer-coated steel; the thick lines correspond to the lower and upper bound of the simulations.

$$u_{\text{hill}} = \tfrac{1}{2}\left(u_z + |u_z|\right) \tag{5.23}$$

$$u_{\text{valley}} = \tfrac{1}{2}|\left(u_z - |u_z|\right)| \tag{5.24}$$

$$u_{\text{in-plane}} = \sqrt{(u_x - u_{x,\varepsilon})^2 + (u_y - u_{y,\varepsilon})^2} \tag{5.25}$$
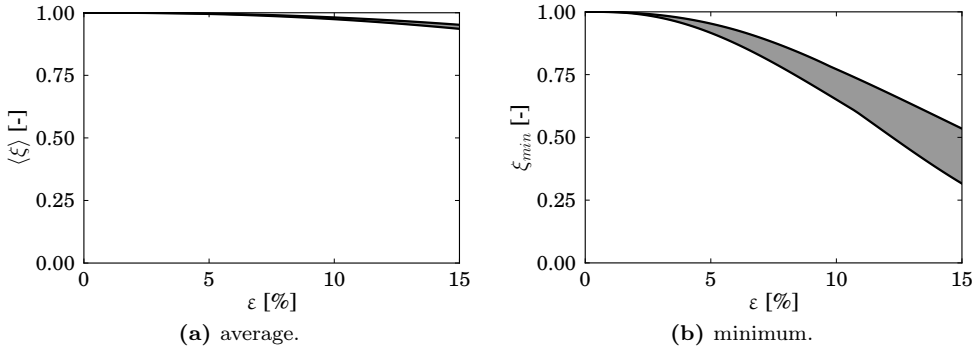
Note that in Eq. (5.25), the average surface strain due to the applied tension ($u_{i,\varepsilon}$, $i = x, y$) is removed via linear regression. These displacement fields are normalized and multiplied by the loss in the interface integrity (i.e. $1 - \xi$) yielding the correlation factor χ

$$\chi = \hat{u}\left(1 - \xi\right). \tag{5.26}$$

Here, $\hat{u}$ is the normalized displacement field for each of the individual measures of Eqs. (5.23)-(5.25). Thus only a large displacement combined with a low interface integrity results in $\chi \gg 0$. The result of the correlation analysis is shown in Fig. 5.12. The correlation factor of the positive out-of-plane displacement field and the interface integrity (Fig. 5.12(a)) shows that no clear correlation exists between the formation of a hill on the steel surface and the interface integrity. This is explained by the fact that the formation of a hill is accompanied by interface closure in the interface normal direction. The correlation factor for the formation of a valley (Fig. 5.12(b)) and the factor for the in-plane displacement field (Fig. 5.12(c)) show high values in several locations. Furthermore, the formation of valleys or the in-plane displacement field alone cannot describe the interface damage, see the arrows in Figs. 5.12(b) and 5.12(c). Clearly, the formation of valleys together with the in-plane displacement field determines the resulting interface integrity profile.
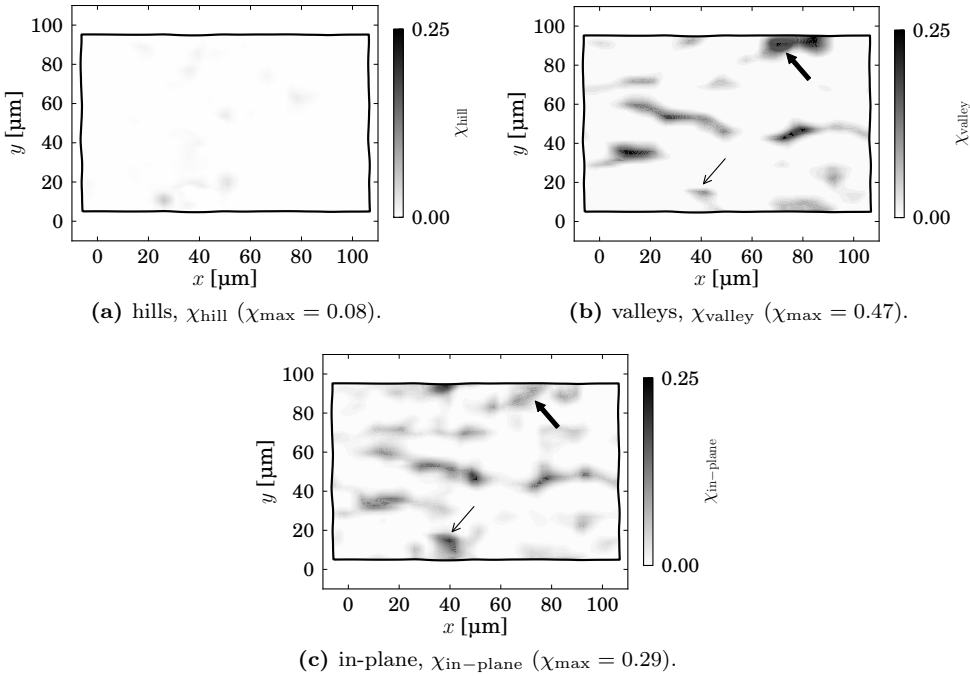
(a) hills, χ_{hill} ($\chi_{\mathrm{max}} = 0.08$).

(b) valleys, χ_{valley} ($\chi_{\mathrm{max}} = 0.47$).

(c) in-plane, $\chi_{\mathrm{in-plane}}$ ($\chi_{\mathrm{max}} = 0.29$).

Figure 5.12: Correlation (χ) between the normalized displacement field ($\hat{u}$) and the loss of interface integrity ($1 - \xi$) for three different displacement measures in the tension simulation shown in Figs. 5.8(b) and 5.10(b); arrows indicate differences between χ_{valley} and $\chi_{\mathrm{in-plane}}$; note that the colorbar was adjusted for clarity (the maximum for each measure is indicated in the respective captions).

5.3.3 Tension-compression comparison

Tension and compression simulations are next compared to study the interface integrity for different loading conditions. The roughness profile predicted for a uniaxial compression simulation at $\varepsilon = $ -15% is shown in Fig. 5.13(a) for the steel crystallography in Fig. 5.7. The tension results were presented earlier in Figs. 5.8 and 5.10. Comparing the roughness patterns predicted in tension (Fig. 5.8(b), repeated in Fig. 5.14(a)) and compression shows clear differences. Apparently, different hills and valleys form on the steel surface due to the applied deformation. However, a clear relation exists between the valleys that form in compression and the hills that form in tension, and vice versa. This is obvious from Fig. 5.14 where the roughness profile in compression was inverted for clarity (Fig. 5.14(b)). The two roughness profiles qualitatively match in terms of the predicted surface heights. However, the in-plane deformations are different due to the prescribed compression and tension. Clearly, the slip activity on the active slip systems in the crystal plasticity model are reversed in compression, resulting in a nearly inverse roughness profile. Fig. 5.15 shows the evolution of the extreme values of the RMS roughness value for four tension and four compression simulations. The results show that, in compression, the average slope of the RMS value increases compared to tension. In compression, the steel surface material extrudes out of the surface to accommodate compression, while in tension, the

surface is stretched, reducing the roughness pattern.

The interface integrity at a strain of ε = -15% is shown in Fig. 5.13(b). Similar to the predicted roughness profiles, a difference is visible in the predicted integrity patterns. Different locations of the PET-steel interface initiate damage. Similar to the result in tension, the correlation analysis showed that a correlation emerges between the in-plane and negative out-of-plane displacement fields and the predicted interface damage. The evolution of the extremes of the average and minimum interface integrity as a function of the applied strain is depicted in Figs. 5.16(a) and 5.16(b), respectively. The average integrity again remains relatively high, indicating that interface failure occurs locally. The interface damages faster in compression as a result of the increased roughening rate. Furthermore, the minimum interface integrity decays more rapidly towards zero in compression than in tension. Obviously, uniaxial compression results in an increase in the predicted interface damage compared to uniaxial tension.

(a) roughness.   **(b)** integrity.
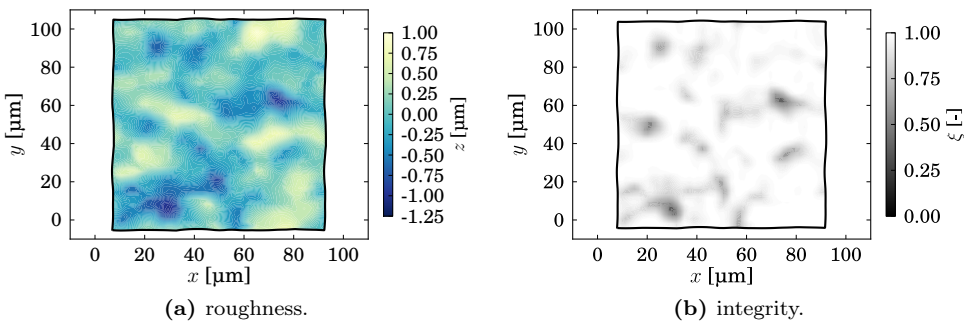
Figure 5.13: (a) Surface roughness and (b) interface integrity for a compression simulation at ε = -15%; the used tessellation and grain orientations are identical to the tension simulation in Fig. 5.8.

(a)   **(b)**

Figure 5.14: (a) Surface roughness profile for a tension simulation at ε = 15% (identical to Fig. 5.8(b)), and (b) the inv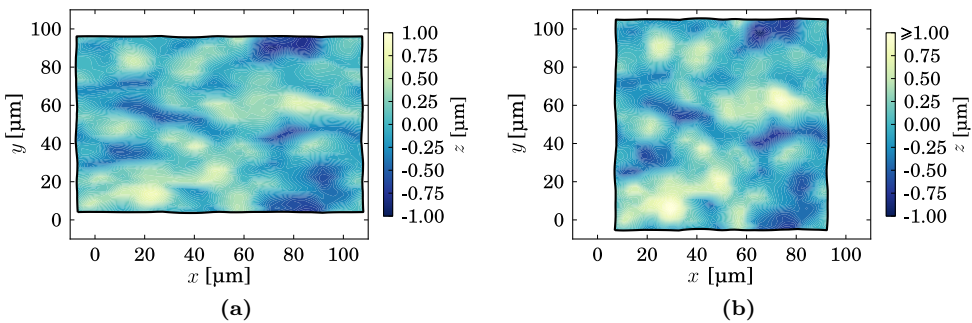erted roughness profile for a compression simulation at ε = -15%; the used tessellation and grain orientations are consistent with the tension simulation.
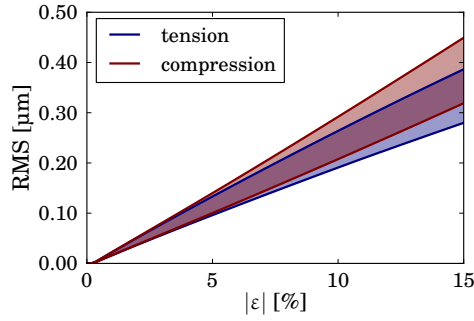
Figure 5.15: Evolution of the RMS values as a function of the applied strain for four simulations in tension and compression; the thick lines correspond to the lower and upper bound of the simulations.
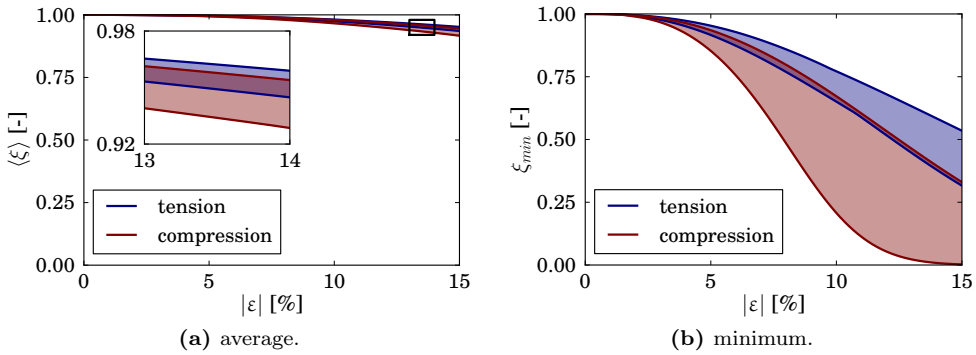

(a) average.

(b) minimum.

Figure 5.16: Evolution of the average and minimum interface integrity as a function of the applied strain for four simulations of uniaxial tension and compression; the thick lines correspond to the lower and upper bound of the simulations.

5.4   Discussion

The presented numerical framework enables prediction of deformation-induced roughening of a steel substrate and the effect thereof on the polymer-steel interface integrity. The simulations predict the initiation and growth of interface damage, whereby the tensile results qualitatively match experimental results. Furthermore, a comparison between uniaxial tension and compression shows that in compression, the roughening rate is increased with an increase in predicted interface failure as a result.

The continuum assumption within the crystal plasticity model limits the simulated height profile evolution to continuum phenomena occurring at the grain-scale or above. The effect of micro-scale events, e.g. the formation of crystallographic slip steps is not predicted in the current framework. Recent results of Faber et al. [25] showed that during production, the polymer-steel interface may locally delaminate due to micro-scale roughening. Clearly, incorporating the micro-scale roughening phenomena into the presented framework poses a great challenge.

While discrete slip events occurring at the free surface are not incorporated in a crystal plasticity approach, the slip activity on the different BCC slip planes is still predicted in

an average sense. The average slip activity may serve as an indicator for discrete surface events. Micro-scale slip steps can be assessed via a different numerical simulation (e.g. Discrete Dislocation Dynamics) on the basis of the predicted slip activities found here.

To incorporate the roughening events near grain boundaries, e.g. due to dislocation pile-ups, a strain gradient crystal plasticity approach can be considered. Borg & Fleck [11] studied roughening near a grain boundary of a bi-crystal of FCC aluminium and found that the predicted roughness profile depends on the internal length scale. Nygårds & Gudmundson [49] also studied roughening using a strain gradient crystal plasticity model. Their simulations revealed a strong dependence of the predicted roughness on the internal length scale. However, these results were not yet compared to experiments, and are therefore still limited to interpretations.

It is also possible to incorporate the misorientations inside the steel grains into the grain orientations. Currently, all material points inside the modeled steel grains have an identical grain orientation. The effect of internal grain misorientations was investigated by Cheong & Busso [21]. Their simulations showed that including the local misorientations into the crystal plasticity simulations may change the local strain distribution and thus also the predicted roughness.

The comparison with experiments presented in this work is limited to a qualitative match in terms of the average roughness evolution. The simulations were compared to a single tensile experiment performed on a packaging steel. To quantitatively predict deformation-induced roughening, experiments have to be compared to simulations using the same grain orientation and geometry. An example of such a comparison is the work of Zhao et al. [75] and Lim et al. [45], who compared the experiments and simulations on aluminium oligocrystals. Their results suggest that the predictions compare well to the experiments. Quantitative predictions of the roughness evolution are feasible by incorporating the complete measured steel crystallography in the presented framework.

In the presented results, the steel thickness was set to 20 [µm]. The influence of the modeled steel thickness was analyzed by studying the evolution of the extremes of the RMS values as a function of the average applied strain for four simulations of a polymer-coated steel with a steel thickness of 20 [µm] and 30 [µm], the results of which are shown in Fig. 5.17. On average, the predicted roughness in the simulations with a steel thickness of 30 [µm] is smaller compared to the simulations with a steel thickness of 20 [µm] and the variation between the simulations decreases. Thus, increasing the steel thickness may improve the experimental match further. Clearly, to accurately predict the steel roughness evolution, a sufficient amount of grains must be considered.

Finally, the adopted finite element discretization is relatively coarse due to the high computational cost of the simulation, limiting the amount of bending that can be applied. A tensile simulation was performed on a modeled steel block of 40 × 40 × 20 [µm] using a coarse and fine discretization and the resulting roughness profile was studied. The results are shown in Fig. 5.18. The roughness amplitude increases with mesh refinement (see Fig. 5.18(c)) and may thus affect the experimental comparison. However, the predicted roughness patterns remain qualitatively the same, see Fig. 5.18(a) and 5.18(b), indicating that the predicted interface integrity patterns are not affected by mesh refinement. However, the initiation of interface damage will occur at a lower strain.
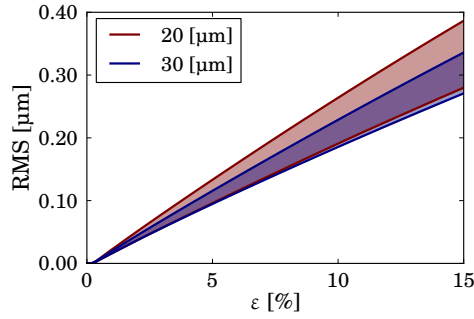
Figure 5.17: Evolution of the minimum and maximum RMS values for four simulations using a steel thickness of 20 [µm] and 30 [µm] and different steel microstructures; the thick lines correspond to the lower and upper bound of the simulations.

(a) roughness, 4.000 elements.

(b) roughness, 32.000 elements.

(c) RMS
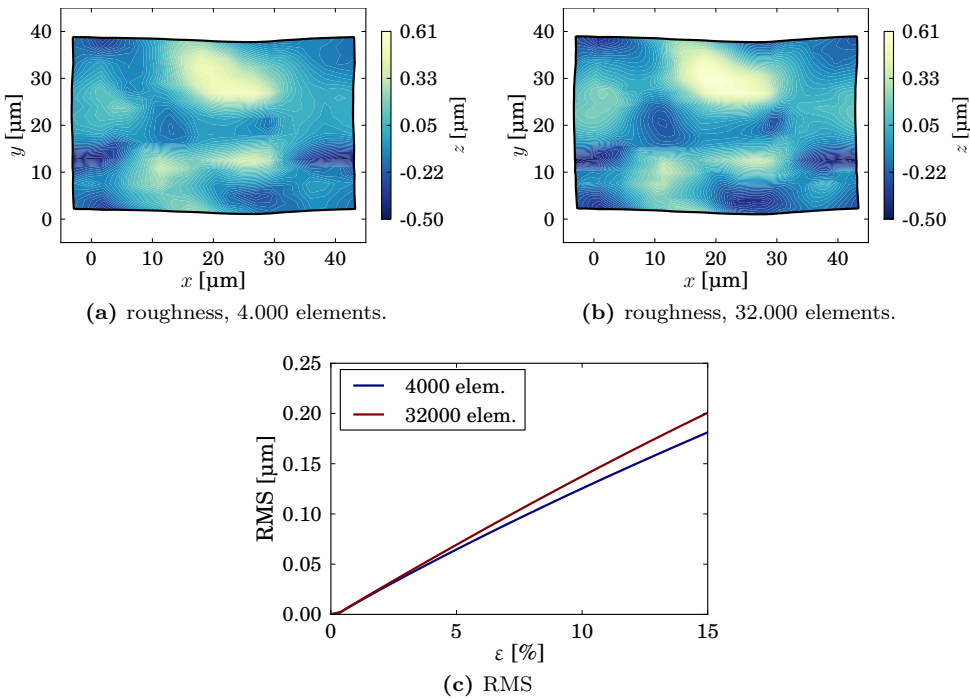
Figure 5.18: (a) and (b) roughness profiles at $\varepsilon = 15\%$ for two different finite element discretizations; and (c) the corresponding evolution of the RMS roughness value.

5.5 Conclusion

A three-dimensional numerical framework for the prediction of deformation-induced interface roughening and interface failure was presented. The framework was applied to a polymer-coated packaging steel. Simulations of uniaxial tension and compression were performed for different steel grain geometries and orientations. Some conclusions are drawn from the analysis.

- The predicted roughness evolution in tension qualitatively agrees with tensile experiments performed on a packaging steel. Furthermore, the simulations predicted the initiation and growth of local interface failure.

- Compared to tension, compression simulations showed an increased roughening rate with an increase in the predicted interface damage as a result.

- The developed framework enables study of the local initiation and growth of interface damage during deformation-induced roughening of a polymer-coated steel.

The incorporation of a predictive steel model, i.e. crystal plasticity, complements the cumbersome measurements of detailed experimental displacement fields that accompany deformation-induced roughening and thus enables the analysis of deformation processes where measuring the steel surface profile is difficult if not impossible, e.g. industrial forming processes such as deep drawing. The framework may be extended to simulate industrial forming conditions, e.g. repeated deep (re-) drawing and wall ironing, to investigate the interface integrity during forming. Due to the computational cost of the simulations, this may be accomplished by incorporating the framework into a global-local approach, e.g. by embedding the modeled domain into a bulk simulation or via a multi-scale approach.

6

CONCLUSIONS AND OUTLOOK

6.1 Conclusions

Deformation-induced roughening is a problematic phenomenon in pre-coated metals. A prime example of an application where this change in roughness is detrimental is polymer-coated steel used in the production of, for example, food and beverage packaging. To significantly reduce the environmental impact of the production process, the steel is pre-coated with a PET layer. However, during production, the polymer-coated steel is subjected to severe loading conditions which result in drastic changes of the steel surface profile and consequently in local interface failure. The application demands that no visible or even invisible damage is present after production and during the prolonged shelf-life of the product.

This thesis aimed to investigate the effect of the change in steel surface roughness during applied deformation on the polymer-steel interface integrity using a numerical-experimental approach. Experimental observations of steel roughening have been incorporated in numerical simulations to study and predict the polymer-steel interface.

First, a novel methodology for extracting three-dimensional full-field displacement fields (in-plane and out-of-plane) from measured surface height profiles was developed to investigate the deformation fields that accompany the steel surface roughening. The developed Digital Image Correlation technique provides quantitative information of various surface deformation phenomena, and thus outperforms traditional methods of evaluating a surface height profile based on average height values. However, the method is only applicable if a) an initial surface profile is present, and b) the height changes between height profiles are small. To guarantee that the second demand was met, an incremental measurement technique was adopted. The method was verified using well-defined displacement fields. Furthermore, the method was applied to sequential in-situ height profiles measured on a packaging steel deformed in a uniaxial tensile test. The extracted displacements revealed the formation and growth of hills and valleys on the steel surface.

The displacement fields were used in a numerical simulation of a polymer coating and a polymer-steel interface layer to study the interface integrity during deformation-induced steel roughening. The displacements served as a boundary condition which was applied to the bottom of the interface layer. This eliminates the necessity of modeling the steel substrate as it was assumed that the steel dictates the deformation of the polymer coating and not vice versa. Simulations with an aged PET coating revealed the initiation and growth of localization bands in the coating. The interface near these bands delam-

inates due to the intensified stress and strain within the bands. Variation of the initial polymer age (i.e. the thermodynamic state) from a rejuvenated to an aged state showed that the predicted interface damage is significantly less for a rejuvenated coating, since the post-yield softening behavior which triggers localization is removed by rejuvenation. Furthermore, the study revealed that an optimum exists in the polymer age which delays the initiation of interface damage to a maximum applied strain.

However, after coating the steel substrate and prior to can production, the coated material is typically stored for extended periods of time. During this time, the coating continuously ages. Hence, during production the polymer is typically far from the optimum age identified in the simulations. Mechanically rejuvenating the material via rolling prior to manufacturing was explored to recover the optimum polymer age before production. Rolling simulations were performed on a polymer-coated packaging steel and the influence of the rolling reduction on the average thermodynamic state directly after rolling was studied. The simulations showed that the final polymer state can be tailored via rolling. Furthermore, the developing interface stresses were investigated and an optimum in the friction coefficient was identified which reduces the stress magnitude to a minimum. Assuming that the stress is sufficiently low, rolling may be used to obtain the desired polymer age prior to production to delay or even prevent the formation of interface damage in subsequent forming processes.

The results thus far were based on uniaxial tensile tests performed on a packaging steel. However, during production, the polymer-coated steel is subjected to industrial forming processes, e.g. deep (re-)drawing and wall ironing. During these processes, in-situ observation of the steel surface is typically not possible as the material is fully obscured by the dies during deep drawing. To enable study of deformation-induced interface roughening in these processes, a numerical framework was developed which incorporates a crystal plasticity constitutive model to predict the change in the steel surface roughness. A steel substrate with a polymer coating and interface layer was modeled and deformed in tension and compression. Due to the anisotropy of the steel grains (captured in the crystal plasticity model), the deformation results in a change in surface roughness of the steel. Comparing the predicted root-mean-square average roughness with experimental observations showed a qualitative agreement. Furthermore, due to the change in steel surface roughness, interface failure was initiated and further promoted by increasing deformation. Finally, tension and compression simulations were compared and it was shown that the steel surface roughness increases faster with increasing strain in compression compared to tension, which increases the predicted interface damage as a result.

With the developed methodologies presented in this thesis, new insights were gained in the effects of deformation-induced roughening on the integrity of a polymer-steel interface. The framework presented within this thesis enables a further study of the required processing and storage conditions in industrial applications, where these polymer-coated steels are used.

6.2   Outlook

Although new insight was gained in the effects of deformation-induced interface roughening on the interface integrity during deformation of a polymer-coated steel, some aspects remain open for further investigation.

6.2.1 Interface parameter identification

The developed numerical framework uses cohesive zones to simulate the polymer-steel decohesion. Material parameters for the adopted exponential cohesive zone law are not readily available. This obviously limits the applicability of the results presented in this thesis since they are qualitative only. While parameters from literature were used in the presented work, quantitative predictions of the interface integrity during deep drawing and other industrial forming processes require experimental determination of the interface parameters.

It was previously shown that characterizing the interface parameters is challenging since different experiments yield different values. For example, the work of Fedorov et al. [28] on laser-induced delamination determined the work-of-separation as $\phi = 2.5$ [J·m^{-2}]. However, the work of Van den Bosch et al. [15], who performed peel-off experiments, reported $\phi = 194.5$ [J·m^{-2}]. The difference between these results is explained by the distinct energy dissipated inside the process zone, i.e. the material close to the interface [72]. It is therefore necessary to determine the interface parameters characteristic for the phenomena investigated, i.e. small-scale interface debonding due to deformation-induced roughening, using a representative experimental technique.

Recently, local damage events in a polymer-coated steel were investigated experimentally by Faber et al. [25]. Cross-sections of produced cans were explored using Focused Ion Beam milling. The experiments revealed local interface delamination after can production, see also Fig. 3.20. While these experiments show that the interface indeed damages during production, they do not allow to track the evolution of the steel surface roughness nor the initiation and growth of the damage events. Expanding this experimental methodology to study the polymer-steel interface during deformation may provide a suitable method to determine the required interface parameters.

6.2.2 Micro-scale roughening

A polycrystalline metal roughens over a wide range of scales, ranging from the nano-scale to the size of multiple grains. The work presented in this thesis has focused on the effect of the grain-scale roughening and above, see also Fig. 2.2, due to limitations imposed by the experimental measurement technique, i.c. optical surface height profilometry, and the used constitutive model for the steel substrate, i.c. crystal plasticity.

Recent experimental observations of Faber et al. [25, 26] revealed that sub-grain deformation-induced roughening may also play a role in the initiation and growth of interface damage. The formation of slip steps on the steel surface were shown to initiate damage in a brittle PET coating due to the high local strain. The presented framework can be extended to incorporate these events to gain quantitative insight into the effects of micro-scale roughening. This may be accomplished through experiments and/or by extending the numerical approach towards smaller length scales.

Experimental

Within this thesis, confocal optical height profilometry was used to study deformation-induced steel roughening of an uncoated packaging steel deformed in tension. The measured height profiles were used in a Finite Element based Digital Image Correlation (FE-DIC) technique to extract the three-dimensional surface displacements of the steel. The verification analysis of the FE-DIC method, presented in section 2.3, showed that a suffi-

cient amount of pixels per degree-of-freedom in the finite element discretization is required to accurately predict the displacement fields. This limits the element size of the finite element discretization to approximately 450 pixels per triangular element. Due to the optical spatial resolution limits of the used confocal profiler, only grain-scale and super-grain-scale roughening events were resolved in the calculation (see also Fig. 2.12). To incorporate the nano- and micro-scale events into the developed numerical-experimental method, a different height measurement technique may be explored.

A possibility is to apply a non-optical measurement technique to measure the evolution of the steel surface profile, e.g. AFM or a 3D SEM reconstruction methodology (e.g. the work of Faber et al. [27]). These methods provide a higher spatial resolution than the optical height profiler used in this thesis and thus provide more information on (part of) the sub-grain roughening phenomena.

Numerical

As discussed, the continuum crystal plasticity constitutive model does not take into account small-scale discrete roughening events, e.g. slip steps forming on the steel surface. To incorporate these nano- and micro-scale events, the numerical framework can be extended. While discrete changes in surface roughness cannot be captured by a continuum description, other modeling approaches can be employed to incorporate smaller length scales. For example, Discrete Dislocation Dynamics [32] can be employed to track to motion of individual dislocations and thus allows to study the effects of the small-scale discrete events.

Furthermore, local variations in steel or interface properties may provide an alternative route to explore the sub-grain roughening phenomena without modeling them explicitly. For example, by statistically varying the interface parameters, the interface can be locally weakened to simulate the reduction in work-of-separation. The variations have to be based on experimental observations of the micro-scale features which form during roughening. Another possibility is the generation of well-defined displacement fields that can be superimposed onto the measured experimental surface displacement fields. These fields have to be characteristic for the investigated roughening phenomena. Finally, the steel grain properties and orientations can locally be varied to incorporate the effect of local misorientations, similar to the work of Cheong and Busso [21].

6.2.3   Prolonged shelf-life

This thesis focused primarily on predicting the interface integrity during the change in surface roughness, i.e. instantaneous damage during deformation. The results presented in this thesis show that the deformation-induced steel roughening is accompanied by highly heterogeneous surface displacements. This heterogeneous displacement field results in the formation of localization bands in the polymer coating which may lead to local interface failure (see also Fig. 3.14).

The mechanical and physical behavior of the PET coating is dominated by time dependent processes which may influence the long-term interface integrity of the products after manufacturing. For example,

(a) continuous physical aging of the polymer is accompanied by a yield stress variation and volume change [58];

(b) while crystallization of the amorphous regions of the semi-crystalline PET is suppressed to a certain degree during production due to the imposed pressures on the coating [76], after production and if the temperature is raised above the glass transition temperature of the PET coating (e.g. during product sterilization [10]), the internal stress and strain result in (additional) crystallization [33], which is also accompanied by a volume change [7]; and

(c) stress relaxation redistributes the stresses to reduce the localization ([42]).

Clearly, these processes change the internal structure of the polymer which may influence the interface integrity. Furthermore, the time-dependency of the polymer-steel adhesion may become apparent during shelf-life. The interface time dependency can be incorporated into the presented framework by extending the traction-separation law to include the effects of time, e.g. the law proposed by Allen & Searcy [3]. Obviously, studying the effect of time on the interface integrity during the prolonged shelf-life is an interesting topic to explore further.

6.2.4 Towards industrial processes

In chapter 5, a numerical framework was developed which incorporates a crystal plasticity model for the steel substrate to enable prediction of deformation-induced roughening in deformation processes other than uniaxial tension. The framework was first applied to a tension simulation of a polymer-coated steel to qualitatively compare the predictions of the model to the experimental measurements. Furthermore, the differences in predicted interface roughness and integrity in tension and compression have been investigated.

A logical next step is to investigate more complex deformation states typically encountered in forming processes, e.g. bending, confined tension or, ideally, repeated deep (re-)drawing. However, to simulate these loading conditions, a large volume of steel substrate material must be modeled and thus the computational cost of such a simulation would be prohibitive. A possible method to reduce the computational costs is to incorporate the developed framework into a global-local approach, for example by embedding the detailed geometry into a bulk model, see Fig. 6.1. Since the surrounding material only has to reflect the presence of the bulk and impose the desired boundary conditions, simplified constitutive laws may be used, e.g. elasto-plasticity for the steel. Such a procedure dramatically decreases the computational cost by restricting the region of interest to a small subvolume of the geometry.
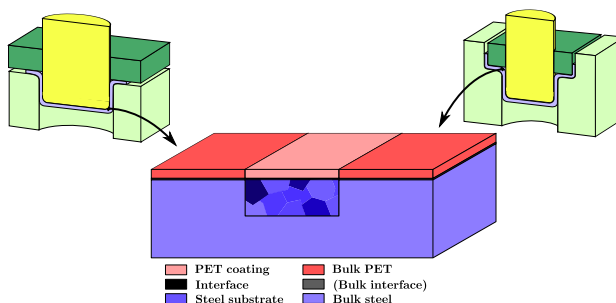

PET coating	Bulk PET
Interface	(Bulk interface)
Steel substrate	Bulk steel

Figure 6.1: Global-local approach to model deep (re-)drawing where a full-scale simulation model is embedded into the polymer-coated steel bulk.

[1] Van der Aa, H.C.E., Van der Aa, M.A.H., Schreurs, P.J.G., Baaijens, F.P.T., Van Veenen, W.J. (2000) An experimental and numerical study of the wall ironing process of polymer coated sheet metal. Mech Mater 32:423–443, 10.1016/S0167-6636(00)00013-2

[2] Alinia, Y., Guler, M.A., Adibnazari, S. (2014) On the contact mechanics of a rolling cylinder on a graded coating. Part 1: Analytical formulation. Mech Mater 68:207–216, 10.1016/j.mechmat.2013.08.010

[3] Allen, D.H., Searcy, C.R. (2001) A micromechanical model for a viscoelastic cohesive zone Int J Fract 107:159–176, 10.1023/A:1007693116116

[4] Bartali, A. E., Aubin, V., Degallaix, S. (2009) Surface observation and measurement techniques to study the fatigue damage micromechanisms in a duplex stainless steel. Int J Fatigue 31:2049–2055, 10.1016/j.ijfatigue.2008.11.003

[5] Bay, B.K., Smith, T.S., Fyhrie, D.P., Saad, M. (1999) Digital volume correlation: Three-dimensional strain mapping using x-ray tomography. Exp Mech 39:217–226, 10.1007/BF02323555

[6] Becker, R. (1998) Effects of strain localization on surface roughening during sheet forming. Acta Mater 46:1385–1401, 10.1016/S1359-6454(97)00182-1

[7] Van der Beek, M.H.E., Peters, G.W.M., Meijer, H.E.H. (2006) Influence of Shear Flow on the Specific Volume and the Crystalline Morphology of Isotactic Polypropylene Macromolecules 39:1805–1814, 10.1021/ma051914e

[8] Besnard, G., Hild, F., Roux, S.G. (2006) "Finite-element" displacement fields analysis from digital images: Application to Portevin-Le Châtelier bands. Exp Mech 46(6):789–803, 10.1007/s11340-006-9824-8

[9] Boelen, B., den Hartog, H., Van der Weijde, H. (2004) Product performance of polymer coated packaging steel, study of the mechanism of defect growth in cans. Prog Org Coat 50:40–46, 10.1016/j.porgcoat.2003.09.011

[10] Boelen, B. (2009) The influence of deformation on product performance of pre-coated packaging steels. PhD thesis, chapter 5, Delft University of Technology

[11] Borg, U., Fleck, N.A. (2007) Strain gradient effects in surface roughening. Model Simul Mater Sci Eng 15:S1–S12, 10.1088/0965-0393/15/1/S01

[12] Van den Bosch, M.J., Schreurs, P.J.G., Geers, M.G.D. (2006) An improved description of the exponential Xu and Needleman cohesive zone law for mixed-mode decohesion. Eng Fract Mech 73:1220-1234, 10.1016/j.engfracmech.2005.12.006

[13] Van den Bosch, M.J., Schreurs, P.J.G., Geers, M.G.D. (2007) A cohesive zone model with a large displacement formulation accounting for interfacial fibrilation. Eur J Mech A 26:1–19, 10.1016/j.euromechsol.2006.09.003

[14] Van den Bosch, M.J., Schreurs, P.J.G., Geers, M.G.D., Van Maris, M.P.F.H.L. (2008) Interfacial characterization of pre-strained polymer coated steel by a numerical-experimental approach. Mech Mater 40:302–317, 10.1016/j.mechmat.2007.09.002

[15] Van den Bosch, M.J., Schreurs, P.J.G., Geers, M.G.D. (2008) Identification and characterization of delamination in polymer coated metal sheet. J Mech Phys Solids 56:3259–3276, 10.1016/j.jmps.2008.07.006

[16] Boyce, M.C., Parks, D.M., Argon, A.S. (1988) Large inelastic deformation of glassy polymers. Part I: rate dependent constitutive model. Mech Mater 7:15–33, 10.1016/0167-6636(88)90003-8

[17] Van Breemen, L.C.A., Klompen, E.T.J., Govaert, L.E., Meijer, H.E.H. (2011) Extending the EGP constitutive model for polymer glasses to multiple relaxation times. J Mech Phys Solids 59:2191–2207, 10.1016/j.jmps.2011.05.001

[18] Bronkhorst, C.A., Kalidindi, S.R., Anand, L. (1992) Polycrystalline plasticity and the evolution of crystallographic texture in FCC metals. Philos Trans R Soc London A 341:443–477, 10.1098/rsta.1992.0111

[19] Broutman, L.J., Patil, R.S. (1971) Cold Rolling of Polymers. 1 Influence of Rolling on Properties of Amorphous Polymers. Pol Eng Sci 11:165–173, 10.1002/pen.760110212

[20] Caillard, D. (2010) Kinetics of dislocations in pure Fe. Part I. In situ straining experiments at room temperature. Acta Mater 58:3493–3503, 10.1016/j.actamat.2010.02.023

[21] Cheong, K., Busso, E.P. (2006) Effects of lattice misorientations on strain heterogeneities in FCC polycrystals. J Mech Phys Solids 54:671–689, 10.1016/j.jmps.2005.11.003

[22] Christiansen, A. W., Baer, E., Radcliffe, S. V. (1971) The mechanical behaviour of polymers under high pressure. Philos Mag 24:451–467, 10.1080/14786437108227400

[23] Clarisse, L., Bataille, A., Pennec, Y., Crampon, J., Duclos, R. (1999) Investigation of grain boundary sliding during superplastic deformation of a fine-grained alumina by atomic force microscopy. Ceram Int 25(4):389–394, 10.1016/S0272-8842(98)00044-3

[24] Dao, M., Asaro, R.J. (1993) Non-Schmid effects and localized plastic flow in intermetallic alloys. Mater Sci Eng 170:143–160, 10.1016/0921-5093(93)90376-P

[25] Faber, E.T., Vellinga, W.P.,De Hosson, J.T.M. (2013) Local delamination on heavily deformed polymerâĂŞmetal interfaces: evidence from microscopy. J Mater Sci 49:691–700, 10.1007/s10853-013-7750-6

[26] Faber, E.T., Vellinga, W.P., De Hosson, J.T.M. (2014) FIB-Etching of Polymer/Metal Laminates and its Effect on Mechanical Performance. Microsc Microanal, *in press*, 10.1017/S1431927614013531

[27] Faber, E.T., Martinez-Martinez, D., Mansilla, C., Ocelík, V., De Hosson, J.T.M. (2014) Calibration-free quantitative surface topography reconstruction in scanning electron microscopy. Ultramicroscopy 148C:31–41, 10.1016/j.ultramic.2014.08.009

[28] Fedorov, A.V., Van Tijum, R., Vellinga, W.P., De Hosson, J.T.M. (2007) Degradation and recovery of adhesion properties of deformed metal-polymer interfaces studied by laser induced delamination. Prog Org Coat 58:180–186, 10.1016/j.porgcoat.2006.08.025

[29] Furnémont, Q., Kempf, M., Jacques, P.J., Göken, M., Delannay, F. (2002) On the measurement of the nanohardness of the constitutive phases of TRIP-assisted multiphase steels. Mater Sci Eng A 328:26–32, 10.1016/S0921-5093(01)01689-6

[30] Gao, Z., Wang, Y., Gioia, G., Cuitiño, A. M. (2002) A global approach for Digital Speckle Correlation. Proc SEM Annual Conf

[31] Geers, M.G.D., De Borst, R., Brekelmans, W.A.M. (1996) Computing strain fields from discrete displacement fields in 2D-solids. Int J Solids Struct 33:4293–4307, 10.1016/0020-7683(95)00240-5

[32] Van der Giessen, E., Needleman, A (1995) Discrete dislocation plasticity: a simple planar model. Model Simul Mater Sci Eng 21:085015, 10.1088/0965-0393/3/5/008

[33] Gorlier, E., Haudin, J.M., Billon, N. (2001) Strain-induced crystallisation in bulk amorphous PET under uni-axial loading Polymer 42:9541–9549, 10.1016/S0032-3861(01)00497-9

[34] Gröger, R., Racherla, V., Bassani, J. L., Vitek, V. (2008) Multiscale modeling of plastic deformation of molybdenum and tungsten: II. Yield criterion for single crystals based on atomistic studies of glide of $1/2\langle 111 \rangle$ screw dislocations Acta Mater 56:5412–5425, 10.1016/j.actamat.2008.07.037

[35] Guler, M.A., Alinia, Y., Adibnazari, S. (2013) On the contact mechanics of a rolling cylinder on a graded coating. Part 2: Numerical results. Mech Mater 66:134–159, 10.1016/j.mechmat.2013.07.014

[36] Han, K., Ciccotti, M., Roux, S.G. (2010) Measuring nanoscale stress intensity factors with an atomic force microscope. Europhys Lett 89(6):66003, 10.1209/0295-5075/89/66003

[37] Hild, F., Roux, S.G. (2006) Digital image correlation: From displacement measurement to identification of elastic properties - a review. Strain 42(2):69–80, 10.1111/j.1475-1305.2006.00258.x

[38] Hild, F., Roux, S.G. (2012) Comparison of local and global approaches to digital image correlation. Exp Mech 52(9):1503–1519, 10.1007/s11340-012-9603-7

[39] Hutchinson, J.W. (1976) Bounds and self-consistent estimates for creep of polycrystalline materials Proc R Soc London A 348:101–127, 10.1098/rspa.1976.0027

[40] Jöchen, K., Böhlke, T. (2013) Representative reduction of crystallographic orientation data. J Appl Crystallogr 46:960–971, 10.1107/S0021889813010972

[41] Klompen, E.T.J., Engels, T.A.P., Van Breemen, L.C.A., Schreurs, P.J.G., Govaert, L.E., Meijer, H.E.H. (2005) Quantitative Prediction of Long-Term Failure of Polycarbonate. Macromolecules 38:7009–7017, 10.1021/ma0504973

[42] Klompen, E.T.J. (2005) Mechanical properties of solid polymers: constitutive modelling of long and short term behaviour. PhD thesis, chapter 1, Eindhoven University of Technology

[43] Knauss, W.G., Chasiotis, L., Huang, Y. (2003) Mechanical measurements at the micron and nanometer scales Mech Mater 35:217–231, 10.1016/S0167-6636(02)00271-5

[44] Leclerc, H., Périé, J.N., Roux, S.G., Hild, F. (2009) Integrated Digital Image Correlation for the Identification of Mechanical Properties. In: Gagalowicz A, Philips W (eds) MIRAGE 2009. LNCS, vol. 5496. Springer, Berlin (Germany), pp 161–171, 10.1007/978-3-642-01811-4_15

[45] Lim, H., Carroll, J.D., Battaile, C.C., Buchheit, T.E., Boyce, B.L., Weinberger, C.R. (2014) Grain-scale experimental validation of crystal plasticity finite element simulations of tantalum oligocrystals. Int J Plast 60:1–18, 10.1016/j.ijplas.2014.05.004

[46] Man, J., Obrtlík, K., Polák, J. (2003) Study of surface relief evolution in fatigued 316L austenitic stainless steel by AFM. Mater Sci Eng A 351(1-2):123–132, 10.1016/S0921-5093(02)00846-8

[47] Matsuoka, S. (1998) Effects of cold-rolling on the cold forging of solid polymer. J Mater Process Technol 84:175–180, 10.1016/S0924-0136(98)00094-6

[48] Van Melick, H.G.H., Govaert, L.E.,, Meijer, H.E.H. (2003) Localisation phenomena in glassy polymers: influence of thermal and mechanical history. Polymer 44:3579–3591, 10.1016/S0032-3861(03)00089-2

[49] Nygårds, M., Gudmundson, P. (2004) Numerical investigation of the effect of nonlocal plasticity onÂăsurface roughening in metals. Eur J Mech A-Solid 23:753–762, 10.1016/j.euromechsol.2004.05.001

[50] Pan, B., Qian, K., Xie, H., Asundi, A. (2009) Two-dimensional digital image correlation for in-plane displacement and strain measurement: a review. Meas Sci Technol 20:062001, 10.1088/0957-0233/20/6/062001

[51] Polák, J., Man, J., Vystavěl, T., Petrenec, M. (2009) The shape of extrusions and intrusions and initiation of stage I fatigue cracks. Mater Sci Eng A 517(1-2):204–211, 10.1016/j.msea.2009.03.070

[52] Poluektov, M., Van Dommelen, J.A.W., Govaert, L.E., Yakimets, I., Geers, M.G.D. (2013) Micromechanical modelling of short-term and long-term large-strain behaviour of polyethylene terephthalate. Model Simul Mater Sci Eng 21:085015, 10.1088/0965-0393/21/8/085015

[53] Quey, R., Dawson, P.R., Barbe, F. (2011) Large-scale 3D random polycrystals for the finite element method: Generation, meshing and remeshing. Comput Meth Appl Mech Eng 200:1729–1745, 10.1016/j.cma.2011.01.002

[54] Raabe, D., Sachtleber, M., Weiland, H., Scheele, G., Zhao, Z. (2003) Grain-scale micromechanics of polycrystal surfaces during plastic straining. Acta Mater 51:1539–1560, 10.1016/S1359-6454(02)00557-8

[55] Rossiter, J., Brahme, A., Inal, K., Mishra, R. (2013) Numerical analyses of surface roughness during bending of FCC single crystals and polycrystals. Int J Plast 46:82–93, 10.1016/j.ijplas.2013.01.016

[56] Sachtleber, M., Raabe, D., Weiland, H. (2004) Surface roughening and color changes of coated Aluminum sheets during plastic straining. J Mater Process Technol 148(1):68–76, 10.1016/j.jmatprotec.2004.01.041

[57] Samyn, P., Schoukens, G. (2008) Experimental extrapolation model for friction and wear of polymers on different testing scales. Int J Mech Sci 50:1390–1403, 10.1016/j.ijmecsci.2008.07.002

[58] Santore, M.M., Duran, R.S., McKenna, G.B. (1991) Volume recovery in epoxy glasses subjected to torsional deformations: the question of rejuvenation. Polymer 32:2377–2381, 10.1016/0032-3861(91)90077-V

[59] Schwerdtfeger, J., Nadgorny, E., Koutsos, V., Blackford, J.R., Zaiser, M. (2010) Statistical heterogeneity of plastic deformation: An investigation based on surface profilometry. Acta Mater 58(14):4859–4870, 10.1016/j.actamat.2010.05.024

[60] Šiška, F., Forest, S, Gumbsch, P., Weygand, D (2007) Finite element simulations of the cyclic elastoplastic behaviour of copper thin films. Model Simul Mater Sci Eng 15:S217–S238, 10.1088/0965-0393/15/1/S17

[61] Sutton, M. A., Orteu, J.-J., Schreier, H. (2009) Image Correlation for Shape, Motion and Deformation Measurements: Basic Concepts,Theory and Applications. Springer, New York

[62] Tang, Z., Liang, J., Xiao, Z., Guo, C. (2012) Large deformation measurement scheme for 3D digital image correlation method. Opt Laser Eng 50:122–130, 10.1016/j.optlaseng.2011.09.018

[63] Tasan, C.C., Hoefnagels, J.P.M., Geers, M.G.D. (2010) Microstructural banding effects clarified through micrographic digital image correlation. Scripta Mater 62(11):835–838, 10.1016/j.scriptamat.2010.02.014

[64] Tata Steel packaging 2015, www.tatasteelpackaging.com

[65] Thomas, T.R. (1972) Computer simulation of wear. Wear 22(1):83–90, 10.1016/0043-1648(72)90429-2

[66] Van Tijum, R., Vellinga, W.P., De Hosson, J.T.M. (2007) Surface roughening of metal-polymer systems during plastic deformation. Acta Mater 55:2757–2764, 10.1016/j.actamat.2006.12.013

[67] Van Tijum, R., Vellinga, W.P., De Hosson, J.T.M. (2007) Adhesion along metal-polymer interfaces during plastic deformation. J Mater Sci 42:3529–3536, 10.1007/s10853-006-1374-z

[68] Turteltaub, S., Suiker, A. (2005) Transformation-induced plasticity in ferrous alloys. J Mech Phys Solids 53:1747–1788, 10.1016/j.jmps.2005.03.004

[69] Uchida, M., Tada, N. (2011) Sequential evaluation of continuous deformation field of semi-crystalline polymers during tensile deformation accompanied by neck propagation. Int J Plasticity 27:2085–2102, 10.1016/j.ijplas.2011.07.009

[70] Usov, P.P., Danilov, V.D. (2007) Contact problem for elastic layer and rigid cylinder with friction forces. J Frict Wear 28:225–238, 10.3103/S1068366607030014

[71] Vendroux, G., Knauss, W. G. (1998) Submicron deformation field measurements: Part 2. Improved digital image correlation. Exp Mech 38:86–92, 10.1007/BF02321649

[72] Vossen, B.G., Schreurs, P.J.G., Van der Sluis, O., Geers, M.G.D. (2014) Multi-scale modelling of delamination through fibrillation. J Mech Phys Solids 66:117–132, 10.1016/j.jmps.2014.01.009

[73] Wu, P.D., Lloyd, D.J. (2004) Analysis of surface roughening in AA6111 automotive sheet. Acta Mater 52:1785–1798, 10.1016/j.actamat.2003.12.039

[74] Yalçinkaya, T., Brekelmans, W.A.M., Geers, M.G.D. (2008) BCC single crystal plasticity modeling and its experimental identification. Model Simul Mater Sci Eng 16:085007, 10.1088/0965-0393/16/8/085007

[75] Zhao, Z., Ramesh, M., Raabe, D. Cuitiño, A.M., Radovitzky, R. (2008) Investigation of three-dimensional aspects of grain-scale plastic surface deformation of an aluminum oligocrystal. Int J Plasticity 24:2278–2297, 10.1016/j.ijplas.2008.01.002

[76] Zoller, P., Fakhreddine, Y.A. (1994) Pressure-volume-temperature studies of semi-crystalline polymers. Thermochim Acta 238:397–415, 10.1016/S0040-6031(94)85221-9

Samenvatting

Industriële innovatie in de verpakkingsindustrie wordt momenteel grotendeels gedreven door milieubehoud. Deze industrie probeert dit te bereiken door het verbeteren van bestaande productieprocessen. Een typisch voorbeeld is de voedselindustrie waar verpakkingsmateriaal wordt gebruikt dat bestaat uit dun plaatstaal met een polymere beschermlaag. Recentelijk is in deze industrie de milieuvriendelijkheid van het productieproces verhoogd door de polymere beschermlaag aan te brengen voordat de verpakking wordt gemaakt. Ten opzichte van het aanbrengen van de beschermlaag na productie leidt deze innovatie tot een reductie van een-derde in het energieverbruik en de CO_2 emissie alsook een reductie tot nagenoeg nul van het gebruikte water en de resulterende afvalstoffen.

Helaas is deze innovatie niet zonder uitdagingen aangezien het materiaal onderhevig is aan grote vervormingen bij verhoogde temperaturen en hoge reksnelheden tijdens het productieproces. Deze vervormingen resulteren in oppervlakteverruwing van het staal en dus ook van de polymeer-staal grenslaag. Na productie mag deze grenslaag geen schade (zowel zichtbaar en onzichtbaar) vertonen, ook niet tijdens de langdurige houdbaarheidsperiode. Deze schade leidt namelijk tot corrosie en tot een verlies van de kwaliteit van de inhoud.

In dit proefschrift wordt de invloed van deformatie geïnduceerde staal oppervlakteverruwing tijdens productie op de integriteit van de polymeer-staal binding onderzocht. Hiervoor is een model ontwikkeld waarin numerieke simulaties worden gekoppeld aan experimenten zodat de grenslaag kan worden bestudeerd tijdens deformatie geïnduceerde oppervlakteverruwing van een verpakkingsmateriaal. De experimenten geven een kwalitatief en kwantitatief inzicht in het verruwingsfenomeen. De resultaten zijn verwerkt in numerieke simulaties om een voorspelling te doen over de integriteit van de polymeer-staal binding.

Als eerste stap is het verruwingsfenomeen experimenteel bestudeerd. Een dunne staalplaat is in trek vervormd en de hoogteprofielen zijn tijdens het deformatieproces gemeten met een confocale optische microscoop. Deze profielen zijn vervolgens gebruikt in een, binnen dit onderzoek ontwikkelde, beeldcorrelatie methode. Deze methode maakt gebruik van de Eindige Elementen methode om de driedimensionale verplaatsingsvelden tussen de gemeten hoogteprofielen te bepalen. Deze verplaatsingsvelden maken het vormende ruwheidslandschap op het staal zichtbaar. Dit landschap groeit als de deformatie toeneemt.

De berekende verplaatsingsvelden zijn vervolgens toegepast als een randvoorwaarde in een tweedimensionale simulatie van een polymeerlaag. Voor de simulaties is vlakke rek aangenomen en de polymeer-staal grenslaag is gemodelleerd door middel van een zogenaamd "cohesive zone" model. De gesimuleerde experimentele staal verruwing leidt tot spanningsconcentraties in de polymeerlaag. Nabij deze concentraties wordt loslating

van de grenslaag voorspeld. Door middel van het variëren van de thermodynamische geschiedenis van de polymeerlaag is een optimale leeftijd van het polymeer ontdekt. Een relatief jonge polymeerlaag vertoont namelijk significant minder loslating in verhouding tot een oudere laag door een afname van de spanningsconcentraties.

Echter, na het aanbrengen van de polymere beschermlaag wordt het verpakkingsmateriaal doorgaans voor langdurige periodes opgeslagen, bijvoorbeeld tijdens transport. Tijdens deze periodes veroudert het polymeer continu en zal het dus ver van de optimale leeftijd zijn tijdens het productieproces. Een mogelijkheid om de optimale leeftijd te bereiken voordat het productieproces start, en dus om loslating tijdens productie te voorkomen, is het optimaliseren van de thermodynamische geschiedenis van de polymeerlaag. Dit is bijvoorbeeld mogelijk door het verpakkingsmateriaal voorafgaand aan de verdere verwerking te walsen. De invloed van het vooraf walsen is bestudeerd door middel van een walssimulatie. De simulaties voorspellen een significante afhankelijkheid van de geschiedenisparameter op de aangebrachte walsreductie. Dit impliceert dat de walsreductie kan worden geoptimaliseerd om loslating van de polymeer-staal grenslaag te verminderen of zelfs te voorkomen.

Tijdens productie is het verpakkingsmateriaal onderhevig aan verschillende complexe vervormingsprocessen. Tijdens deze processen is het staaloppervlak onzichtbaar, bijvoorbeeld tijdens dieptrekken en wandstrekken. Om dit soort vervormingsprocessen te kunnen bestuderen is een kristalplasticiteitsmodel toegevoegd aan het numerieke model om de staalverruwing te kunnen voorspellen. Simulaties van trek (in één richting) vertonen een goede vergelijking met experimentele observaties. De simulaties voorspellen ook loslating van de polymeer-staal binding als gevolg van de voorspelde staalverruwing. Een vergelijking tussen simulaties in trek en in druk laten zien dat de verruwing sterker is in druk dan in trek wat leidt tot een toename van de voorspelde loslating.

De in deze dissertatie ontwikkelde modellen hebben geleid tot kwalitatief en (semi-) kwantitatief begrip over het verruwen van verpakkingsstalen tijdens productie. Daarnaast is de invloed van verruwing op de integriteit van de polymeer-staal binding gekarakteriseerd. Met het geïdentificeerde optimum in de thermodynamische geschiedenis van de polymere beschermlaag en de mogelijkheid om deze geschiedenis te optimaliseren voordat het productieproces start kan de loslating van de polymeer-staal binding tijdens productie worden verminderd of zelfs voorkomen. Ten slotte zorgt de toevoeging van een voorspellend staal model, i.c. een kristalplasticiteitsmodel, voor een aanvulling op de omslachtige metingen van gedetailleerde experimentele verplaatsingsvelden die plaatsvinden tijdens deformatie geïnduceerde staalverruwing. Hierdoor wordt analyse van vormingsprocessen mogelijk waarbij het meten van het hoogteprofiel van het staal moeilijk danwel onmogelijk is, bijvoorbeeld tijdens industriële omvormprocessen zoals dieptrekken.

> "**There is some good in this world,
> and it's worth fighting for.**"
> *J.R.R. Tolkien, The Two Towers*

Obviously, the research presented within this thesis was not accomplished without help in many shapes and forms. First of all, I would like to express my gratitude to my promotor, Marc Geers. You believed in my abilities and convinced me to start on this journey and guided me through it all these years. My daily supervisor, Piet Schreurs, also played a role. Piet, the many discussions, both on-topic and highly off-topic, have certainly contributed to the end result and my view on life. Of course my employer, M2i, also deserves recognition for allowing me to spend four years researching an industrially-relevant topic. Furthermore, the organized social activities made the past four years more enjoyable. Additionally, I thank my defense committee members for taking the time, and effort, for reading my thesis and providing the necessary feedback for improvements.

During the course of the past four years, I have met many great people from all over the world who have made the PhD struggle bearable. In particular, I thank my fellow PhD students and the staff members and support personnel of the MaTe group for the many critical discussions, social activities and just always being helpful when needed. The people of room 4.09, 4.13 and 4.21 (that includes you, Bart!) deserve special mention for creating a great social atmosphere, where even the not-so-bright questions were (sarcastically) answered.

Last but most definitely not least, I thank my friends and family for aiding wherever and whenever it was possible. Words cannot describe my gratitude for the never-ending stream of support and understanding during the more difficult moments of emotional turmoil in the past four years. While I undoubtedly will forget someone this way, some personal words: Mom and dad, thank you for always being there and the indestructible confidence in my abilities, even in the moments where I had none. Without the solid foundation that you have created for me I would not have been able to chase after my dreams and this thesis would certainly not have come to be. Michael, thank you for the numerous caffeine-driven discussions, both research related and (completely) unrelated, during the early morning hours and for the countless of hours spend unloading emotions by excessive clicking (and shouting). Francesco, your Italian view on life during our early morning bike trips, while consuming dinner and while unwinding in Sapri changed the way I look at the world. Michèl and Yvonne, thank you for providing the means to

vent my emotions without drawbacks. I truly hope you will find your place in life, you deserve it. Marlous and Ivana, thank you for the support and understanding, providing perspective and for making sure I had a way of letting go of the troubles that lay behind and ahead, even if only for a short moment. Emanuela, Mary and Jasna, thank you for the many activities outside of work, which showed me that there is much more to life than work, and for giving me a new (international) view on the world. Mahan, Matt, Abel and Adrian, even though you are thousands of kilometers away, you still provided mental support and created some unforgettable memories. Thank you.

Jeroen van Beeck
Helmond, 2015

CURRICULUM VITAE

Jeroen van Beeck was born on the 28$^{\text{th}}$ of September 1987 in Oss. After finishing secondary education in 2005, he started in the Bachelor program of Mechanical Engineering at the Eindhoven University of Technology. In 2008, he graduated cum laude with the project "Paper: a closer study", supervised by dr.ir. R.H.J. Peerlings. Directly after, he started in the Master program of Mechanical Engineering at the Eindhoven University of Technology in the group Mechanics of Materials of prof.dr.ir. M.G.D. Geers. During the master program, Jeroen went abroad for the internship project "The effect of TWIP and TRIP effects on deformation and fracture of high-manganese steels" at the McMaster University in Canada under supervision of prof.dr. J.D. Embury and dr. H.S. Zurob. In 2011, the master program was successfully finished and Jeroen graduated cum laude with the thesis "Multi-scale modeling of mechanical and transformation behaviour of metastable austenitic steels", supervised by dr.ir. V.G. Kouznetsova and prof.dr.ir. M.G.D. Geers. After graduating, Jeroen started a PhD project at the Eindhoven University of Technology titled "Tailoring metallic-organic interfaces to improve product reliability". The project was financially supported by the Materials innovation institute (M2i) in Delft and carried out in the group Mechanics of Materials of prof.dr.ir. M.G.D. Geers, supervised by dr.ir. P.J.G. Schreurs. The results of this project are presented in this thesis.

"I had a good day."
Ending of Cloverfield